Parametrization of relative humidity- and wavelength-dependent optical properties of mixed Saharan dust and marine aerosol

Von der Fakultät für Physik und Geowissenschaften

der Universität Leipzig

genehmigte

DISSERTATION

zur Erlangung des akademischen Grades

Doctor rerum naturalium

(Dr. rer. nat.)

vorgelegt

von Dipl.-Met. Alexander Schladitz

geboren am 3. Januar 1982 in Leipzig

Gutachter: Prof. Dr. Alfred Wiedensohler
Prof. Dr. David S. Covert

Tag der Verleihung: 20. Juni 2011

Bibliographische Beschreibung

Schladitz, Alexander

Parametrization of relative humidity- and wavelength-dependent optical properties of mixed Saharan dust and marine aerosol

Universität Leipzig, Dissertation

139 S.*, 165 Lit.*, 59 Abb., 14 Tab., Anlagen

Referat:

Aerosolpartikel wechselwirken durch Streu- und Absorptionsprozesse mit der einfallenden Sonnenstrahlung und haben somit einen direkten Strahlungseffekt. Bei relativen Feuchten bis 100% können Aerosolpartikel aufquellen und somit ihre Größe ändern. Im Zuge des Aufquellens, ändern sich die optischen Eigenschaften und somit auch der direkte Strahlungseffekt der Aerosolpartikel. Speziell für Mischungen von verschiedenen Aerosolspezies ist die Änderung der optischen Eigenschaften des Aerosols durch Feuchteeinfluss noch nicht ausreichend verstanden.

Gegenstand der vorliegenden Arbeit ist daher die Quantifizierung der wellenlängen- und feuchteabhängigen optischen Eigenschaften einer Mischung von Saharastaub- und marinen Aerosol. Die zur Quantifizierung notwendigen Daten wurden im Rahmen einer Feldmessung von mikrophysikalischen- und optischen Aerosol-Eigenschaften auf den Kapverdischen Inseln gesammelt. Auf Grundlage dieser Messungen wurde ein Aerosol-Modell entwickelt. Dieses Modell wurde daraufhin verwendet, um Berechnungen von optischen Aerosol-Eigenschaften bei relativen Feuchten bis 90% durchzuführen. Eine Messung der Lichtschwächung durch Aerosolpartikel unter Umgebungsbedingungen wurde verwandt, um das Modell bei Umgebungsfeuchten zu validieren. Die Wellenlängen- und Feuchteabhängigkeit der optischen Eigenschaften des Aerosols wurde parametrisiert und konnte anhand von zwei Parametergleichungen bestimmt werden.

Unter Benutzung von tabellierten Werten und der Wellenlänge des einfallenden sichtbaren Sonnenlichtes, der relativen Feuchte, sowie der Staubvolumenfraktion, kann die Feuchteabhängigkeit von wichtigen Aerosol-optischen Eigenschaften für Saharastaub, marinen Aerosol und einer Mischung aus beiden Komponenten bestimmt werden. Globale Zirkulationsmodelle, die auch eine Berechnung von Strahlungseffekten durch Aerosolpartikel beinhalten, nutzen Aerosol-optische Eigenschaften als Eingabeparameter. Durch zunehmende Komplexität zur Beschreibung von Wechselwirkungen in der Atmosphäre, sind einfache Parametrisierungen unabdingbar. Die vorliegende Arbeit liefert daher einen wichtigen Beitrag für die Modellierung von Strahlungseffekten durch Aerosolpartikel und somit zum Verständnis des Strahlungshaushaltes der Erde.

---

* 139 S. (Seitenzahl insgesamt)

165 Lit. (Anzahl der im Literaturverzeichnis ausgewiesenen Literaturangaben)

Bibliographic description

Schladitz, Alexander

Parametrization of relative humidity- and wavelength-dependent optical properties of mixed Saharan dust and marine aerosol

University of Leipzig, Dissertation

139 pp., 165 Lit., 59 Fig., 14 Tab., Appendix

Abstract:

Aerosol particles interact with sunlight through scattering and absorption and have therefore a direct radiative effect. Hygroscopic aerosol particles take up water and are able to grow in size below 100% relative humidity, which involves the change of optical properties and the direct radiative effect. The change of aerosol optical properties for aerosol mixtures under humidification is presently not well understood, especially for the largest particle sources worldwide.

The present PhD-thesis quantifies wavelength- and humidity-dependent aerosol optical properties for a mixture of Saharan mineral dust and marine aerosol. For quantification, an aerosol model was developed, which based on in-situ measurements of microphysical and optical properties at Cape Verde. With this model, aerosol optical properties were calculated from the dry state up to 90% relative humidity. To validate the model, a measure of the total extenuated light from particles under ambient conditions was used. Finally, the humidity dependence of aerosol optical properties for marine aerosol, Saharan dust aerosol, and a mixture of both species was described by two empirical equations. With the wavelength of the incident visible solar radiation, relative humidity, and dry dust volume fraction, the humidity dependence of optical properties can be calculated from tabulated values. To calculate radiative effects, aerosol optical properties were used as input parameters for global circulation models including radiative transfer. Due to the complexity of aerosol related processes, they have been treated implicitly, meaning in parameterized form. For modelling purposes, the present PhD-thesis provides a solution to include humidity effects of aerosol optical properties.

---

*

139 pp. (Total number of pages)

165 Lit. (Number of references)

Contents

List of Figures

List of Tables

List of Abbreviations

ACE	**A**erosol **C**haracterization **E**xperiment
AOP	**A**erosol **O**ptical **P**roperty
APS	**A**erodynamic **P**article **S**izer
ARIADNE	**A**e**R**osol Phys**I**cal and Chemic**A**l I**D**e**N**tification on Cret**E**
asl	**a**bove **s**ea **l**evel
BPC	**B**ulk-to-**P**article **C**onversion
CAREBeijing	**C**ampaigns of **A**ir Quality **RE**search in **B**eijing and Surrounding Region
CCN	**C**loud **C**ondensation **N**ucleus
CPC	**C**ondensation **P**article **C**ounter
CRH	re**C**rystallization **R**elative **H**umidity
CTS	**C**onstrained **T**wo **S**tream method
DDA	**D**iscrete **D**ipole **A**pproximation
DMA	**D**ifferential **M**obility **A**nalyzer
DMPS	**D**ifferential **M**obility **P**article **S**izer
DOY	**D**ay **O**f **Y**ear
DRH	**D**eliquescence **R**elative **H**umidity
ESCC	**E**xtra **S**harp **C**ut **C**yclone
FDTDM	**F**inite **D**ifference **T**ime **D**omain **M**ethod
FSM	**F**orward **S**catter **M**eter
GCM	**G**eneral **C**irculation **M**odel
GF-PDF	**G**rowth **F**actor - **P**robability **D**ensity **F**unction
GPC	**G**as-to-**P**article **C**onversion
HAPS	**H**umidified **APS**
HDMPS	**H**umidifying **D**ifferential **M**obility **P**article **S**izer
HTDMA	**H**ygroscopicity **T**andem **D**ifferential **M**obility **A**nalyzer
IfT	Leibniz **I**nstitute **f**or **T**ropospheric Research
IPCC	**I**ntergovernmental **P**anel On **C**limate **C**hange
lidar	**li**ght **d**etection **a**nd **r**anging
LT	**L**ocal **T**ime
MAAP	**M**ulti **A**ngle **A**bsorption **P**hotometer
MAC	**M**ass **A**bsorption **C**ross section

MBL	**M**arine **B**oundary **L**ayer
MINI	**MIN**iature cascade **I**mpactor
NSS	**N**on-**S**ea-**S**alt sulfate
PM	**P**articulate **M**atter
PNSD	**P**article **N**umber **S**ize **D**istribution
PRIDE-PRD	**P**rogram of **R**egional **I**ntegrate**D** **E**xperiments of Air Quality over **P**earl **R**iver **D**elta
PSAP	**P**article **S**oot **A**bsorption **P**hotometer
SOAP	**S**pectral **O**ptical **A**bsorption **P**hotometer
PSL	**P**oly**S**tyrene **L**atex
RH	**R**elative **H**umidity
SAMUM	**SA**hran **M**ineral D**U**st experi**M**ent
SHADE	**S**a**HA**ran **D**ust **E**xperiment
TEM	**T**ransmission **E**lectron **M**icroscopy
TMM	**T**-**M**atrix **M**ethod
TOA	**T**op **O**f **A**tmosphere
TSP	**T**otal **S**uspended **P**articles
UTC	**U**niversal **T**ime **C**oordinated

$(NH_4)_2SO_4$	Ammonium Sulfate
NaCl	Sodium Chloride
Na_2SO_4	Sodium Sulfate

Notation

Roman symbols	Quantity	Unit
$\text{Å}(\lambda_1/\lambda_2)$	Ångström-exponent at wavelengths λ_1 and λ_2	-
C_c	Cunningham slip correction factor	-
C_i	absorption, scattering, and extinction cross sections ($i = a, s, e$)	m^2
GF_{hyd}	mean hygroscopic growth factor of hydrophobic particles	-
GF_{hyg}	mean hygroscopic growth factor of hygroscopic particles	-
$\overline{GF}$	average hygroscopic growth factor	-
$GF_{a,hyd}$	mean aerodynamic hygroscopic growth factor of hydrophobic particles	-
$GF_{a,hyg}$	mean aerodynamic hygroscopic growth factor of hygroscopic particles	-
$\overline{GF_a}$	average aerodynamic hygroscopic growth factor	-
$I(\theta)$	normalized angular illumination function of integrating nephelometer	-
$\mathcal{M}$	real scattering matrix	-
M_s	molecular weight of solute s	$\mathrm{kg\,mol^{-1}}$
M_w	molecular weight of water	$0.018\,\mathrm{kg\,mol^{-1}}$
N	total particle number concentration	$\mathrm{cm^{-3}}$
Q	aerosol flow rate	$\mathrm{m^3\,s^{-1}}$
Q_i	absorption, scattering, and extinction efficiency factors ($i = a, s, e$)	-
R	universal gas constant	$8.314\,\mathrm{J\,K^{-1}\,mol^{-1}}$
$\mathbf{S}$	normalized Stokes vector	-
T_{amb}	temperature at ambient conditions	K
T	temperature inside the measurement container	K

U	voltage between inner and outer rod of the DMA	V
V	volume concentration	$\mathrm{m^3\,m^{-3}}$
Z_p	electrical mobility	$\mathrm{m^2\,V^{-1}\,s^{-1}}$
$\overline{Z_p}$	midpoint electrical mobility	$\mathrm{m^2\,V^{-1}\,s^{-1}}$
ΔZ_p	electrical mobility width	$\mathrm{m^2\,V^{-1}\,s^{-1}}$

Roman symbols	**Quantity**	**Unit**
a	distance from scatterer	m
a_w	water activity	-
d_{gN}	geometric mean diameter of particle mode	m
dp	particle diameter	m
dp_a	aerodynamic particle diameter	m
dp_c	critical droplet diameter	m
dp_m	mobility particle diameter	m
dp_s	particle diameter of dry solute s	m
dp_{ve}	volume equivalent particle diameter	m
e	elementary charge	$1.602 \cdot 10^{-19}\,\mathrm{C}$
$e_{sat}(dp, dp_s)$	saturation vapor pressure over droplet with solute	Pa
$e_{sat}(\infty)$	saturation vapor pressure over plane water surface	Pa
$e_{sat}(\infty, n_s)$	saturation vapor pressure over plane water surface containing solute s	Pa
$f'(\theta, \Phi)$	scattering phase function for scattering and azimuth angle	$\mathrm{m^{-1}\,sr^{-1}}$
$f(\Omega)$	scattering phase function for solid angle	$\mathrm{sr^{-1}}$
$f'(\Omega)$	scattering phase function for solid angle	$\mathrm{m^{-1}\,sr^{-1}}$
g	asymmetry parameter	-
i	van't Hoff factor	-
k	wavenumber	$\mathrm{m^{-1}}$
l	effective length of the electric field in a DMA	m
$\tilde{m}$	complex refractive index of particle	-
$\tilde{m}_w$	complex refractive index of water	-
m	real part of $\tilde{m}$	-
n	imaginary part of $\tilde{m}$	-
n_e	number of elementary charges	-
nf_{hyd}	mean hydrophobic number fraction	-
nf_{hyg}	mean hygroscopic number fraction	-

n_s	mole number of solute s	-
n_w	mole number of water	-
p_{amb}	atmospheric pressure at ambient conditions	Pa
r	Pearson's correlation coefficient	-
r_1	radius of the inner electrode of a DMA	m
r_2	radius of the outer electrode of a DMA	m
vf_{dust}	dust volume fraction fraction of total aerosol	-
vf_{dust,PM_1}	dust volume fraction within PM_1	-
x	size parameter	-
x_s	solute weight fraction	-

Greek symbols	**Quantity**	**Unit**
Φ	azimuth angle	rad
Ω	solid angle	sr
η	viscosity of the carrier gas	$\mathrm{kg\,m^{-1}\,s^{-1}}$
θ	scattering angle	rad
κ	hygroscopicity parameter	-
λ	wavelength of radiation	m
π	mathematical constant	3.14159265
ξ_a	humidification factor of absorption coefficient	-
ξ_e	humidification factor of extinction coefficient	-
ξ_g	humidification factor of asymmetry parameter	-
ξ_s	humidification factor of scattering coefficient	-
ξ_{ω_0}	humidification factor of single scattering albedo	-
ρ	solution density	$\mathrm{kg\,m^{-3}}$
ρ_0	reference density	$\mathrm{kg\,m^{-3}}$
ρ_{eff}	effective particle density	-
ρ_p	particle density	$\mathrm{kg\,m^{-3}}$
ρ_s	solute density	$\mathrm{kg\,m^{-3}}$
ρ_w	water density	$\mathrm{kg\,m^{-3}}$
σ_i	absorption, scattering, and extinction coefficients ($i = a, s, e$)	$\mathrm{m^{-1}}$
$\sigma_{a,soot}$	absorption coefficient of soot	$\mathrm{m^{-1}}$
$\sigma_{a,dust}$	absorption coefficient of mineral dust	$\mathrm{m^{-1}}$

$\sigma_{a,dust}^{\text{Mie}}$	calculated absorption coefficient of mineral dust	m^{-1}
$\sigma_a^{\text{PM}_1\text{ PSAP}}$	measured absorption coefficient by the PM_1 PSAP	m^{-1}
$\sigma_a^{\text{PM}_{10}\text{ PSAP}}$	measured absorption coefficient by the PM_{10} PSAP	m^{-1}
σ_a^{SOAP}	measured absorption coefficient by the SOAP	m^{-1}
σ_g	geometric standard deviation of particle mode	-
σ_s^{neph}	measured nephelometer scattering coefficient	m^{-1}
σ_w	water surface tension	$\text{J}\,\text{m}^2$
χ	dynamic shape factor	-
ω_0	single scattering albedo	-

1 Introduction

1.1 Placement of the thesis in meteorological science

The understanding of the radiation processes between the Earth's atmosphere and surface is a subject in meteorological science. The radiative balance and not only the incident radiation from the sun is responsible for the global mean temperature of the Earth's surface and atmosphere. The Earth's radiative balance can be altered due to changes in the incoming solar radiation, planetary albedo and in the emitted longwave energy flux. In turn, changes in the planetary albedo result from changes in the aerosol content in the atmosphere from natural and anthropogenic sources and land albedo, as well as from changes of gas concentrations in the atmosphere, which absorb solar radiation (Seinfeld and Pandis, 2006). Any such alteration is a radiative forcing that disturbs the equilibrium and leads to a nonzero average downward net radiative flux at the top of the atmosphere (Seinfeld and Pandis, 2006). For instance, an increase (decrease) of the net downward radiative flux heats (cools) the Earth.

In this regard, an aerosol is defined as the suspension of solid or liquid particles in a carrier gas (typically air). These suspended particles occur in the size range from a few nanometers to 100 μm. However, these microscopically small particles interact with radiation by scattering and absorption. The scattering and absorption behavior can alter the planetary albedo and has therefore a direct effect on the radiative forcing. The same physical process that causes the direct effect is the reduction in visibility in a particle laden air mass. To quantify the direct radiative forcing, the albedo of the underlying surface, the vertical aerosol distribution, aerosol optical depth, the fraction of the surface covered by clouds (cloudiness) and relative humidity and wavelength-dependent aerosol optical properties (e.g., single scattering albedo and upscatter fraction) are crucial (Seinfeld and Pandis, 2006; Tegen *et al.*, 1996). The single scattering albedo is a key parameter governing the change in planetary albedo. A so called critical single scattering albedo, which is dependent on the albedo of the underlying surface and the upscatter fraction, defines the boundary between negative (cooling) and positive (heating) direct radiative forcing (Heintzenberg *et al.*, 1997; Liao and Seinfeld, 1998). Nevertheless, this approximation is valid in absence of clouds.

Another effect that alters the planetary albedo is the first indirect effect, called Twomey effect (Twomey, 1974, 1977), which describes the influence of aerosols on clouds. If relative humidity exceeds a critical value, hygroscopic particles become cloud condensation nuclei (CCN) and activate to cloud droplets. An increased CCN concentration due to anthro-

pogenic pollution increases the number of cloud droplets. Since the given amount of water is distributed over more drops, the effective cloud droplet diameter is reduced. Clouds with smaller droplets, but with a larger CCN concentration in comparison with larger droplets and smaller CCN concentrations, have a higher cloud optical thickness and cloud albedo. Examples for this behavior are ship tracks observed in marine stratocumulus layers. The microphysically induced effect of aerosols on the liquid water content, cloud height, and lifetime of clouds is called the second indirect effect (e.g., Ramaswamy *et al.* (2001)).

1.2 Motivation

As outlined in the last section the quantification of the direct radiative forcing depends on a number of different parameters. In contrast to atmospheric greenhouse gases such as CO_2, CH_4, N_2O, and the CFCs, aerosol particles show a large spatial and temporal variability in size, concentration, and composition. Particles are emitted directly due to bulk-to-particle conversion (BPC) from crustal material (e.g., mineral dust) or from sea spray (e.g., sea-salt) and due to gas-to-particle conversion (GPC) by nucleation of precursor gases (sulfuric acid, organic carbon, ammonia). Particles can also be emitted due to high temperature combustion processes or biomass combustion (e.g., elemental and organic carbon). These varieties of particle types are most abundant close to their sources, e.g., mineral dust particles in the outflow of large arid regions or secondary and combustion particles in highly industrialized regions in the Northern Hemisphere. These are some arguments that make the prediction of radiative forcing by particles more difficult than for the gases. Nevertheless, the last Intergovernmental Panel On Climate Change (IPCC) report IPCC (2007) included numerous research studies, e.g., Forster *et al.* (2007) in quantifying the aerosol direct radiative forcing. Based on the newest results of general circulation models (GCMs), which include radiative transfer, the direct aerosol forcing is -0.5±0.4 $\mathrm{W\,m^{-2}}$ what means a cooling. However, the recent IPCC report (IPCC, 2007) rates the scientific understanding of the direct radiative forcing to be medium or even low.

The largest natural particle sources are mineral dust with a global estimated source strength of 1500±700 $\mathrm{Tg\,yr^{-1}}$ (Tegen *et al.*, 1996) and sea-salt with ∼1300 $\mathrm{Tg\,yr^{-1}}$ (Andreae, 1995). Tegen and Fung (1995) estimate the anthropogenic contribution of mineral dust to be 30 - 50% of the total dust burden in the atmosphere, which were later updated by Tegen *et al.* (2004) to only 5 - 7%. Mineral dust from anthropogenic sources originates mainly from agricultural practices (harvesting, ploughing, overgrazing), and changes in surface water (e.g., Caspian and Aral Sea, Owens Lake) (Prospero *et al.*, 2002). In contrast to sea-salt and mineral dust, sulfate and black carbon have minor total global burdens, ranging from 91.7 to 125.5 $\mathrm{Tg\,yr^{-1}}$ and 5.8 to 8.0 $\mathrm{Tg\,yr^{-1}}$, respectively (Haywood and Boucher, 2000). The direct anthropogenic radiative forcing on the top of the atmosphere (TOA) for the largest particle sources is estimated to be -0.1±0.5 $\mathrm{W\,m^{-2}}$ for mineral dust particles and -0.35±0.15 $\mathrm{W\,m^{-2}}$ for sulfate particles (Forster *et al.*, 2007). For black carbon particles, the direct radiative

forcing on TOA is positive and is given by Forster *et al.* (2007) to $0.44 \pm 0.13\,\mathrm{W\,m^{-2}}$. Note the high uncertainty of the direct anthropogenic radiative forcing, especially for mineral dust. One major reason for that is caused by the uncertainty of the quantification of aerosol optical properties (AOP), e.g., complex refractive index, asymmetry parameter, and single scattering albedo. Moreover, the humidity dependence of aerosol optical properties are crucial to predict the direct radiative forcing correctly (Quinn *et al.*, 1996).

Hygroscopic growth at relative humidities below 100% influences strongly their scattering properties (Hänel, 1976; Nemesure *et al.*, 1995) mainly by changing the particle size but also the refractive index (Covert *et al.*, 1972). The hygroscopic particle growth behavior is insufficiently implemented in GCMs and is therefore a significant source of uncertainty when predicting direct radiative forcing (Kinne *et al.*, 2003). However, efforts were undertaken to include effects of hygroscopic growth of aerosol particles in GCMs (Randall *et al.*, 2007). In GCMs, which include radiative transfer, aerosol related processes have been treated implicitly, meaning in parameterized form. An explicit calculation of AOPs from the dry to the ambient condition using the Köhler theory (Köhler, 1936) tends to be too complex to be applicable in a GCM. Empirical growth laws determined from experimental data may therefore provide a more applicable solution to better approximate ambient aerosol radiative properties at the current state of model development. There is a need to quantify the humidity dependence for AOPs of the largest natural and also anthropogenic sources.

The humidity dependency of the scattering coefficient of the marine aerosol were determined from experimental data for several locations of the world, e.g., off the pacific coast of the United States (Hegg *et al.*, 1996), in the Pacific and Southern Oceans (Carrico *et al.*, 1998) and in the northern Atlantic during ACE-2 (Carrico *et al.*, 2000). Humidity dependence on AOPs in the presence of Asian dust during ACE-Asia was reported by Anderson *et al.* (2003), Carrico *et al.* (2003), Howell *et al.* (2006), and Yoon and Kim (2006). Relative humidity-dependent AOPs of a mixture of marine and transported Saharan dust aerosol was published by Li-Jones *et al.* (1998) and Lack *et al.* (2009). Nevertheless, the weakness of the most of the publications given above, is to present the humidity dependence for only one AOP (e.g., absorption or scattering coefficients) and for few wavelengths (530, 532, and 550 nm).

In contrast to that, the amenity of aerosol models (e.g., Hänel (1976); Shettle and Fenn (1979); D'Almeida *et al.* (1991)) is that they deliver a comprehensive set of humidity-dependent AOPs for certain aerosol species for a large wavelength range. In some regions, the aerosol consists however, of a mixture of the two largest aerosol species, e.g., Saharan dust which is the most important source of desert dust on a global scale (Washington *et al.*, 2003) and marine aerosol. To conclude, a comprehensive quantification of humidity effects of AOPs of such an aerosol mixture is presently a gap in knowledge.

1.3 Goals

This PhD-work contributes to the identified gap in the frame of the Saharan Mineral Dust Experiment (SAMUM) consortium. Other participants of the SAMUM consortium (status in 2011) are the "Deutsches Zentrum für Luft- und Raumfahrt" (DLR) which operates the aircraft "Falcon" for in-situ and remote sensing of the vertical and spatial distribution of microphysical and optical aerosol properties. In cooperation with the University of Leipzig, several instruments were operated at the "Falcon" to measure radiances and irradiances in the visible solar spectrum. The DLR also provided instrumentation to investigate longwave radiative effects of Saharan dust. The modelling department of the Leibniz Institute for Tropospheric Research (IfT) was involved to model the transport of the Saharan dust and biomass burning aerosol, its modification and the radiative impact. IfT and University of Munich operated three multi-wavelength lidar systems and a novel wind lidar to measure the vertical distribution of Saharan dust and biomass burning aerosol and the vertical mixing within aerosol layers. The Technical University Darmstadt (TU Darmstadt) provided physicochemical and mineralogical parameters of mixed mineral dust, biomass burning and marine aerosols as well as meteorological instruments.
Two experiments were carried out in the framework of this consortium. The first experiment called SAMUM-1 was conducted in May / June 2006 at the outskirts of the Saharan desert in Ouarzazate and in Zagora, Morocco. The scope of SAMUM-1 was to better determine the parameters relevant for computing the direct radiative effect of Saharan dust. As discussed in chapter 1.2, the sign of the radiative forcing of mineral dust in a global meaning is uncertain (Tegen *et al.*, 1996; Sokolik and Toon, 1999). To be more specific, the SAMUM-1 campaign determined optical properties of pure mineral dust. Two years later the SAMUM consortium moved to the Cape Verde Islands at the outflow region of mineral dust from the Saharan desert. The second experiment, called SAMUM-2, was carried out in January / February 2008, with the highest occurrence of spreading dust plumes from the Saharan desert over the Atlantic (Chiapello *et al.*, 1997; Engelstaedter *et al.*, 2006), especially at low altitudes in the trade wind layer (Chiapello *et al.*, 1995). SAMUM-2 was planned to quantify the radiative effects of the mixed plume of Saharan dust, biomass burning aerosol from central Africa and marine aerosol from the Atlantic. With the knowledge from SAMUM-1 it should be possible to test the hypothesis that dust processing during transport leads to changes in hygroscopic and optical properties of the Saharan dust.
The goal of this PhD-work is the quantification and parametrization of optical properties of the mixed aerosol for dry and ambient conditions with ground-based in-situ measurements. After the introduction, the theoretical background of hygroscopic and optical aerosol properties is given (chapter 2). In the following chapter 3, the measurement location and meteorological conditions are described. Chapter 4 "Measurement techniques and data processing", introduces the used measurement devices and the data processing for the individual instruments is explained. Chapter 5 "Aerosol characterization and closure studies at dry conditions" characterizes the relevant microphysical and optical aerosol parameters,

which are the prerequisites for chapter 6. Chapter 6 "Aerosol model calculations at ambient conditions" describes the parameters of the aerosol model and validates the model calculations with measured quantities in terms of an optical closure study and mass closure at ambient conditions. The primary goal of the PhD-work is presented in chapter 7, which delivers look-up tables for the parameterized humidification factors for the extinction, scattering and absorption coefficient as well as single scattering albedo and asymmetry parameter. Chapter 7 delivers also parameterizations for the dry single scattering albedo and asymmetry parameter as function of the incident wavelength of light and mineral dust volume fraction. The PhD-work closes with a "Summary and Outlook" (chapter 8).

2 Physical basics

There are two catchwords in the title of the PhD-thesis. These are the aerosol optical properties and the particle behavior when surrounded by humid air. The following sections introduce the reader to the two main issues of this thesis and explain basic analytically and empirically derived equations.

2.1 Optical properties of aerosol particles

In the atmosphere, solar electromagnetic radiation interacts with aerosol particles by scattering and absorption processes. The scattering is the process where an incoming electromagnetic radiation with the wavelength λ hits a inhomogeneity and induces a secondary electromagnetic radiation. Elastic scattering occurs when the wavelength of the secondary electromagnetic radiation equals the wavelength of the incoming radiation. Inelastic (Raman) scattering however occurs when the wavelength changes during the scattering process. The total scattering includes the physical processes of diffraction, refraction and reflection. The scattering process distributes the incoming energy from the electromagnetic wave in different directions. The fraction of electromagnetic radiation scattered in a solid angle Ω is described by the scattering phase function $f(\Omega)$. The derivation of the scattering phase function is shown later in this chapter. Absorption occurs, when one part of the incoming electromagnetic radiation is transformed into thermal energy. A physical property of the particle that describes the absorption and scattering is the complex refractive index

$$\tilde{m} = m - n\,\mathrm{i} \text{ with } \mathrm{i} = \sqrt{-1}. \tag{2.1}$$

In a simple way, the real part m and imaginary part n mainly characterize the scattering and absorption ability, respectively. The imaginary part equals zero if no absorption occurs. To describe the concept of how particles scatter and absorb electromagnetic radiation in the visible spectral range (light), the following assumptions have to be made:

- particles are placed in an homogeneous medium
- particles do not interact with each other, which means the scattered light by one particle is small compared to the incoming radiation and does not influence other particles (single scattering processes)
- only elastic scattering occurs e.g., the wavelength of scattered and incoming light is identical.

Stokes vectors $\mathbf{S} = (I, Q, U, V)$ quantify the energy of different polarizations of incident light $\mathbf{S_i}$ and scattered light $\mathbf{S_s}$. The 4 components of the Stokes vector are

- I = total intensity of the light
- Q = degree of parallel or cross polarized light
- U = degree of 45° polarized light
- V = degree of elliptical polarized light.

The Stokes vector of the scattered radiation $\mathbf{S_s}$ are calculated from the incident radiation $\mathbf{S_i}$ as follows (Bohren and Huffman, 1983):

$$\mathbf{S_s} = \frac{1}{k^2 a^2} \cdot \mathcal{M} \cdot \mathbf{S_i}, \tag{2.2}$$

where $\mathcal{M}$ is the real scattering matrix, a is the distance of the observation point from the scatterer and $k = \frac{2\pi}{\lambda}$ is the wavenumber. The elements of the 4 x 4 matrix $\mathcal{M}$ depend on the particle size and shape, the wavelength λ, the wavelength-dependent complex refractive index $\tilde{m}$ and the scattering angle θ. The elements of the scattering matrix are calculated by solving Maxwell's equations. In general, all 16 elements of the scattering matrix $\mathcal{M}$ for non-spherical particles can be nonzero and independent of each other. For simplification, non-spherical particles are assumed to be randomly oriented (macroscopically isotropic) in a medium and have one symmetry axis. For this case, the scattering matrix becomes block diagonal with eight nonzero elements, while six of them are independent (van de Hulst, 1957). Hence, $\mathcal{M}$ has the form:

$$\mathcal{M} = \begin{pmatrix} S_{11} & S_{12} & 0 & 0 \\ S_{12} & S_{22} & 0 & 0 \\ 0 & 0 & S_{33} & S_{34} \\ 0 & 0 & -S_{34} & S_{44} \end{pmatrix}. \tag{2.3}$$

The incoming sunlight is not polarized and therefore $\mathbf{S_i} = (I_i, 0, 0, 0)$ (Bohren and Huffman, 1983). The Stokes vector of the scattered light is calculated using equation 2.2 and 2.3 as:

$$\begin{pmatrix} I_s \\ Q_s \\ U_s \\ V_s \end{pmatrix} = \frac{1}{k^2 a^2} \begin{pmatrix} S_{11} & S_{12} & 0 & 0 \\ S_{12} & S_{22} & 0 & 0 \\ 0 & 0 & S_{33} & S_{34} \\ 0 & 0 & -S_{34} & S_{44} \end{pmatrix} \begin{pmatrix} I_i \\ 0 \\ 0 \\ 0 \end{pmatrix} = I_i \frac{1}{k^2 a^2} \begin{pmatrix} S_{11} \\ S_{12} \\ 0 \\ 0 \end{pmatrix}. \tag{2.4}$$

From this, it follows that the intensity of the scattered light I_s is solely dependent on the S_{11} component. To describe the spatial intensity of the scattered light, the scattering phase function $f(\Omega)$ is introduced, which equals the S_{11} component of $\mathcal{M}$. The integral of the

scattering phase function over the solid angle Ω is:

$$\int_{\Omega=4\pi} f(\Omega)d\Omega = k^2 C_s, \tag{2.5}$$

where C_s is the scattering cross section.
The sum of scattering and absorption is called extinction. Due to energy conservation, the extinction cross section is defined as (Mishchenko *et al.*, 2000; Bohren and Huffman, 1983):

$$C_e = C_s + C_a. \tag{2.6}$$

In general, the cross sections C_i (here the subscript i stands for $a =$ absorption, $s =$ scattering and $e =$ extinction) describe the scattered, absorbed and extenuated amount of incoming energy I_i per time and space. The ratio of the cross section C_i to the geometric cross section is called efficiency factor Q_i.
The outcomes of solving Maxwell's equation for the scattering problem are efficiency factors Q_i for extinction and scattering as well as the scattering phase function $f(\Omega)$.
For spherical particle diameters much smaller than the incoming wavelength $d_p << \lambda$, the scattering efficiency is (e.g., Bohren and Huffman (1983)):

$$Q_s = \frac{8}{3}x^4 \left[\frac{\tilde{m}^2 - 1}{\tilde{m}^2 + 2}\right]^2 \tag{2.7}$$

and the extinction efficiency is:

$$Q_e = 4xIm\left\{\frac{\tilde{m}^2 - 1}{\tilde{m}^2 + 2}\left[1 + \frac{x^2}{15}\left(\frac{\tilde{m}^2 - 1}{\tilde{m}^2 + 2}\right)\frac{\tilde{m}^4 + 27\tilde{m}^2 + 38}{2\tilde{m}^2 + 3}\right]\right\} + \frac{8}{3}x^4 Re\left\{\left(\frac{\tilde{m}^2 - 1}{\tilde{m}^2 + 2}\right)^2\right\}. \tag{2.8}$$

For particles much larger than the incoming wavelength $d_p >> \lambda$, the asymptotic value of the scattering and extinction efficiency factors are:

$$Q_s = 1 \tag{2.9}$$

$$Q_e = 2. \tag{2.10}$$

For spherical aerosol particles in the range of the incoming wavelength $d_p \approx \lambda$, the Mie theory (Mie, 1908) delivers an analytical solution for the efficiency factors Q_e, Q_s, and the scattering phase function $f(\Omega)$. The derivation of these parameters starting with Maxwell's equations is described e.g. in Bohren and Huffman (1983). There exist a variety of analytical solutions for computation of the optical parameters of non-spherical particles. Common solutions are the discrete dipole approximation (DDA) (Purcell and Pennypacker, 1973), the T-matrix method (TMM) (Waterman, 1971), and finite difference time domain method (FDTDM) (Yee, 1966). An introduction to these methods is delivered by Mishchenko *et al.* (2000). However, each solution is limited in its use and has strengths and weaknesses. With the

TMM, optical properties of rotational symmetric, homogeneous scatterers can be computed up to a size parameter of $x = 200$. The size parameter is defined as $x = \frac{\pi dp}{\lambda}$, where dp ist the particle diameter. In contrast to the TTM, the DDA is used for arbitrary shapes, as well as inhomogeneous and anisotropic particles. Here, one particle is approximated by up to several thousand dipoles. The disadvantage follows that the scattering problem needs to be computed for each dipole, thus increasing the computation effort tremendously, especially for the larger size parameter. As a consequence, current DDA computations can be made up to $x \approx 25$. Within this thesis the following methods for different shaped particles are used to solve the scattering problem:

- Mie theory for spherical homogeneous particles
- TMM for homogeneous prolate spheroids
- DDA for deformed spheroids & aggregates.

2.1.1 Optical properties of particle ensembles

Aerosol particles in the atmosphere cover a size range from a few nanometers to about one hundred micrometers. With the known efficiency factors Q_i and introducing a particle number concentration $\frac{dN}{d\log dp}$ (weighted by the log-equidistant size interval) in a certain volume, the total attenuated light in terms of the scattering, absorption, and extinction coefficient (represented by the index i) can be calculated as follows:

$$\sigma_i = \pi \int_{dp_{min}}^{dp_{max}} Q_i \left(\frac{dp}{2}\right)^2 \frac{dN}{d\log dp} d\log dp. \tag{2.11}$$

Similar to equation 2.11, the scattering phase function $f(\Omega)$ of the particle ensemble in a certain volume can be calculated as:

$$f'(\Omega) = \frac{1}{k^2} \int_{dp_{min}}^{dp_{max}} f(\Omega) \frac{dN}{d\log dp} d\log dp \tag{2.12}$$

The apostrophe $'$ denotes that the scattering phase function has the dimension of $\mathrm{m}^{-1}\mathrm{sr}^{-1}$ instead of sr^{-1}. Introducing the polar azimuth Φ and scattering angle θ, the scattering coefficient for certain angle ranges Φ_1,Φ_2 and θ_1,θ_2 is defined as:

$$\sigma_s = \int_{\theta_1}^{\theta_2} \int_{\Phi_1}^{\Phi_2} f'(\theta, \Phi) \sin(\theta) d\Phi d\theta. \tag{2.13}$$

2.1.2 Dimensionless quantities of optical properties

Extinction, scattering, and absorption coefficients are generally wavelength-dependent. The wavelength dependency of σ_i in a certain wavelength range λ_1, λ_2 gives the Ångström-

exponent (Angström, 1929) that is

$$\text{Å}\,(\lambda_1/\lambda_2) = -\frac{\log(\sigma_i^{\lambda_1}/\sigma_i^{\lambda_2})}{\log(\lambda_1/\lambda_2)}. \tag{2.14}$$

The Ångström - exponent is the exponent of a power law, which is used for the wavelength dependence of σ_i. Soot, for instance, has an Ångström-absorption-exponent of 1 (Bergstrom *et al.*, 2002; Kirchstetter *et al.*, 2004) in the visible spectral range. Saharan mineral dust has an Ångström-absorption-exponent of up to 6 (Linke *et al.*, 2006; Müller *et al.*, 2009b). However, the Ångström-absorption-exponent for Saharan dust is strongly dependent on the wavelength range. The Ångström-extinction-exponent is positive when the particle population is dominated by small particles sizes ($dp << 1\mu$m), while for large particles ($dp > 1\mu$m), the Ångström-extinction-exponent would be zero or slightly negative.
To conclude, the Ångström-absorption-exponent is controlled mostly by chemical composition, while the Ångström-extinction-exponent is controlled mostly by the particle size distribution. Hence, with the Ångström-exponents a classification of the particles by their type and size can be made.
Another dimensionless optical parameter used in this thesis is the asymmetry parameter:

$$g =< \cos\theta >= \frac{1}{\sigma_s}\int_{\Omega=4\pi} f'(\Omega)\cos\theta d\Omega. \tag{2.15}$$

The asymmetry parameter is the expectation value of the cosine of the scattering angle θ. g has values between 1 and -1 and is positive, if the particle scatters more light toward the forward direction ($0 \leq \theta \leq \frac{\pi}{2}$); g is negative if the scattering is directed more toward the back direction ($\frac{\pi}{2} \leq \theta \leq \pi$). The asymmetry parameter vanishes if the scattering is isotropic or the scattering is symmetric about the scattering angle $\theta = \frac{\pi}{2}$. With increasing particle size, the relative scattering in forward direction is enhanced, and therefore the asymmetry parameter can be used to classify the particle ensemble by their average particle size.

The single scattering albedo

$$\omega_0 = \frac{\sigma_s}{\sigma_e} \tag{2.16}$$

is an important quantity in aerosol research, since it has a strong influence on the direct effect of radiative forcing (e.g., Heintzenberg *et al.* (1997)). The single scattering albedo may vary between 0 and 1 and gives the proportion of absorption relative to the scattering. It is thus an indirect measure of the absorption. When $\omega_0 = 0$ the total extenuated light is absorbed, while $\omega_0 = 1$ when no light is absorbed by the particle and the total attenuated light is scattered. Nearly both extreme values were found in the atmosphere, for instance $\omega_0 = 0.17$ for Diesel soot (Schnaiter *et al.*, 2003) and $\omega_0 = 0.99$ for sea-salt dominated aerosol (Quinn *et al.*, 1998).

2.2 Hygroscopic properties of aerosol particles

This chapter introduces the ability of atmospheric aerosol particles to interact with water vapor in the atmosphere. The hygroscopicity is a measure of the affinity of particles to adsorb and absorb water molecules. It encompasses the mass transfer of water in both directions, from the gas phase to the particle phase (condensation) and vice versa (evaporation). Furthermore, the atmosphere seeks equilibrium conditions and reaches that via condensation and evaporation. The affinity of a particle to interact with the surrounding water vapor depends on its chemical composition and size; additionally the relative humidity around the particle controls the amount of water mass transfer.
The theoretical description of this mechanism is the Köhler theory introduced by Köhler (1936). An overview of the classical Köhler theory presented here is taken from Liljequist and Cehak (2006), Pruppacher and Klett (1997), and Rogers and Yau (1989). The classical Köhler theory and several modifications and parametrization made in the last decades, called modified Köhler theory, are introduced in section 2.2.1. Rose *et al.* (2008) give an overview of different types of Köhler models and compared their differences. Within this thesis the modified Köhler theory according to Tang and Munkelwitz (1994) and Petters and Kreidenweis (2007) is used.

2.2.1 Classical and modified Köhler theory

The saturation water vapor pressure over a plane water surface $e_{sat}(\infty)$ can be calculated by the Clausius-Clapeyron equation. Rogers and Yau (1989) and references therein give an empirical formula

$$e_{sat}(\infty) = 6.112 \cdot \exp\left(\frac{17.67T}{T + 243.5}\right) \tag{2.17}$$

that is valid for atmospheric relevant temperatures $243\,\mathrm{K} \leq T \leq 308\,\mathrm{K}$. The saturation water vapor pressure over a water droplet diameter dp is given by the Kelvin equation

$$e_{sat}(dp) = e_{sat}(\infty) \cdot \exp\left(\frac{4M_w\sigma_w}{RT\rho_w dp}\right), \tag{2.18}$$

where M_w is the molecular weight of water, and ρ_w and σ_w are the density of water and surface tension of water, respectively. R is the universal gas constant. Equation 2.18 demonstrates that for a given T and σ_w, the saturation water vapor pressure over the surface of a water droplet dp is larger than that over a plane water surface. Therefore, for a constant T, supersaturation ($e_{sat}(dp) > e_{sat}(\infty)$) is needed for condensation of water vapor on a droplet. The expression $e_{sat}(dp) > e_{sat}(\infty)$ means that the relative humidity (RH) is >100% on the droplet relative to the plane surface. Moreover, smaller water droplets require a higher supersaturation to reach equilibrium conditions between condensation and evaporation. Figure 2.1 shows the Kelvin effect of a pure water droplet as a function of the droplet size dp. From equation 2.18, it is obvious that an atmospheric supersaturation of $\frac{e_{sat}(dp)}{e_{sat}(\infty)}$ is required to form thermodynamic stable pure water droplets of a given size, otherwise they

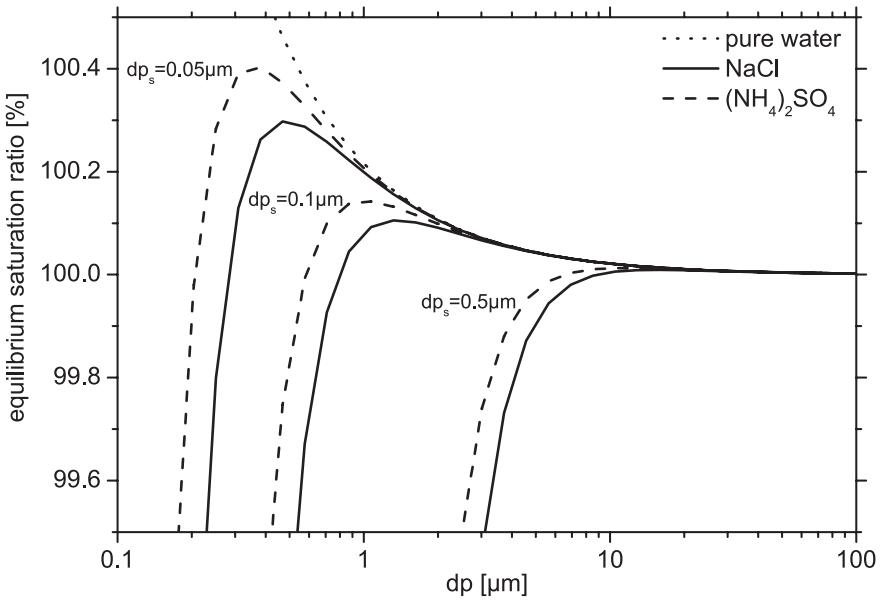

Figure 2.1: *Calculated equilibrium saturation ratio using Köhler theory for pure water (dotted line), sodium chloride (solid line), and ammonium sulfate (dashed line) versus droplet diameter. Curves are shown for several initial dry diameters dp_s*

evaporate. For instance, a droplet size of $dp = 0.05\mu$m requires a supersaturation of 4.4% at $T = 293\,\mathrm{K}$. Such large saturation ratios have been never observed in the atmosphere, where supersaturations rarely exceed 1 - 2% (Rogers and Yau, 1989). Consequently, homogeneous nucleation of liquid water from water vapor does not occur in the atmosphere.
In fact, water droplets in the atmosphere are solutions of water and dissolved particle components e.g., inorganic salts. Indeed, the presence of a condensation nucleus (heterogeneous nucleation) lowers the saturation water vapor pressure over a dissolved water droplet, and hence the equilibrium water vapor pressure occurs at much lower saturation ratios than compared to the pure water case.
The saturation vapor pressure over of a plane water surface consisting of n_w moles water and n_s moles of a solute s, is expressed by Raoult's law:

$$e_{sat}(\infty, n_s) = e_{sat}(\infty)\frac{n_w}{n_w + in_s}. \tag{2.19}$$

The factor i is the degree of ionic dissociation or van't Hoff factor and expresses the deviation from ideality of the solution (Pruppacher and Klett, 1997). An ideal solution means that the dissolved ions do not interact with each other. The most hygroscopic substances found in the atmosphere do not behave ideally in solution. The Raoult's law describes the reduction of the equilibrium saturation water vapor pressure in presence of a solute compared to the pure water case. The reduction of the equilibrium saturation water vapor depends also on the value of the van't Hoff factor, which in turn depends on the solute substance. The ratio $\frac{e_{sat}(\infty,n_s)}{e_{sat}(\infty)}$ is also known as the water activity a_w. Returning to a droplet, replacing the moles of solute and water through masses, and assuming spherical particles for the solute s, the

water activity has the form:

$$a_w = \frac{(dp^3 - dp_s^3)\rho_w/M_w}{i dp_s^3 \rho_s/M_s + (dp^3 - dp_s^3)\rho_w/M_w}, \tag{2.20}$$

where dp_s is the initial dry diameter, ρ_s the dry density, and M_s the molecular weight of the solute s, respectively. Combining the Kelvin equation 2.18 (curvature term) and the Raoult's equation 2.19 (solution term) one obtains the Köhler equation

$$\frac{e_{sat}(dp, dp_s)}{e_{sat}(\infty)} = a_w \cdot \exp\left(\frac{4M_w\sigma_w}{RT\rho_w dp}\right), \tag{2.21}$$

which describes the equilibrium saturation water vapor pressure of a given droplet size dp and solute particle diameter dp_s. Figure 2.1 shows the Köhler curves for solutions of sodium chloride and ammonium sulfate at initial dry solute diameters of $dp_s = 0.05$, 0.1, and 0.5 μm. Each curve represents the equilibrium saturation ratio of a droplet containing a solute relative to a plane water surface. In contrast to the pure water case, an equilibrium saturation ratio can occur under sub-saturated conditions ($\frac{e_{sat}(dp,dp_s)}{e_{sat}(\infty)} = \mathrm{RH} < 100\%$). Furthermore, all curves pass a maximum, which occurs at the critical diameter dp_c (activation diameter) and the equilibrium saturation ratio at dp_c is called critical saturation. The present PhD-work only considers cases for which $dp < dp_c$.

Consider an aqueous droplet lying on the branch of the Köhler curve (cf. Figure 2.1) for which $dp < dp_c$ and is in equilibrium with the atmosphere at a certain saturation ratio (RH). If the droplet size increases (decreases), by adsorbing (desorbing) water, its equilibrium vapor pressure is larger (lower) than the fixed ambient vapor pressure, the droplet shrinks (grows) and the water of the droplet will evaporate (condense) until reaching the former equilibrium state. Finally, the droplets on the rising part ($dp < dp_c$) of the Köhler curve are in stable equilibrium with their environment.

Modified Köhler theory according to Tang and Munkelwitz (1994)

The improvements to enhance the accuracy of the Köhler equation, called modified Köhler theory, occur mostly in the Raoult's term (equation 2.19). The disadvantage of using classical Köhler theory, is that the van't Hoff factor describes the non-ideality of the solution not fair enough. In the following, the modified Köhler theory according to Tang and Munkelwitz (1994) and Tang (1996) is introduced. Now, the water activity a_w introduced in equation 2.21 is represented by the polynomial expression

$$a_w = 1 + \sum C_i x_s^i, \tag{2.22}$$

where C_i are polynomial coefficients (not to be confused with the cross sections in chapter 2.1) and x_s^i is the solute weight fraction in solution in percent. The solute weight fraction

is defined as

$$x_s = 100\frac{\rho_s dp_s^3}{\rho dp^3}, \tag{2.23}$$

where ρ is the density of the solution. Since the density of the solution ρ depends on the solute weight fraction by

$$\rho = 0.9971 + \sum A_i x_s^i \tag{2.24}$$

(Tang and Munkelwitz, 1994), the solute weight fraction has to be determined iteratively by solving

$$\rho\left(x_s\right) x_s dp^3 = 100 dp_s^3 \rho_s. \tag{2.25}$$

Values of A_i and C_i for several solutes, e.g., sodium chloride (NaCl) and ammonium sulfate ($(NH_4)_2SO_4$) are tabulated in Tang and Munkelwitz (1994) and Tang (1996). A comparison of the equilibrium saturation ratio for these two substances calculated with modified Köhler theory after Tang and Munkelwitz (1994) and with classic Köhler theory is shown in Figure 2.2. For supersaturated as well as for sub-saturated conditions, the Köhler theory deviates

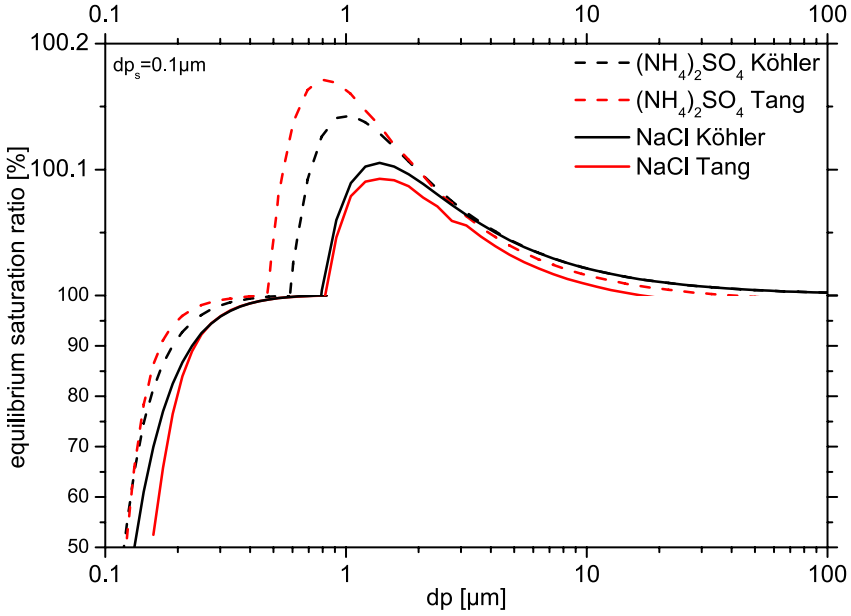

Figure 2.2: *Calculated equilibrium saturation ratio using Köhler theory and modified Köhler theory after Tang and Munkelwitz (1994) and Tang (1996) for sodium chloride (solid line), and ammonium sulfate (dashed line) versus particle diameter.*

from the modified Köhler theory.

However, practical use of the polynomial expression of the water activity is limited, since coefficients are available for a small number of hygroscopic components. In the real atmosphere, the variety of hygroscopic material is much larger, since some hygroscopic material with certain hygroscopicity can interact with hydrophobic material, leading to a modified

hygroscopicity. With regard to a parametrization of the measured hygroscopic growth factor

$$GF(RH) = \frac{dp(RH)}{dp_s} \tag{2.26}$$

for modeling hygroscopic behavior of particles, a simple relationship is additionally worthwhile. In recent years, several studies have been developed to represent the water activity a_w by a single parameter. In Petters and Kreidenweis (2007) this parameter is called κ, whereas in the work of Wex *et al.* (2008) it is called ρ_{ion} and the values can easily be converted. In this work, the parametrization of hygroscopic particle growth is based on the more common κ parameter.

κ - Köhler theory after Petters and Kreidenweis (2007)

Starting with equation 2.19, the water activity can also be written as

$$a_w^{-1} = 1 + i\frac{n_s}{n_w} = 1 + \kappa\frac{dp_s^3}{dp^3 - dp_s^3}, \tag{2.27}$$

where $\kappa = i\frac{M_w\rho_s}{M_s\rho_w}$. Combining equation 2.27, 2.26, and 2.21 the κ parameter can be written as function of the growth factor and the respective relative humidity:

$$\kappa = 1 + \frac{GF^3 - 1}{RH} \cdot \exp\left(\frac{4M_w\sigma_w}{RT\rho_w dp_s GF}\right) - GF^3. \tag{2.28}$$

2.2.2 Hysteresis effect of hygroscopic growth

As already mentioned, aerosol particles can form aqueous solutions at relative humidities below 100%. A property of inorganic (salts) particle components is their hysteresis effect as shown in Figure 2.3.

The phase change from solid to liquid state starting at low RH and increasing it, occurs at a certain relative humidity, commonly called the deliquescence relative humidity (DRH). Below the DRH, which is specific to the chemical composition of the aerosol particle and temperature (Gysel *et al.*, 2002), only a limited amount of water may be adsorbed on the particle (Orr *et al.*, 1958). DRHs of some inorganic salts are given in Table 2.1. If the

Table 2.1: *Physical properties of inorganic salts with corresponding recrystallization- and deliquescence relative humidities taken from Tang (1996).*

salt	ρ_s [kg m^{-3}]	refractive index m	CRH [%]	DRH [%]
$(NH_4)_2SO_4$	1770	1.53	37-40	80
Na_2SO_4	2680	1.48	57-59	84
NaCl	2164	1.544	46-48	75.3

relative humidity equals DRH, the particle spontaneously becomes a solution droplet. If the relative humidity is above the DRH, the particle growths in size according to the Köhler curve.

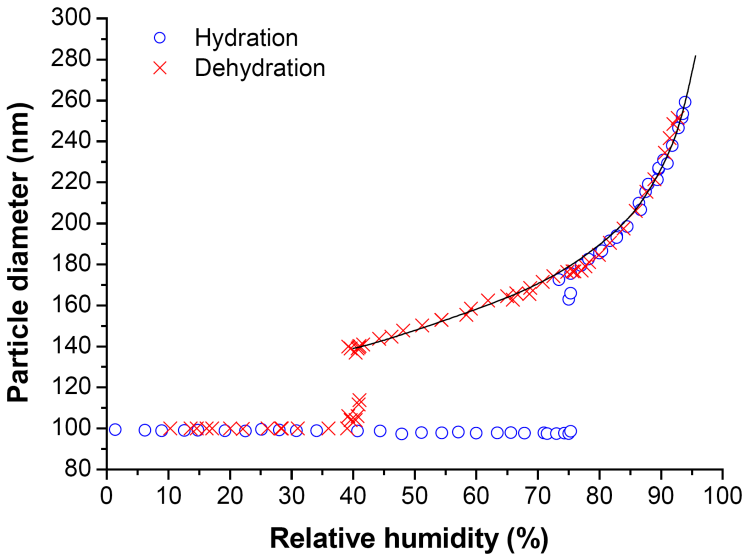

Figure 2.3: *Hysteresis effect of hygroscopic growth of sodium chloride (NaCl) taken from Mikhailov* et al. *(2004). The initial dry NaCl diameter was $dp_s = 99\,nm$. Shown are the measured droplet diameter with an HTDMA during hydration and dehydration.*

For decreasing relative humidity, starting at a point above the DRH, the solution droplet follows the Köhler curve. Below DRH, the solution droplet does not recrystallize and remains in a metastabile equilibrium state as a supersaturated solution droplet (Gysel *et al.*, 2002). Further decrease of the relative humidity leads to a recrystallization. The recrystallization relative humidity (CRH) is much lower than the DRH, and all water evaporates instantaneously from the solution droplet and leftover the solid particle. Table 2.1 gives ranges of CRHs for some inorganic salts.
In general, Rood *et al.* (1989) point out that more than 50% of the aerosol particles for ambient relative humidities between 45 and 75%, are in metastable equilibrium, instead of the more thermodynamically stable solid phase.

3 Measurement site and meteorology

The following chapter describes the measurement site and the meteorological situation during the SAMUM-2 campaign. The measurements presented in this thesis were performed from January 17 to February 10, 2008, which slightly deviate from the official measurement duration of SAMUM-2.

The measurement site was located near the Praia airport (14°57′ N, 23°29′ W, 101 m above sea level, asl) on the Island of Santiago, Cape Verde. The Republic of Cape Verde is located approximately 650 km westwards from the northeast tip of Africa. The measurement site was located on a small hill on the north end of the runway of Praia airport, about two kilometers away from the coastline (Figure 3.1[1]). In order to determine the representative-

Figure 3.1: *Map of the south-eastern part of Santiago Island, Cape Verde taken from OpenStreetMap (http://www.openstreetmap.org/) under license CC-BY-SA (http://creativecommons.org/licensec/by-sa/2.0/).*

ness of the station for characterizing the aerosol from their source areas and not measuring aerosol particles from local anthropogenic emissions, the general circulation pattern, and the prevailing wind directions were taken into account. Figure 3.2 shows the measurement container, which was situated on the measurement site shown in Figure 3.1. The measurement

[1]Due to limitations of use, the figure was changed in the approved version of the PhD-thesis.

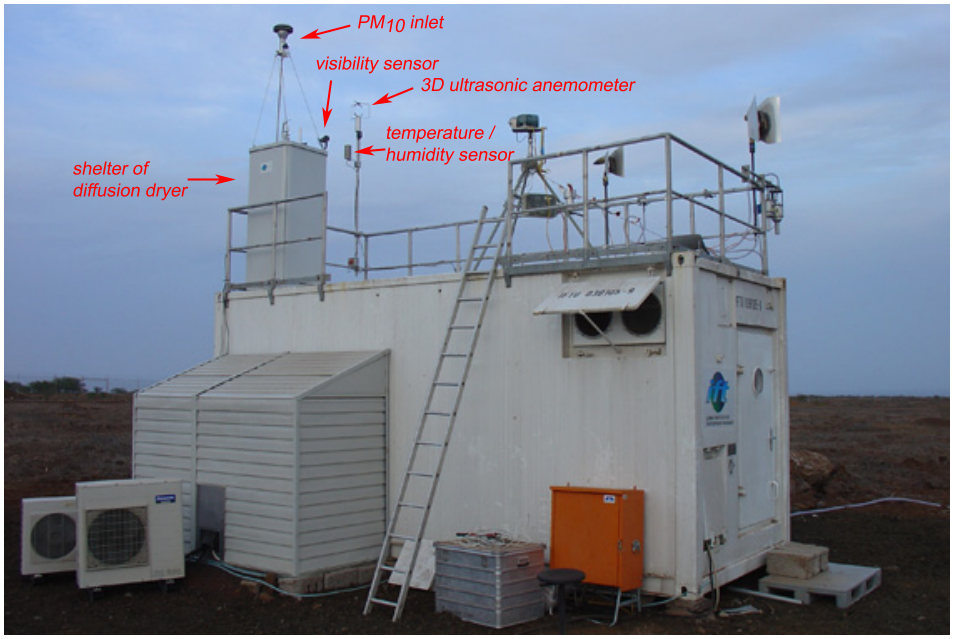

Figure 3.2: *Measurement container from the front position.*

container includes the aerosol instrumentation for in-situ characterization. On the roof top of the measurement container at about 6 m above the ground, an ultrasonic anemometer (Model 81000, R.M. Young, Traverse City, USA) from TU Darmstadt measured the three-dimensional wind. The ultrasonic anemometer was placed in a way, such that the influence from obstacles for the prevailing wind direction was minimal. Further meteorological parameters measured at the station were the relative humidity and air temperature (position is designated by an arrow in Figure 3.2) by a Humicap sensor (HMP233, Vaisala, Vantaa, Finland) and atmospheric air pressure at station level by a barometric sensor (type 5002, Friedrichs, Schenefeld, Germany). The time series of the weather situation at the measurement site is shown in Figure 3.4(a) - (c) in terms of air temperature, relative humidity and atmospheric air pressure. The water vapor mixing ratio shown in Figure 3.4(d) is defined as the ratio of the density of the actual water vapor content to the density of dry air and was calculated from the air temperature and relative humidity. Figure 3.4(e) illustrates the horizontal wind vector (north is at the top) as a time series.

As a result of the Hadley circulation, the predominant wind direction in this region is between NNE and NE. By comparing the measured wind direction with Figure 3.1, contamination with local emissions from larger urban areas (e.g., Praia city and Praia airport) can be excluded. The influence from emissions from the exhaust plume from aircraft is estimated to be minor, since the frequency of starting and landing aircraft was about 5 - 10 times per day. The influence of uplifting crustal material from the island cannot be 100% excluded. An influence is possible, if the surface wind velocity exceeds a threshold wind speed of $8\,\mathrm{m\,s^{-1}}$ (Engelstaedter *et al.* (2006) and references therein). However, the measured wind speeds at the station exceeded the threshold wind velocity of only about 1% of the time. Moreover, wind speed and measured dust mass concentration show no (significant) correlation.

Figure 3.3: *Measurement container from the rear position.*

Looking at the general circulation pattern in the winter season, there are two wind systems, which influence the weather at the Cape Verde Islands. These are the NE trade wind and the Harmattan. The NE trade wind is driven by the Hadley circulation, and transports air masses near the surface from northwestern Africa, along the West-African coastline to the Cape Verde Islands. The Harmattan is a hot, dry wind that is strengthened by a low-pressure center over the north coast of the Gulf of Guinea and a high-pressure center located over northwestern Africa in winter. It blows over the Cape Verde region and Western Sahara from NE or E and is strongest in late fall and winter (late November to mid March).
On January 17, a high pressure centre (Azores anticyclone) was located to the north of the Canary Islands. A flat low-pressure center was located over the Gulf of Guinea. With this pressure field constellation, similar to the Harmattan case, the air moves from east to west in the lowermost levels. In the following days, the high pressure center moved slowly north-eastward across the Iberian Peninsula into the western Mediterranean Sea with slightly increasing core pressure. Hence, the pressure gradient was reduced, leading to a period with lower wind speeds (Figure 3.4e). Trajectories reaching Praia between the surface and 850 hPa (not shown) show advection of Saharan mineral dust mainly from sources in Mali and Niger, but also from the Bodélé Depression in Chad. From January 30, the subtropical high pressure center began to diminish and stayed weak until the end of the campaign. The consequence was a cutting-off effect of the dust transport to the Cape Verde region from the African continent. From February 9, back-trajectories show air masses originating in the tropical Atlantic, caused by the penetration of a cyclonic disturbance from mid-latitudes to the subtropical Atlantic.
The temperature curve in Figure 3.4(a) shows a typical diurnal variation, with maxima typically between 12 p.m. and 2 p.m. local time. The temperatures did not fall below 20° C

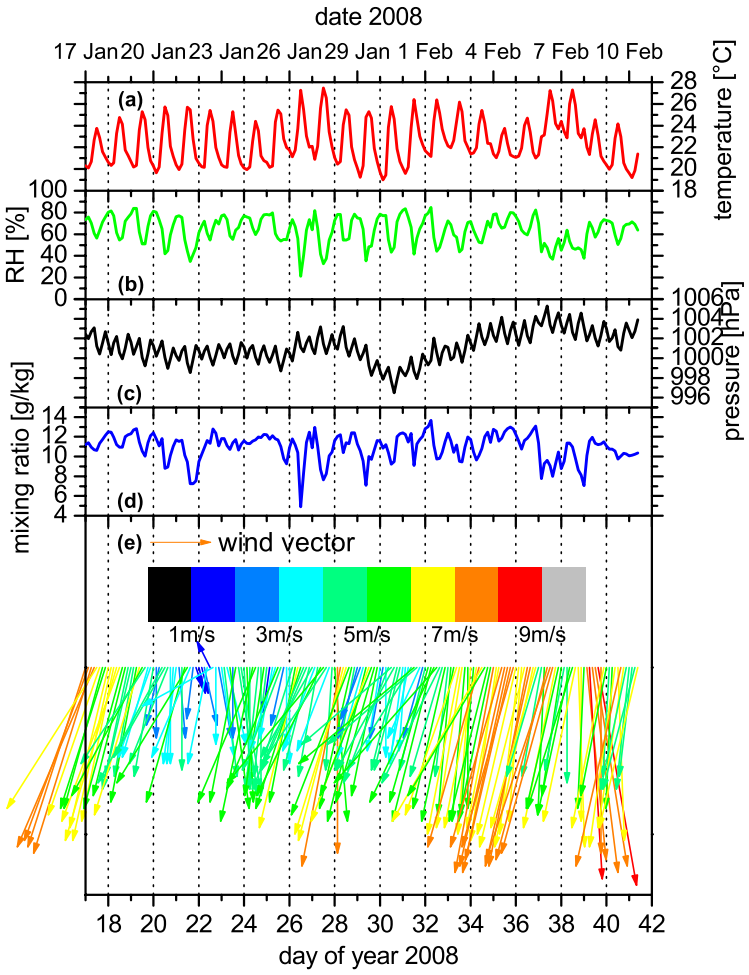

Figure 3.4: *Meteorological data with a temporal resolution of 3 hours from January 17 to February 11, 2008.*

during nighttime, due to the warm reservoir of the surrounding Atlantic Ocean.
If the air parcel's water vapor pressure is constant, the relative humidity (Figure 3.4b) is exclusively dependent on the temperature. The time series of relative humidity shows an opposite diurnal variation with respect to the temperature curve, with lowest values at noon and highest values at nighttime. This effect is caused through increasing saturation water vapor pressure with increasing temperature (cf. equation 2.17). Since the water vapor mixing ratio is a conservative parameter of an air mass, the variation of the water vapor mixing ratio as shown in Figure 3.4(d) was altered through an air mass change or mixing of different air masses. Especially for the dust influenced period, there is a minimum in water vapor mixing ratio during daytime. This behavior is caused by the down-mixing process of dust into the marine boundary layer, because the water vapor mixing ratio of the dry dust layer is lower than in the marine boundary layer. Additionally, this behavior was observed mainly after noon, when convection was fully developed.

Remark:

Text passages or single sentences of the following chapters 4, 5, 6, and 7.1 are taken literally or basically from two submitted publications (status: June 20, 2011) of the author of this PhD-thesis. Also Figures 4.1, 4.7, 4.9, 4.10, 4.11, 4.12, 5.1, 5.2, 5.3, 5.4, 5.5, 5.6, 5.7, 5.8, 5.9, 5.10, 5.11, 5.12, 6.1, 6.2, 6.4, and 6.5 and Tables 5.1, 5.2, 5.3, 7.1, 7.2, 7.3, and 7.4 are taken from these two publication given below.

Schladitz, A., Müller, T., Nowak, A., Kandler, K., Lieke, K., Massling, A. and Wiedensohler, A. 2011a. In-situ aerosol characterization at Cape Verde. Part 1: Particle number size distributions, hygroscopic growth, and state of mixing of the marine and Saharan dust aerosol. to be published in Tellus 63B(4), status: accepted.

Schladitz, A., Müller, T., Nordmann, S., Tesche, M., Groß, S., Freudenthaler, V., Gasteiger, J. and Wiedensohler, A. 2011b. In-situ aerosol characterization at Cape Verde. Part 2: Parametrization of relative humidity- and wavelength-dependent aerosol optical properties. to be published in Tellus 63B(4), status: accepted.

4 Measurement techniques and data processing

In this chapter, important instruments are presented that measure aerosol properties under ambient conditions as well as inside the aerosol measurement container. Figures 3.2 and 3.3 illustrate the position of the instruments located on the roof of the aerosol measurement container. These are the visibility sensor (chapter 4.3.1), $PM_{2.5}$ and PM_{10} filter sampler, a high volume sampler, and a miniature cascade impactor (all in chapter 4.6).
Figure 4.1 gives an overview of the aerosol instruments that operated inside of the aerosol measurement container. To supply the instrumentation with aerosol, an aerosol PM_{10} inlet

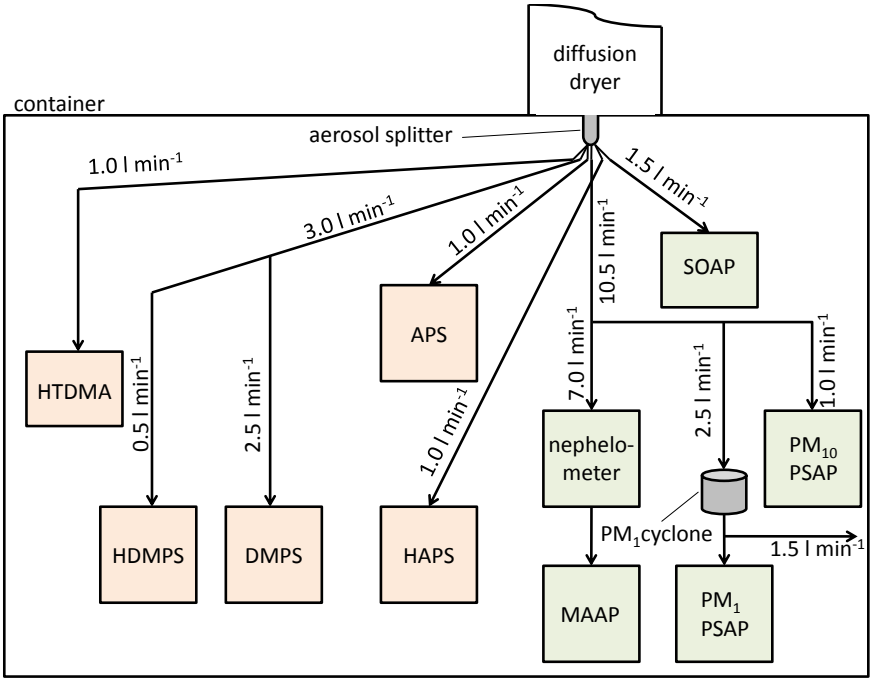

Figure 4.1: *Instrumental setup of the container and flow rate partitioning to each instrument. Instruments for microphysical characterization are shown on the left, whereas optical instrumentation are shown on the right.*

(shown by an arrow in Figure 3.2) from manufacturer Rupprecht and Patashnik Co. Inc., Albany, USA, was employed to remove particles larger than 10 μm in aerodynamic diameter ($dp_a < 10\mu$m). Downstream of the inlet, an automatic aerosol diffusion dryer (Tuch *et al.*, 2009) that was stored in a separate shelter was used to dry the sample aerosol below 30% RH. The dehydration of the sample aerosol is a crucial step to avoid uncontrolled water up-

take of aerosol particles when they enter the air-conditioned aerosol measurement container. Downstream the dryer and inside the measurement container, the sample aerosol was split isokinetically to conduct the aerosol sample to the instruments. The temperature inside the container was kept constant ($T = 293 \pm 2\,\mathrm{K}$), using two independently working air conditioners.

General remarks for the measurements and data processing

Measurement conditions All measured data inside the container relate to container conditions. The conditions inside the container were stable with only small changes in temperature $T = 293 \pm 2\,\mathrm{K}$ and atmospheric pressure $p_{amb} = 1001 \pm 2\,\mathrm{hPa}$ during the campaign. Here, the atmospheric pressure is the measured ambient atmospheric pressure (cf. Figure 3.4).

Date A master computer was configured to run at local time (LT = UTC - 1h). The system time of the other measurement computers was regularly synchronized with the master computer. The measurement data were stored by recording a timestamp. Before processing the data, the timestamps were converted into "day of year 2008" (DOY), which simplified data averaging. In case of no leap year, January 1 and December 31 equal DOY 1 and DOY 365, respectively.

Corrupt data Corrupt data were excluded from the raw dataset. Examples of corrupt data include e.g., power breakdowns, filter changes in the MAAP and PSAP, routine zeroing in the integrating nephelometer, and automatic switching between the two columns of the automatic aerosol diffusion dryer.

Time average Since the HDMPS is the instrument with the lowest temporal resolution of three hours, all data were averaged after data processing within this time interval to yield a uniform data set.

4.1 Dry particle number size distribution

4.1.1 DMPS and APS

The dry particle number size distribution (PNSD) was measured in the size range from $26\,\mathrm{nm} < dp < 10\mu\mathrm{m}$, using two different physical techniques. The polydisperse[1] aerosol was classified by their electrical mobility with a Differential Mobility Particle Sizer (DMPS), whereas the Aerodynamic Particle Sizer (APS model 3321 / Serial no. 1297, TSI Inc., St. Paul, USA) separated the particles due to their inertia. The electrical mobility diameter dp_m is the diameter of a unit-density spherical particle moving at the same velocity in an electric field as the particle in question (Willeke and Baron, 1993). The inertia of a particle can be explicitly attributed to a certain aerodynamic particle diameter dp_a. The measured diameter size range was from $26\,\mathrm{nm} < dp_m < 800\,\mathrm{nm}$ for the DMPS and $0.57\mu\mathrm{m} < dp_a < 10\mu\mathrm{m}$ for the APS. In the following, the design, main parts and calibration procedures of the DMPS and the APS are explained.

[1] Ensemble of particles that consists of more than one particle size

DMPS

Aerosol particles in the atmosphere are naturally bipolarly charged, but the fractions of neutral, positively or negatively charged particles are undefined. In a mobility size spectrometer such as DMPS, aerosol particles pass a ^{85}Kr charger to bring them into a defined bipolar charge equilibrium. The ^{85}Kr beta emitter ionizes the carrier gas and the free air ions are transported to the particles by diffusion and electrostatic forces. In Wiedensohler (1988), the probability of neutral, (multiple) positive or (multiple) negative charged particles in the submicron range is described by an approximation formula. Downstream of the ^{85}Kr charger, the polydisperse charged aerosol enters the Differential Mobility Analyzer (DMA). The DMA is a cylindrical capacitor that can select charged particles according to their electrical mobility Z_p (Knutson and Whitby, 1975):

$$Z_p = \frac{n_e e C_c(dp_m)}{3\pi\eta dp_m}, \tag{4.1}$$

where n_e is the number of negative charges, e the elementary charge ($1.602 \cdot 10^{-19}$ C), η the viscosity of the carrier gas and C_c the size dependent Cunningham slip correction factor. The design of the DMA is shown in Figure 4.2. Between the inner center electrode (positive

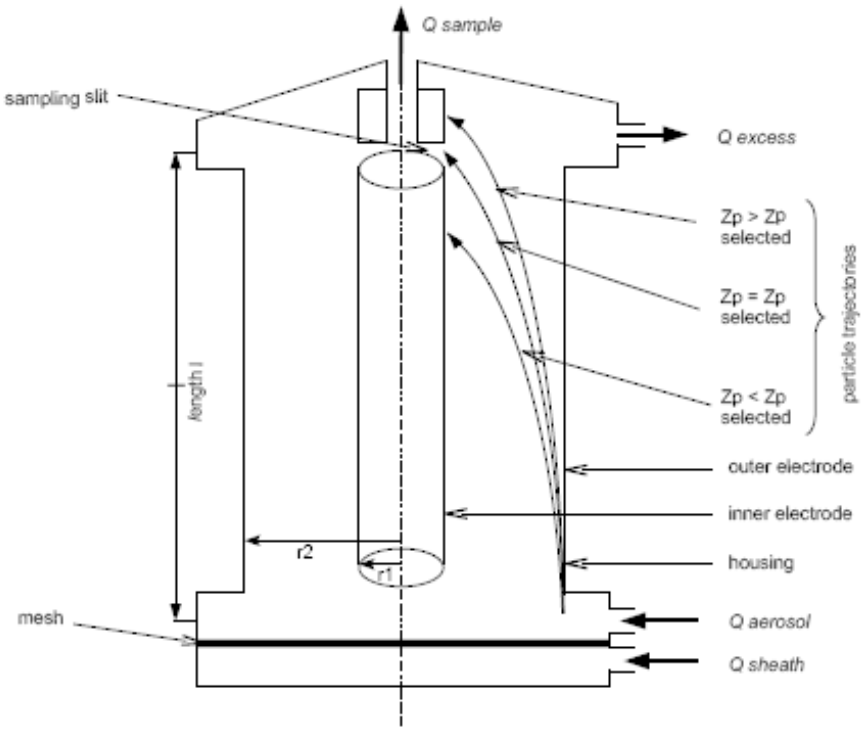

Figure 4.2: *Sketch of a Differential Mobility Analyzer with trajectories of charged particles having a mobility Z_p.*

potential) and the outer grounded electrode with radii r_1 and r_2, a certain voltage U is employed. In Figure 4.2, l describes the effective length of the resulting electric field. A particle free sheath air flow rate Q_{sheath} and a flow rate $Q_{aerosol}$ of the polydisperse charged

aerosol are injected into the DMA. Due to the electric field, positive charged particles precipitate directly onto the outer electrode, while neutral particles are not attracted by the electric field and leave the DMA in the excess air (Q_{excess}). A probability density function (transfer function) describes the probability that particles (negative charge) with a certain mobility Z_p enter the sampling slit of the DMA. An ideal transfer function has a triangular shape with its maximum at $Z_p = \overline{Z_p}$ and its width ΔZ_p. Transfer functions for different DMAs at several flow rates $\frac{Q_{aerosol}}{Q_{sheath}}$ are given e.g., in Birmili *et al.* (1997). According to Knutson and Whitby (1975), the midpoint mobility $\overline{Z_p}$ and the mobility width ΔZ_p of the DMA are:

$$\overline{Z_p} = \frac{Q_{sheath} + Q_{excess}}{4\pi U l} \ln \frac{r_2}{r_1} \tag{4.2}$$

$$\Delta Z_p = \frac{Q_{sample} + Q_{aerosol}}{2\pi U l} \ln \frac{r_2}{r_1}. \tag{4.3}$$

Negative charged particles having an electrical mobility of $Zp = \overline{Zp} \pm \frac{1}{2}\Delta Z_p$, exit the DMA in Q_{sample} through a small sampling slit in the DMA. The DMA (type Vienna medium) was operated at the flow rates of $Q_{sheath} = 5\,\mathrm{l\,min^{-1}}$ and $Q_{aerosol} = 0.5\,\mathrm{l\,min^{-1}}$.

Downstream of the DMA, the number concentration of particles with the same electrical mobility Z_p is measured by a Condensation Particle Counter (CPC model 3010 / Serial no. 2069, TSI Inc., St. Paul, USA). The function of a CPC is following: The sample flow is sucked through the CPC with a constant flow. There, it is saturated with butanol vapor in a slightly heated saturator. Afterwards, the aerosol is conducted through a condenser, where the butanol vapor becomes supersaturated and condenses onto the particles. Subsequently, the aerosol particles grow to micrometer size. In the optical detection unit, the droplets pass a laser beam, and they are individually counted. Measurements with the CPC are limited by the counting efficiency of each CPC type (Wiedensohler *et al.*, 1997), the set sample flow, and several other parameters, e.g., atmospheric pressure, temperature difference between saturator and condenser (Mertes *et al.*, 1995; Hermann and Wiedensohler, 2001). The typical decrease in counting efficiency for particles of $dp_m < 20\,\mathrm{nm}$ is not of interest for this thesis, since the lowest measured diameter was $dp_m = 26\,\mathrm{nm}$. However, the operated CPC worked at the half of the nominal flow rate of $Q_{sample} = 1.0\,\mathrm{l\,min^{-1}}$. The counting efficiency in this case is generally approximately 10% reduced (Birmili, 1998; Nowak, 2006).

The general uncertainty of the DMPS depends mainly on the inaccuracy in sizing, internal particle losses, and measured concentration (Wiedensohler *et al.*, 2010). Fluctuations of the aerosol inlet flow rates (Birmili *et al.*, 1999), which are restricted by the defined range of ±2% leads to an error in counting of about 10%. As a consequence, flow fluctuations influence also the shape of the transfer function in terms of the midpoint mobility and mobility width yielding to a DMPS error in sizing of 2%.

Prior to the measurement campaign, the correct sizing of the DMPS was checked using spherical polystyrene latex particles (PSL) with volume equivalent particle diameters of dp_{ve} = 100, 200, and 500 nm. During the campaign the aerosol, sample, sheath, and excess air flow rates were daily checked using a bubble flow meter (Gilibrator 2, Sensidyne,

Clearwater, USA).

APS

The APS classifies aerosol particles by their aerodynamic diameter. As illustrated in Figure 4.3, a polydisperse sample flow of $1\,\mathrm{l\,min^{-1}}$ is drawn into an inner nozzle by the APS. Particle

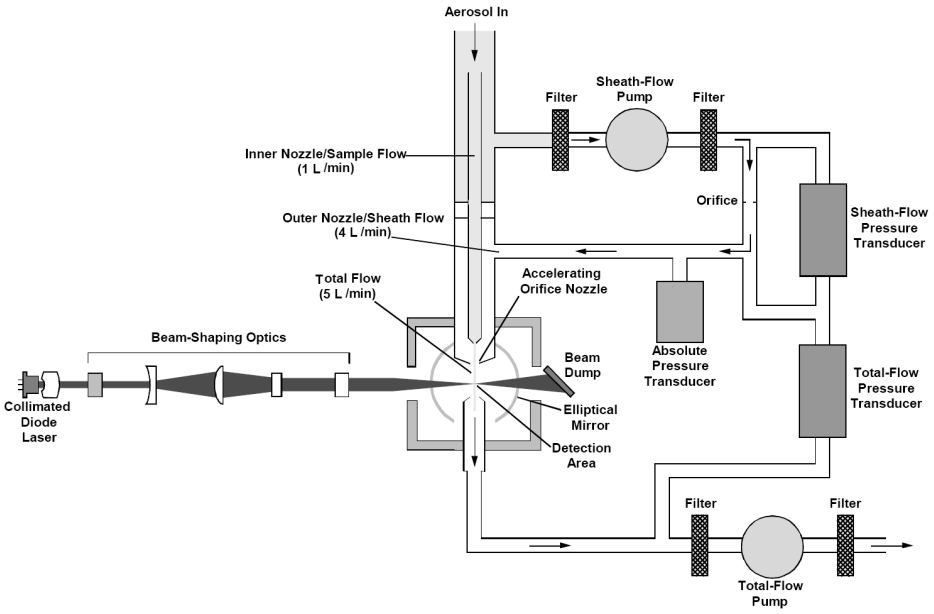

Figure 4.3: *Sketch of the aerosol flow through the APS model 3321 taken from the APS user manual.*

free sheath air with an air flow of $4\,\mathrm{l\,min^{-1}}$ is sucked through the outer nozzle. The orifice at the end of the inner nozzle accelerates both flow rates including particles, which are centered in the inner flow. Due to their low inertia, smaller particles adopt faster to the increased flow velocity than larger particles do. Directly after the second nozzle, the time of flight is measured when a particle passes two laser beams. From the time of flight, the aerodynamic particle diameter is achieved by a calibration function, which was done by the manufacturer using PSL particles.

The counting error of the APS is given in the user manual to 10%. Additionally, for high particle number concentrations $> 10^3$ cm^{-3} for the size range larger than 500 nm, the probability of coincident errors increases. For the present measurements with much lower particle number concentrations, coincident errors did not occur. Sizing of the APS was checked prior the campaign using PSL particles with $dp_{ve} = 800$, 1000, and 2000 nm that corresponds to $dp_a = 820$, 1025, and 2050 nm using a PSL density of $\rho_p = 1050\,\mathrm{kg\,m^{-3}}$. The measured PNSD by the APS is shown in Figure 4.4(b) - (d). A lognormal size distribution was fitted to the latex peaks. The free parameters of the lognormal size distribution

$$\frac{dN}{d\log dp} = \frac{N}{\sqrt{2\pi}\log\sigma_g}\exp\left(-\frac{(\log dp - \log d_{gN})^2}{2(\log\sigma_g)^2}\right) \tag{4.4}$$

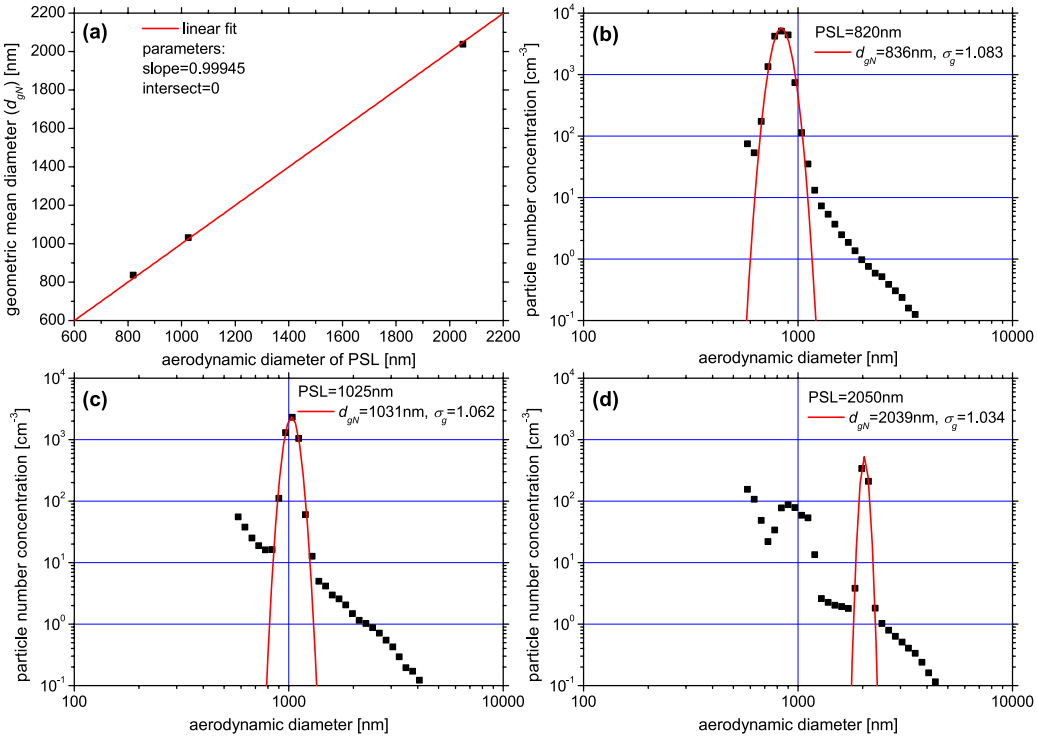

Figure 4.4: *(a) Scatter plot and linear fit of nominal aerodynamic diameter of latex particles and geometric mean diameter of fitted particle modes of measured latex PNSD (b) - (d).*

are the total particle number concentration N, the geometric mean diameter d_{gN}, and the geometric standard deviation σ_g. Plotting each d_{gN} to the nominal aerodynamic diameter of the latex sphere as shown in Figure 4.4(a) indicates that the calibration of this instrument is excellent (slope = 1).

4.1.2 Data processing of the DMPS and APS

Before the recorded DMPS number concentrations were corrected for multiple charged particles in the APS size range, they were converted to a uniform particle diameter. Since the DMPS and APS measure particles according to different physical methods, a formula given in DeCarlo *et al.* (2004) was used that converts volume equivalent (dp_{ve}) to mobility particle diameters:

$$dp_m = dp_{ve}\chi\frac{C_c(dp_m)}{C_c(dp_{ve})}, \tag{4.5}$$

and volume equivalent to aerodynamic particle diameters:

$$dp_a = dp_{ve}\sqrt{\frac{1}{\chi}\frac{\rho_p}{\rho_0}\frac{C_c(dp_{ve})}{C_c(dp_a)}}, \tag{4.6}$$

where χ is the dynamic shape factor, ρ_p the dry particle density, and ρ_0 the reference density of $1000\,\mathrm{kg\,m^{-3}}$. For simplification, it is assumed that in the DMPS size range the particles are spherical, meaning $\chi = 1$ and $dp_{ve} = dp_m$. The APS measures in the size range of the

continuum regime[2], where $C_c(dp_{ve}) = C_c(dp_a)$ and equation 4.6 simplifies to

$$dp_{ve} = dp_a \sqrt{\frac{1}{\rho_{eff}}}. \tag{4.7}$$

In equation 4.7, an effective density

$$\rho_{eff} = \frac{\rho_p}{\rho_0 \chi} \tag{4.8}$$

is introduced to investigate differences in the conversion from aerodynamic to volume equivalent diameter for prevailing particle components in the APS size range. As seen from the mixing state (cf. chapter 4.2.3 and 4.2.4), particles in the APS size range are an externally mixture of hydrophobic dust and hygroscopic sea-salt. A dry particle density $\rho_p = 2170\,\mathrm{kg\,m^{-3}}$ for the hygroscopic fraction was estimated, using the average mineralogical composition from the single particle analysis of the most frequent three inorganic salts (see Figure 5.4) and particle densities (Table 2.1). The dynamic shape factor was assumed to be $\chi = 1.08$, which is the value of cubic sodium chloride particles in the continuum regime (Gysel *et al.*, 2002; Kelly and McMurry, 1992).

The dry density for dust particles was determined to a range of $\rho_p = 2450 - 2700\,\mathrm{kg\,m^{-3}}$ over the Cape Verde Islands (Haywood *et al.*, 2001) and near the Saharan desert during SAMUM-1 (Kandler *et al.*, 2009). The dry dynamic shape factor was reported to $\chi = 1.25$ (Kaaden *et al.*, 2009) for one micrometer sized Saharan dust particles. The overall effective density of the sea-salt and dust fraction is approximately 2. Without any knowledge of the actual mixing state of sea-salt and dust, the dry APS diameters were converted into volume equivalent diameters using $\rho_{eff} = 2$.

As proposed by Schladitz *et al.* (2009), the DMPS number concentration is biased by multiple charged particles (APS size range particles), when the particle number concentration in the APS size range exceeds $50\,\mathrm{cm^{-3}}$. To remove these multiple charged particles, a procedure described in Birmili *et al.* (2008) and Schladitz *et al.* (2009) was used, applying the measured APS number size distribution. Afterwards, the DMPS dataset was smoothed with a three point floating average to remove rapid changes in the particle number concentration. The corrected DMPS mobility distributions were then inverted using the regular inversion algorithm from Stratmann and Wiedensohler (1996). The inversion algorithm accounts for the DMA-specific area of the transfer function, the CPC counting efficiency for the operated CPC sample flow (see chapter 4.1.1), and the bipolar charge distribution in the DMPS size range. Finally, the DMPS and APS data were merged to obtain one PNSD in $\frac{dN}{d\log dp_{ve}}$ ranging from 26 nm to 10μm with equally spaced lognormal intervals.

[2]Flow is governed by the macroscopic properties of the gas or fluid such as viscosity and density

4.2 Humidified particle number size distribution, hygroscopic growth, and state of mixing

4.2.1 HDMPS and HAPS

The measurement technique for the humidified PNSD is similar to that for the dry PNSD. The Humidifying Differential Mobility Particle Sizer (HDMPS) measures the PNSD in the size range from 26 nm $< dp_m <$ 900 nm for discrete RHs, which can be varied in the range between 30% and 90% RH (Birmili *et al.*, 2009). The adjacent size range was measured with a humidified APS (HAPS) at a constant RH-level. The HAPS was especially developed for this field experiment.

HDMPS

The HDMPS is described in detail in the doctoral thesis by Nowak (2006). A simplified principle of the HDMPS setup is given in Figure 4.5. In step I, a Nafion^{TM} pre-humidifier

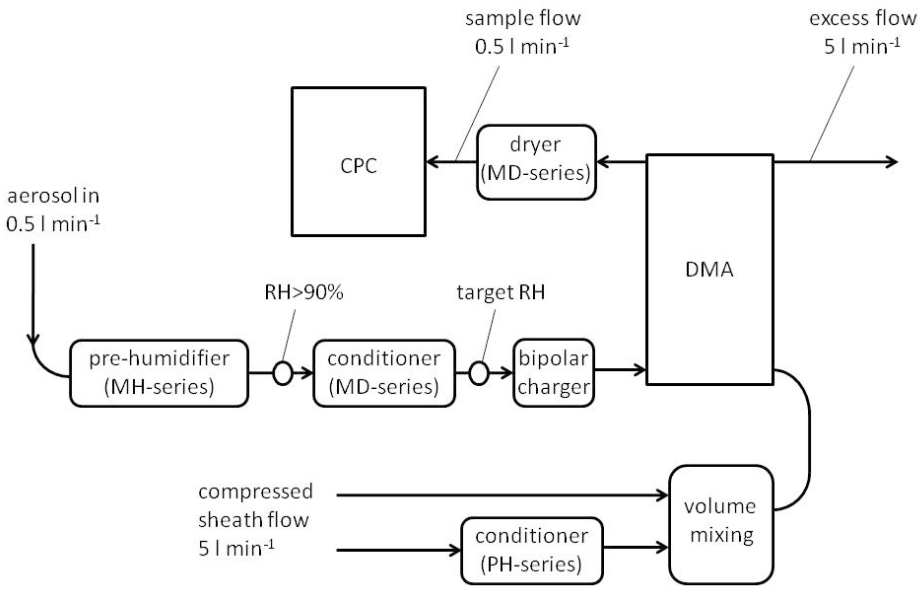

Figure 4.5: *Simplified design of the HDMPS.*

(MH-series, ANSYCO Inc., Karlsruhe, Germany) humidifies the aerosol with a flow rate of $Q_{aerosol} = 0.5\,\mathrm{l\,min^{-1}}$ to approximately 90% RH. This process humidifies the particles above the known deliquescence point of most of the abundant aerosol species (Nowak, 2006; Birmili *et al.*, 2009). In step II, an aerosol conditioner (MD-series, ANSYCO Inc., Karlsruhe, Germany) dries the sample aerosol to the target RH following the upper (metastable) branch of the hysteresis of hygroscopic growth in Figure 2.3. The reason for conditioning the aerosol to the same relative humidity conditions (and size) as in the subsequent classification in the DMA, is to obtain the correct bipolar charge distribution. The particle-free

sheath air in the DMA with a flow rate of $Q_{sheath} = 5\,\mathrm{l\,min^{-1}}$ is kept at the same RH. In step III, particles were classified in the DMA. Downstream of the DMA, the quasi-monodisperse sample aerosol is again dried to RH $< 30\%$ in order to prevent accumulation of water inside the butanol reservoir of the condensation particle counter. In a last step, the particles were counted by a CPC (CPC model 3010 / Serial no. 2254 , TSI Inc., St. Paul, USA). The time required for a whole cycle of three PNSD scans at a certain RH is about 30 min. During the measurement campaign, this cycle was repeated for 4 different RHs, which were RH = 30, 55, 75, and 90%. Adding the time for RH stabilization between each change in RH, the complete characterization of the aerosol required about three hours across the operated relative humidities .

Humidity and temperature sensors (HMP230, Vaisala Inc., Vantaa, Finland) were used within the HDMPS. All humidity sensors (2 sensors for regulation of aerosol and sheath air flow, 2 sensors for monitoring sample and excess air flow) were calibrated prior the measurement campaign with a dew point mirror sensor (DewPrime II Dew Point Hygrometer, Model 2002, Edge Tech, Marlborough, USA). The sizing of the HDMPS was calibrated with ammonium sulfate particles at the operational relative humidities as follows: During

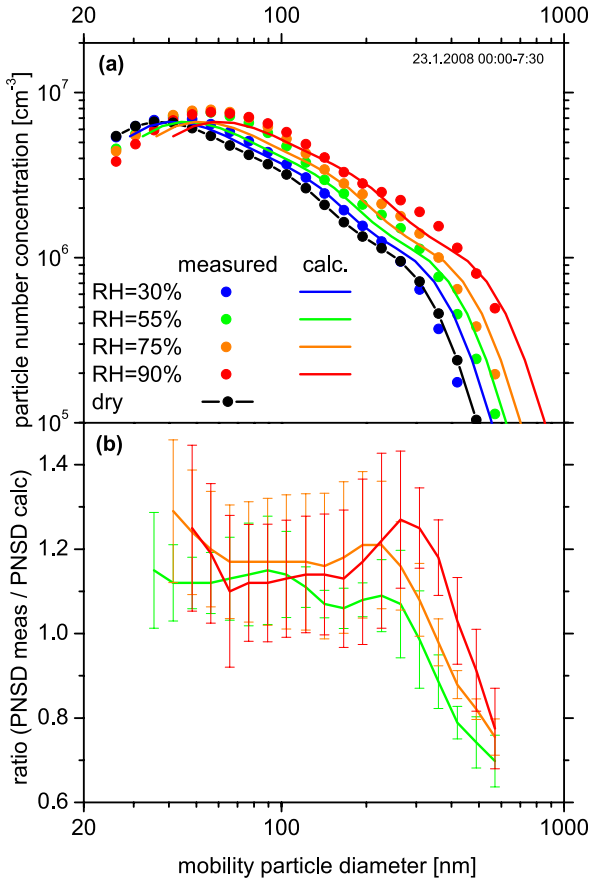

Figure 4.6: *(a) Measured (dots) and calculated (solid lines) PNSDs of ammonium sulfate at 30, 55, 75, and 90% RH. (b) Size-dependent correction functions for the HDMPS at 55, 75, and 90% RH.*

the calibration procedure, the HDMPS measured the size distribution of ammonium sulfate particles at 30, 55, 75, and 90% RH, while the DMPS measured the dry PNSD simultaneously. With modified Köhler theory (Tang and Munkelwitz, 1994; Tang, 1996) (see Chapter 2.2.1), the hygroscopic growth factor of ammonium sulfate for each size bin of the dry PNSD was calculated. According to equation 2.26, the wet diameter and hence the wet PNSD were calculated for each RH given above and compared with the measured wet PNSD of the HDMPS. For illustration, Figure 4.6(a) shows the HDMPS calibration from January 23.

In a last step, size- and RH-dependent correction functions were calculated, which are defined as the ratio of the measured wet PNSD to the calculated wet PNSD. The correction functions include differences between the DMPS and HDMPS with respect to size dependent counting efficiencies of the CPCs, particle losses in the sampling lines, and sizing by the two DMAs. Figure 4.6(b) shows arithmetic mean values ± single standard deviation of four independent HDMPS calibrations performed on January 19, 22, 31 and February 9. There is a significant deviation from unity for $dp_m < 300\,\text{nm}$. The correction functions decrease with increasing particle size and show also a slight RH dependency. The HDMPS correction functions were considered in data evaluation.

HAPS

The HAPS is a novel instrument that consists in principal of a humidification unit and a commercial APS (APS model 3321 / Serial no. 1223, TSI Inc., St. Paul, USA). The principle of the HAPS is shown in Figure 4.7. The humidification unit for sheath and

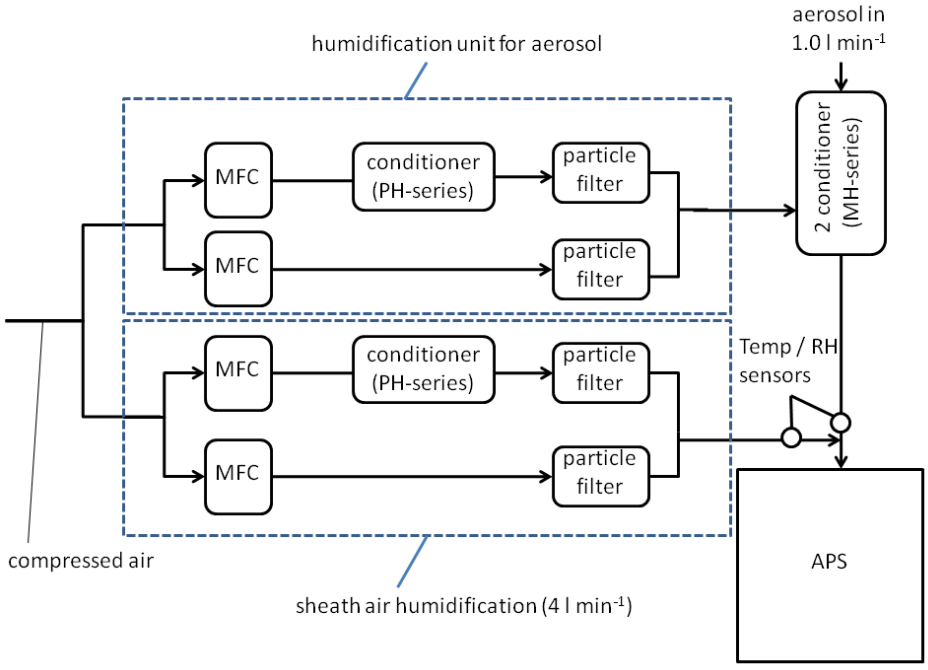

Figure 4.7: *Design of the HAPS.*

aerosol air is similar to the HDMPS, except for the pre-humidifier. The mixing of wet and dry sheath and aerosol air to a set point RH of 85% was achieved by manual adjusting the flows via needle valves. The humidity sensors for aerosol and sheath air were calibrated prior the measurement campaign with the dew point mirror sensor. The HAPS calibration was done in the same way as the HDMPS calibration exemplified in subsection HDMPS. Figure 4.8(a) shows an ammonium sulfate calibration from January 21 and (b) the average size-dependent correction function ± single standard deviation of four independent HAPS calibrations performed on January 21, 22 and February 3, 10. The correction function

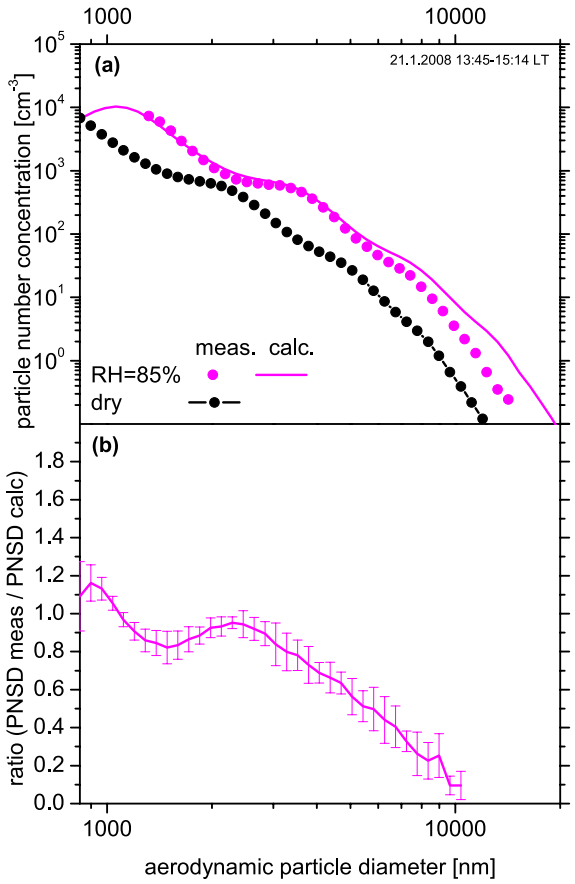

Figure 4.8: *(a) Measured (dots) and calculated (solid lines) PNSDs of ammonium sulfate at 85% RH. (b) Size-dependent correction function for the HAPS at 85% RH.*

includes different counting efficiencies between the two APS, different particle losses in the sampling lines relative to the dry APS, and RH changes of the aerosol inside the HAPS. For aerodynamic diameters >2000 nm the correction function decreases, because of the conditioner unit, the sampling path to the HAPS is longer than for the APS and thus causes higher particle losses. Another process, causing the decreasing correction function, is a droplet distortion effect that becomes very significant above 2000 nm. The HAPS correction function was considered in data evaluation.

Table 4.1: *Growth factor correction factor for the selected dry mobility diameters.*

initial dry diameter	GF correction factor
30 nm	0.9446
50 nm	0.9634
80 nm	0.977
150 nm	0.9936
250 nm	1.0542
350 nm	1.0207

4.2.2 HTDMA

To determine the hygroscopic growth and mixing state for certain particle sizes, a Hygroscopicity Tandem Differential Mobility Analyzer (HTDMA) technique (Liu *et al.*, 1978) was used. A first DMA selects a quasi-monodisperse aerosol, while the CPC measures the particle number concentration. Downstream, the quasi-monodisperse aerosol is conditioned to a target RH, typically above the DRH of common inorganic salts in the atmosphere. The subsequent humidified size distribution of the quasi-monodisperse aerosol is measured by a combination of a second DMA and CPC. From this size distribution, hygroscopic growth factors and number fractions can be achieved for externally mixed particle groups. The setup of the HTDMA used here is explained in detail in Massling *et al.* (2007). During the measurement campaign, hygroscopic growth distributions were measured for particles with dry mobility diameters of $dp_m = 30$, 50, 80, 150, 250, and 350 nm at RH = 85%. The selected RH is an appropriate compromise to guarantee that all particles exceeded the deliquescence point and growth distributions of more hygroscopic components will completely be resolved by the second DMA, especially at the largest initial dry diameter. The measurement error of the HTDMA mainly depends on the uncertainty in measuring and controlling the RH within the system (Massling *et al.*, 2010). Therefore, all RH sensors were calibrated with the dew point mirror sensor prior the measurement campaign. The sizing accuracy of the entire HTDMA and a size shift between the two DMAs were checked before the campaign by selecting atomized ammonium sulfate particles at RH < 20%. A growth factor correction factor was calculated for each initial dry diameter employing the inversion toolkit for TDMA measurements (TDMAinv, Gysel *et al.* (2009)). The GF correction factors in Table 4.1 are the ratios of the initial dry diameters and the peak diameter measured by the second DMA.

4.2.3 Data processing of the HTDMA

Hygroscopic growth distributions were evaluated with the TDMAinv inversion toolkit (Gysel *et al.*, 2009). This algorithm considers the growth factor correction factors given in Table 4.1. For deriving the hygroscopic growth distribution, a tolerance range of 3% to the set point of RH = 85% was allowed. In a later stage of data evaluation, hygroscopic growth distributions

were corrected to the set point RH using an empirical formula (Equation 3 in Gysel *et al.* (2009)). This empirical formula is based on the κ-Köhler theory. Figure 4.9 shows an example of a hygroscopic growth distribution of an externally mixed aerosol at Cape Verde in terms of hygroscopic growth. In analogy to Swietlicki *et al.* (2008), the minimum in the

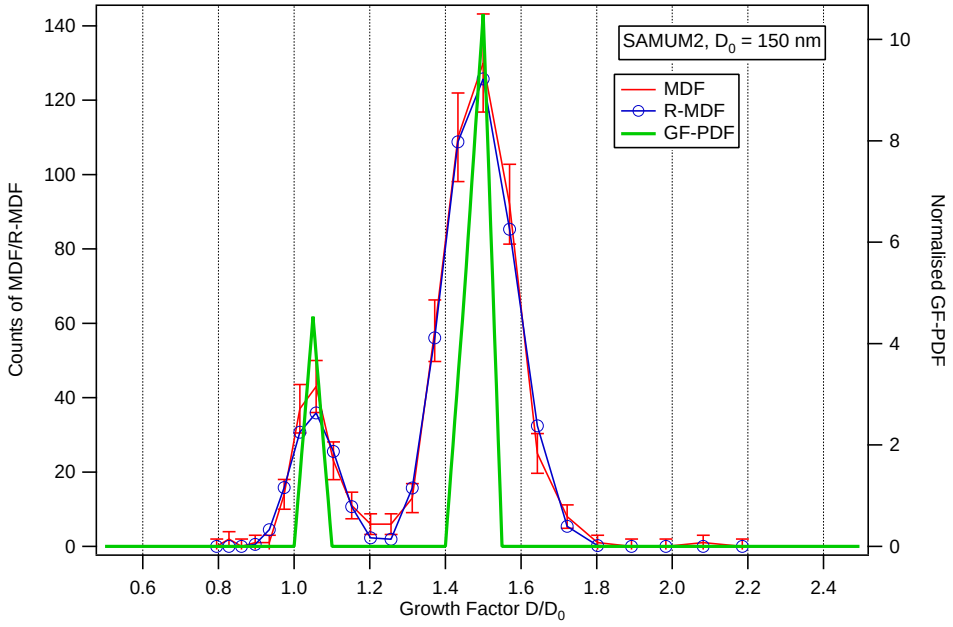

Figure 4.9: *Typical hygroscopic growth factor distribution derived from the HTDMA (red solid line). The example shows also the retrieved normalized growth factor probability density function (green solid line) after application of the TDMAinv program for an initial dry diameter of* $dp_m = 150\,nm$.

hygroscopic growth distribution splits the particles into a fraction of hydrophobic particles ($GF < 1.2$, hydrophobic particle mode) and hygroscopic particles ($GF > 1.2$, hygroscopic particle mode). The mean number fractions and their corresponding mean hygroscopic growth factors were determined by integration of the normalized growth factor probability density function (GF-PDF) in defined GF ranges given above.

Similar to the DMPS, the HTDMA results are based on mobility diameters. The instrument may classify singly as well as multiply charged particles in the same mobility diameter bin. A correction for multiple charges selected by the first DMA in the HTDMA is not possible, since the first DMA selects only discrete diameters of the whole particle size spectrum. However, with the simultaneous measurement of the PNSD, the error can be quantified. Duplissy *et al.* (2009) pointed out, if the fraction of singly charged particles in the first DMA is $< 80\%$, the HTDMA data are erroneous and should be excluded from the dataset. The fraction of singly charged particles was determined using the DMPS data for each initial diameter selected by the HTDMA. The fraction of singly charged particles is defined as the ratio of the particle number concentration of a certain particle diameter of singly charged particles to the particle number concentration of a certain particle diameter from the mobility size distribution. Figure 4.10 shows a time series of the fraction of singly charged particles for the selected initial dry mobility diameters of the HTDMA. The figure also

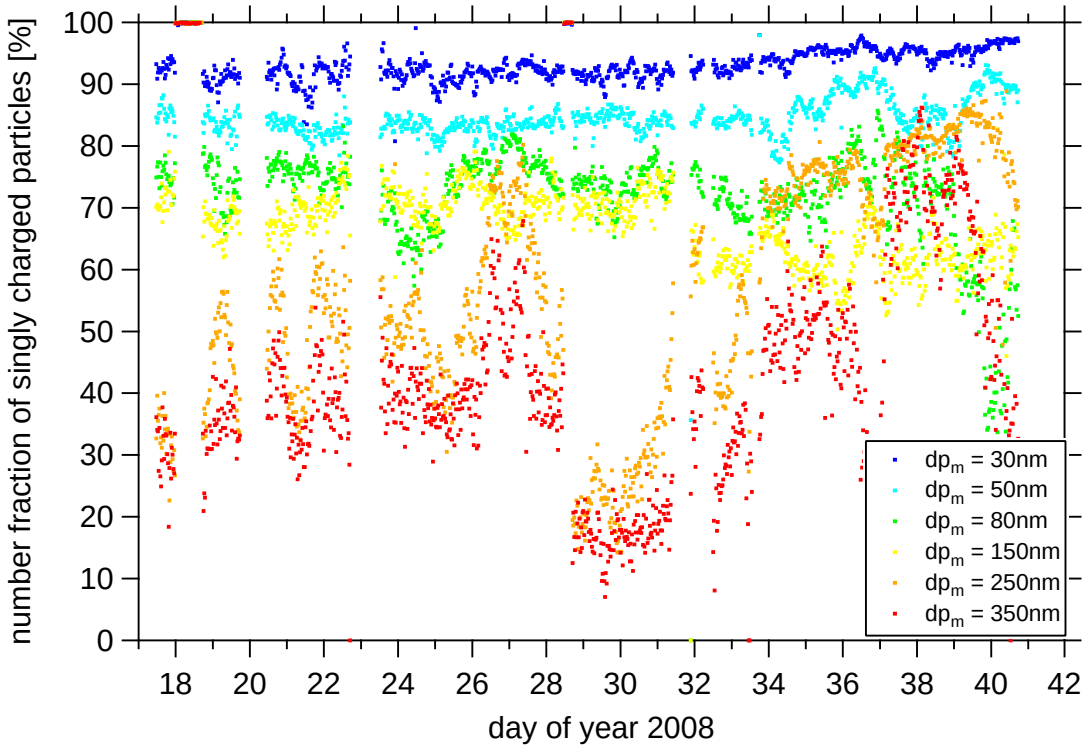

Figure 4.10: *Time series of number fraction of singly charged particles derived from DMPS data.*

reveals fractions of singly charged particles much smaller than 80% for initial dry diameters with $dp_m = 150$, 250 and, 350 nm during the dust dominated periods DOY 24.5 - 26.5 LT and 28 - 34 LT (cf. Figure 5.5). Assuming that the multiply charged particles in the HTDMA are mainly hydrophobic mineral dust particles, the mean number fraction of hydrophobic particles is measured higher than in reality. It follows that the mean hydrophobic number fraction and hence the mean hygroscopic number fraction are more biased than the respective mean GFs. For further analysis, the biased mean number fractions were excluded from the HTDMA data.

4.2.4 Data processing of the HDMPS and HAPS

The objective of this section is to derive a time series of RH-dependent mean hygroscopic growth factors and their corresponding mean number fractions in the size range from 26 nm $< dp_{ve} < 10\mu$m by using the HDMPS, HAPS, and HTDMA data and the dry PNSD. To achieve this aim, it was necessary to solve several substantial problems:

- The information of the time-dependent hygroscopic mixing state is absent in the size range from 150 nm $< dp_{ve} < 10\mu$m.
- The HAPS measured the humidified aerodynamic PNSD. In combination with the aerodynamic PNSD at dry conditions, an average aerodynamic growth factor was determined. A conversion from aerodynamic to volume equivalent growth factor has to be carried out.

- The HDMPS measured the humidified number size distribution and thus in combination with the DMPS it measured an average GF at 30, 55, 75, and 90% RH, whereas the HAPS was operated only at 85% RH. The problem to combine both to one humidified PNSD at the same RH has to be solved.

- The HDMPS data has to be corrected for multiply charged particles. Therefore, information about the PNSD at 30, 55, 75, and 90% RH in the APS size range is required.

- The summation method is a statistical method and was developed to derive an average GF from HDMPS and DMPS data. It can only be applied, if the particle number concentration falls beneath a certain threshold value at the upper or the lower end of the PNSD. If not, the summation method would disregard a significant number of particles outside the measurement range of the HDMPS. Hence, the problem to apply the summation method to the HDMPS data has to be solved.

Applying "summation method" to calculate the average aerodynamic growth factor using HAPS and dry APS data

In a first step, the measured HAPS data were corrected with the correction function shown in Figure 4.8(b). A statistical model called "summation method" (Birmili *et al.*, 2004) was used to derive the average aerodynamic growth factor from HAPS and APS data. The "summation method" was developed to calculate average growth factors from HDMPS and DMPS data. Until now, the summation method was applied in numerous research projects, e.g., PRIDE-PRD2004 and CAREBeijing-2006 in China (Eichler *et al.*, 2008; Achtert *et al.*, 2009) and in a Finnish boreal forest (Birmili *et al.*, 2009). Here, the principle of the summation method was applied to the HAPS and APS data. The summation method was deployed in the following:
The number concentrations of the HAPS and APS were summed bin-wise starting at the upper end of the PNSD, ranging from $835\,\mathrm{nm} < dp_a < 19.81\,\mu\mathrm{m}$. The obtained cumulative PNSDs were divided into logarithmically equidistant levels of cumulative number concentrations, since the cumulative PNSDs cover multiple orders of magnitude. The logarithmic equidistant levels of the dry and wet cumulative PNSD are identical. Finally, to each logarithmic equidistant level, a certain dry and wet particle diameter was attributed. The ratio of the wet to the dry particle diameter (cf. equation 2.26) defines the average aerodynamic hygroscopic growth factor. This procedure was applied to each logarithmic equidistant level obtaining the average aerodynamic hygroscopic growth factor as a quasi-continuous function of the dry particle size. Nevertheless, Birmili *et al.* (2004, 2009) refer to some restrictions concerning the summation method.

1. No dry particle of a smaller size reaches a larger wet diameter than a dry particle of a larger size (i.e. no overtaking during the humidification process).

2. The average hygroscopic growth factor varies only slowly with particle size.

3. The summation method requires the assumption that the total particle number concentration of the PNSD remains constant during the humidification process. The conservation of particle number requires that particles are neither produced nor lost.

For the present measurements, item 1 is fulfilled since the hygroscopic mixing state (Figure 4.9) offers only one hygroscopic particle mode. As it will be shown in Figure 5.4, the apparent hygroscopic material from the mineralogical composition shows no abrupt change with particle size and therefore item 2 is fulfilled. To meet item 3, a maximum variation of ±15% (Nowak, 2006) of the total number concentration ratio was allowed. This maximum variation was chosen, since it considers the counting error of both APS.
For data analysis, a tolerance range of ±5% in RH (cf. 3% for the HDMPS data) to the set point of RH = 85% was allowed. The larger tolerance range was chosen due to manual adjusting to the set point RH of the HAPS. The average growth factors were then corrected to the set point RH using the κ-parametrization.

Extrapolation of HTDMA derived mean growth factors in the size range $dp_{ve} > 350\,\mathrm{nm}$ and κ-parametrization

To address the problems stated in bullet points 1 and 2 on page 36 (information of time dependent hygroscopic mixing state in the size range from 150 nm to 10 μm and conversion from aerodynamic to volume equivalent growth factor), information about the mean hygroscopic growth factors in the size range 350 nm $< dp_{ve} <$ 10μm is needed. For this case, it was proven to use the mean hygroscopic growth factors from the HTDMA. Figure 4.11 shows a box plot of the mean hygroscopic growth factors of the hydrophobic and hygroscopic mode for the entire time period. Hygroscopic growth factors from literature for sea-salt during ACE-Asia (Massling *et al.*, 2007) and for more hygroscopic particles during ARIADNE at Crete (Stock, 2006) are added. The hygroscopic growth factors during ACE-Asia were measured at RH = 90% and were recalculated to RH = 85% for comparison. Additionally, growth factors for mineral dust measured during SAMUM-1 (Kaaden *et al.*, 2009) are plotted into Figure 4.11. The literature values lie within the 10$^{\mathrm{th}}$ and 90$^{\mathrm{th}}$ percentile of the HTDMA growth factors measured at $dp_{ve} = 350$ nm. Therefore, the time series of the HTDMA derived mean growth factors at $dp_{ve} = 350$ nm was used to describe the mean hygroscopic growth factors in the size range 350 nm $< dp_{ve} <$ 10μm.
Subsequently, the mean hygroscopic growth factors were parameterized according to RH at RH = 85% using the single parameter κ formalism (equation 2.28) and were interpolated to the size bins of the discrete dry PNSD.

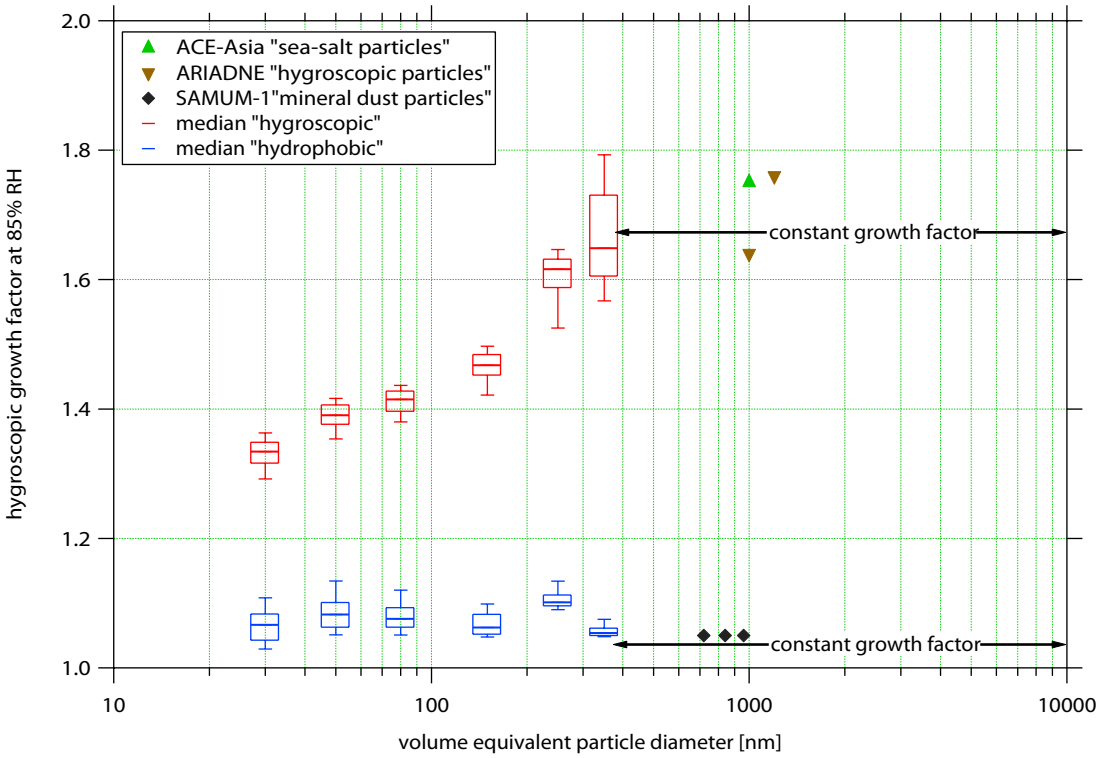

Figure 4.11: *Box plot of mean hygroscopic growth factors from HTDMA at 85% RH. Growth factors for mineral dust (black markers), hygroscopic particles at the Mediterranean Sea (brown markers) and for sea-salt (green marker) are added.*

Calculation of number fractions in the APS size range

In the following, problems stated in bullet points 1 and 2 on page 36 (information of time dependent hygroscopic mixing state in the size range from 150 nm to 10 μm and conversion from aerodynamic to volume equivalent growth factor) will be further addressed. To combine mean hygroscopic growth factors with the average growth factor, a formula for the average hygroscopic growth factor is introduced as (e.g., Meier *et al.* (2009)):

$$\overline{GF}^3 = \sum_i nf_i \cdot GF_i^3, \tag{4.9}$$

where GF_i are the mean GFs and corresponding mean number fraction nf_i of the hygroscopic and hydrophobic mode (i = 2), respectively. Rearranging equation 4.9 and using the expression $nf_{hyd} = 1 - nf_{hyg}$, the mean hygroscopic number fraction can be written as:

$$nf_{hyg} = \frac{\overline{GF}^3 - GF_{hyd}^3}{GF_{hyg}^3 - GF_{hyd}^3}. \tag{4.10}$$

The easiest way would be, to calculate an average growth factor from the measured average aerodynamic growth factor. However, this is not possible, because an average particle density at RH = 85% is unknown. In turn, the average particle density depends on the actual mixing state of mineral dust and sea-salt, which is actually also unknown. For this

case, a formula is essential to convert the growth factors into aerodynamic growth factors first. The aerodynamic growth factor is defined (cf. equation 2.26) as:

$$GF_a(RH) = \frac{dp_a(RH)}{dp_a(dry)}. \tag{4.11}$$

Combing equations 4.11, 4.7, and 2.26 and introducing the solution droplet density and the dynamic shape factor at a certain RH, one obtains the following expression:

$$GF_a(RH) = GF \cdot \sqrt{\frac{\rho(RH) \cdot \chi}{\rho_p \cdot \chi(RH)}} \tag{4.12}$$

with the unknown parameters $\rho(RH)$ and $\chi(RH)$. Obviously, after humidification a hygroscopic particle is spherical, and therefore, $\chi(RH = 85\%) = 1.0$. The solution droplet density at a certain RH is calculated using a volume mixing rule (e.g., Leinert and Wiedensohler (2008)):

$$\rho(RH) = \frac{1}{GF^3} \cdot \rho_p + (1 - \frac{1}{GF^3}) \cdot \rho_w. \tag{4.13}$$

Combining equations 4.12 and 4.13 leads to a formula to calculate aerodynamic growth factors from the mean GFs in the APS size range:

$$GF_a(RH) = \sqrt{\frac{\chi + \frac{\chi \cdot \rho_w}{\rho_p}(GF^3 - 1)}{\chi(RH) \cdot GF}}. \tag{4.14}$$

Now, all information needed to calculate the mean hygroscopic and hydrophobic number fractions in the APS size range by replacing in equation 4.10 the respective GF to GF_a as:

$$nf_{hyg} = \frac{\overline{GF_a}^3 - GF_{a,hyd}^3}{GF_{a,hyg}^3 - GF_{a,hyd}^3}. \tag{4.15}$$

In equation 4.15, $\overline{GF_a}$ is the measured average aerodynamic hygroscopic growth factor and $GF_{a,hyd}$ and $GF_{a,hyd}$ are the calculated mean aerodynamic hygroscopic growth factors (hydrophobic and hygroscopic mode) from equation 4.14.

Calculation of PNSD at 30, 55, 75, and 90% RH in the APS size range and merging with humidified PNSD from HDMPS

This section addresses problems stated in bullet points 3 and 4 on page 36 (HDMPS / DMPS measured an average GF, while the HAPS was operated at 85% RH and HDMPS data has to be corrected for multiply charged particles).
By using the derived κ values, the mean hygroscopic growth factors were calculated at 30, 55, 75, and 90% RH in the APS size range based on the growth factors at 85% RH. Afterwards, the average hygroscopic growth factor was calculated at the 4 RHs applying equation 4.9. Finally, the PNSDs at 30, 55, 75, and 90% RH in the APS size range were calculated, by

multiplying the dry PNSD bin-wise with the respective RH-dependent average hygroscopic growth factor.
The HDMPS raw data were classified into different RH intervals of RH = 30±3%, RH = 55± 3%, RH = 75±3%, and RH = 90±3%. Secondly, the multiple charge correction (APS size range particles) was applied using the PNSD at 30, 55, 75, and 90% RH in the APS size range. Thirdly, the HDMPS data were inverted using the regular inversion algorithm by Stratmann and Wiedensohler (1996). Fourthly, the humidified PNSDs in the HDMPS size range were corrected using the RH-dependent correction functions shown in Figure 4.6(b). Finally, the humidified PNSDs at 30, 55, 75, and 90% RH in the HDMPS and in the HAPS size range were merged to final PNSDs ranging from 26 nm $< dp_{ve} <$ 10μm.

Applying the "summation method" to calculate the average hygroscopic growth factor in the size range from 26 nm $< dp_{ve} <$ 10μm

This section gives an answer to the problem outlined in bullet point 5 on page 36 (conservation of total particle number concentration).
The "summation method" was applied to obtain the average hygroscopic growth factor at 4 RHs in the size range from 26 nm $< dp_{ve} <$ 10μm. Therefore, cumulative PNSDs were obtained starting again at the upper end of the PNSD, but now ranging from 26 nm $< dp_{ve} <$ 10μm. The derived average hygroscopic growth factor was corrected to the respective set point RH using the κ-parametrization. The statistical evaluation of the HDMPS data claims conservation for the total particle number concentrations when the particles are humidified from the dry to the wet state. Hence, in most of the time, this demand is however not fulfilled. For this case, a maximum deviation of the total particle concentrations of 15% was allowed.
At this stage of data processing, a comparison of different methods to retrieve average hygroscopic growth factors is shown. The first method to derive average GFs is to use the HTDMA, while the second method is based on a statistical evaluation (summation method) of the HDMPS data. The HTDMA derived growth factor probability density function (GF-PDF)at RH = 85% was recalculated to RH = 90% using the κ-parametrization. Afterwards, the normalized (GF-PDF) was integrated over the full GF range to yield an average GF. Figure 4.12 shows an intercomparison of average GFs of the six selected initial diameters by the HTDMA. Generally, $\overline{GF}$ for dp_{ve} = 150, 250, and 350 nm lie on the 1:1 line, while $\overline{GF}$ for dp_{ve} = 30, 50, and 80 nm of the HDMPS method underestimate the HTDMA derived average GFs. Considering the smallest 3 selected diameters (dp_{ve} = 30, 50, and 80 nm), the deviation from the 1:1 line is largest for the smallest particles. This behavior is also the case in Meier *et al.* (2009) in their Figure 7, and is an artefact of the "summation method". Due to the maximum variation of the particle number concentration of ±15% and summing-up the particle concentration from the upper end of the PNSD, the "summation method"

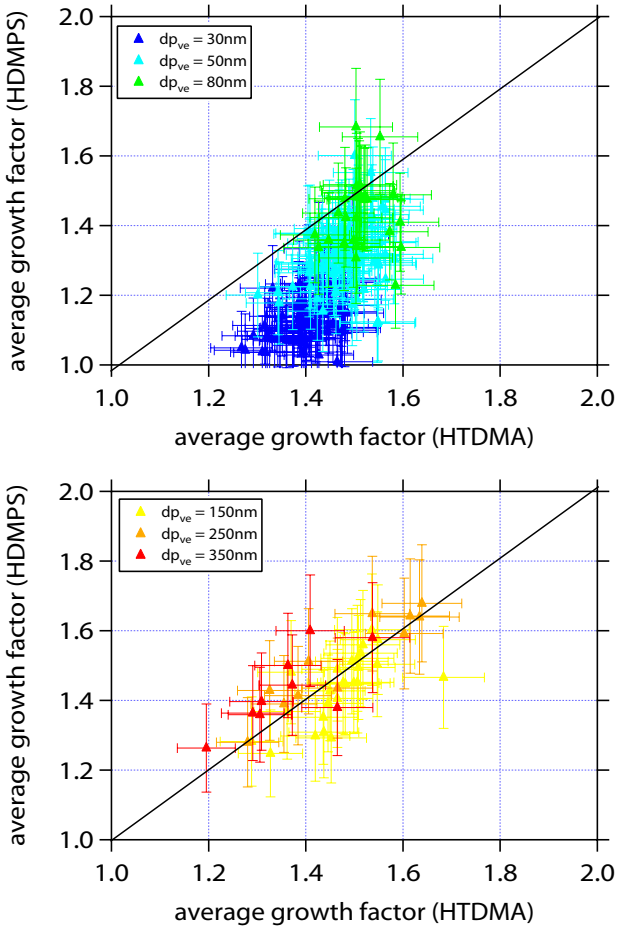

Figure 4.12: *Intercomparison of average growth factors from HTDMA and HDMPS data at RH = 90% for different volume equivalent particle diameters. Values from HTDMA are disregarded, where the fraction of singly charged particles drops below ∼ 80%. Error bars for average growth factors from HDMPS (10%) and HTDMA (5%) are added.*

causes an underestimation of average GF for the smallest diameters.

Calculation of number fractions in the intermediate size range from 150 nm $< dp_{ve} <$ 570nm

This section addresses the problem discussed in bullet point 1 on page 36 (information of time dependent hygroscopic mixing state in the size range from 150 nm to 10 μm). Due to the exclusion of biased HTDMA mean number fractions at dp_{ve} = 150, 250, and 350 nm, quasi-continuous mean number fractions are only available in the size range from 30 nm $< dp_{ve} <$ 80nm. Quasi-continuous mean number fractions in the size range $dp_{ve} >$ 570 nm are derived by calculations based on the HAPS data exemplified above. The mean number fractions in the intermediate size range were calculated according to equation 4.10, using the size resolved average GFs from the HDMPS and the corresponding mean hygroscopic growth factors.

Error discussion of growth factors, κ values, and number fractions

After diverse calibrations and corrections, the remaining uncertainty of the mean hygroscopic growth factors depends mainly on the uncertainty in RH within the HTDMA system. At 90% RH, the manufacturers give absolute uncertainties of 1% for the humidity sensors, and 0.5% for the dew point mirror sensor, respectively. An overall uncertainty of 5% for GFs as well as for κ values was estimated, when the HTDMA growth factors were corrected to the set point RH as shown in Gysel *et al.* (2009) in their Figure 6. This uncertainty for the mean GFs is in agreement with reported values from HTDMA measurements by Massling *et al.* (2009).

The uncertainty of the mean number fractions for $dp_{ve} <$ 150 nm results from the HTDMA, while the uncertainty for $dp_{ve} >$ 150 nm results from average GFs as well as from uncertainties of mean GFs. To estimate the uncertainty of the number fractions for $dp_{ve} >$ 150 nm, the uncertainty of the average GF needs to be quantified.

The average GF uncertainty is composed of uncertainties in RH and deviations in the PNSD. Here, deviations of up to ±15% in the total particle concentration of the dry and humidified PNSD involve the largest source of error. Since the average deviations of the total particle number concentrations are even smaller, an average GF uncertainty of 10% from HDMPS and HAPS derived data was estimated.

Applying error propagation, the uncertainty for the mean number fractions in the size range $dp_{ve} >$ 150 nm is about 24%.

4.3 Extinction coefficient

4.3.1 Visibility sensor

The visibility sensor (VPF 710, Biral, Bristol, UK) is a meteorological instrument, to determine the visibility in the range from 10 m - 75 km ($3.0 \cdot 10^{-1}\mathrm{m}^{-1} > \sigma_e > 4.0 \cdot 10^{-5}\mathrm{m}^{-1}$, Biral

user manual) at e.g., roadside stations, airports, and automatic weather stations in hazy and foggy conditions. In this work, the visibility sensor was used to measure the reduction in visibility caused by aerosol particles at ambient (atmospheric) conditions. This is possible, since fog, drizzle or rain did not appear during the campaign. The visibility sensor consists of a transmitter and receiver unit with the sample volume in between (Figure 4.13).

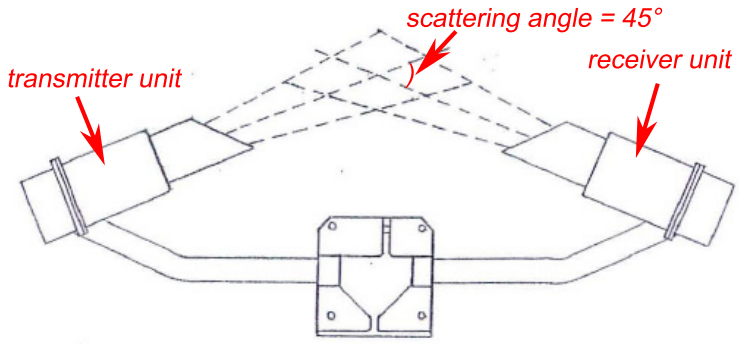

Figure 4.13: *Top view of the visibility sensor, showing transmitter and receiver unit. The dashed lines illustrate the light paths of transmitted and scattered light, enclosing by the scattering angle θ. (modified figure from Biral user manual)*

The transmitter unit emits infrared light at a wavelength of $\lambda = 880\,\text{nm}$. The transmitter unit is rotated with respect to the receiver unit at about 45°, to ensure that only scattered light with a scattering angle of $\theta = 45 \pm 6°$ is measured by the receiver unit. Hence, this visibility sensor is classified as a forward scatter meter (FSM), which measures the amount of light scattered at scattering angles less than 90°. However, the internally stored calibration constant converts the measured receiver signal into an extinction coefficient, but this is only valid for fog (Biral user manual) and is unfortunately unknown.
The accuracy of the instrument given in the user manual decreases with decreasing atmospheric extinction (increasing visibility) and is smaller than 10% for $\sigma_e > 1.87 \cdot 10^{-4}\text{m}^{-1}$ and smaller than 20% for $\sigma_e > 1.0 \cdot 10^{-4}\text{m}^{-1}$.
Contamination of the windows in front of the transmitter and receiver influence the measured signal. This functioning of the sensor was checked periodically with a calibration reference standard of $\sigma_e = 0.0237\,\text{m}^{-1}$, which was mounted between the transmitter and receiver unit. If the latter σ_e value agreed with the measured value within the instrument uncertainty, the extinction coefficient was calibrated, otherwise the windows were cleaned. The periodically checks made during the measurement period are shown in Table 4.2.

4.3.2 Data processing of the visibility sensor

The ambient extinction coefficient measured by the visibility sensor includes the attenuating effects of both aerosol particles and air molecules. Yielding an ambient extinction coefficient not to be affected by the attenuation of light by air molecules, the extinction of the air has to be subtracted from the measured extinction. Using equations 2.8 and 2.11 the extinction coefficient of air at a wavelength of 880 nm is around $2.0 \cdot 10^{-6}\text{m}^{-1}$. This value does not

Table 4.2: *Measured σ_e during calibration with reference standard.*

day of year 2008	date 2008	measured σ_e [m^{-1}] (5 min average)	cleaning optical window
14.660	14.1. 15:50	0.0209	✓
22.415	22.1. 9:57	0.01514	✓
27.403	27.1. 9:40	0.02346	No
33.413	2.2. 9:55	0.02354	No
35.383	4.2. 9:11	0.02346	No
39.392	8.2. 9:25	0.02346	No

contribute significantly to typical atmospheric extinction of visible light at that wavelength and was therefore neglected.

As outlined in chapter 4.3.1, the calibration factor that converts the receiver signal of the visibility sensor into an extinction coefficient is a constant and is only valid for fog conditions with low visibility conditions. To use the measured extinction coefficient as a reference for optical closure studies at ambient conditions, the ratio of the receiver signal of the visibility sensor to the extinction coefficient must be constant during the campaign. Thus, it is necessary to show that a measurement of the angular scattering coefficient, under certain strict conditions, can be related to the ambient (atmospheric) extinction coefficient (Biral user manual). Therefore, the receiver signal of the visibility sensor and the extinction coefficient were simulated with the aerosol model (introduced in chapter 6). As it will be shown in Figure 6.3(c), both values show a linear dependency and are connected by a constant factor.

4.4 Scattering coefficient

4.4.1 Integrating nephelometer

An integrating nephelometer (Model 3563, Serial no. 1027, TSI Inc., St. Paul, USA) was used to measure a value that is close to the particulate scattering and hemispheric backscattering coefficient at three wavelengths ($\lambda = 450$, 550, and 700 nm). The setup and the function of the instrument are described in detail by Anderson *et al.* (1996) and Heintzenberg *et al.* (2006). The sample aerosol is drawn through an inlet via a blower or an external vacuum supply. During the campaign, the blower was removed and bypassed, and the integrating nephelometer was placed upstream of the Multi Angle Absorption Photometer (MAAP) (see Figure 4.1), which generally operates with an external vacuum pump. Automatic daily zero measurements with particle-free air were performed daily to correct online the scattering coefficient for changes in wall scattering artifacts due to contamination of the sensing volume.

Calibrations with particle-free air and carbon dioxide were carried out before and after the field campaign on January 16 and February 11, respectively. Table 4.3 summarizes the cal-

Table 4.3: *Calibration constants derived from calibration made on January 16 (red) and February 11 (green).*

	$\lambda = 450\,\mathrm{nm}$	$\lambda = 550\,\mathrm{nm}$	$\lambda = 700\,\mathrm{nm}$
K2	$4.347{\cdot}10^{-3}$ $4.334{\cdot}10^{-3}$	$4.228{\cdot}10^{-3}$ $4.260{\cdot}10^{-3}$	$4.194{\cdot}10^{-3}$ $4.189{\cdot}10^{-3}$
K4	$4.130{\cdot}10^{-1}$ $4.110{\cdot}10^{-1}$	$4.080{\cdot}10^{-1}$ $4.126{\cdot}10^{-1}$	$3.950{\cdot}10^{-1}$ $4.004{\cdot}10^{-1}$

ibration constants K2 and K4. The deviation of the calibration constants was smaller than 2%, and hence, no nephelometer drift was observed during the measurement period. Nevertheless, the K4 value, which describes the ratio of hemispheric backward to total scattered light, was lower than normal. The value should be about 0.5 for a symmetrical scatterer, such as a gas molecule. The deviation of the K4 values was investigated after the measurement campaign. The integrating nephelometer was disassembled and it was found that the backscatter shutter, which shadows the forward scattered light, was deformed such that it blocked some light in the backward direction. As a consequence, the data of hemispheric backscatter coefficient were unfortunately corrupted and thus excluded from the data set for further analysis.

The uncertainty of the integrating nephelometer was investigated recently in an intercomparison workshop. Heintzenberg *et al.* (2006) intercompared nine TSI nephelometer (model 3563) using submicrometer and supermicrometer test aerosols. For the submicrometer and the supermicrometer particles, the TSI nephelometer varied within an average value of 6% and 13%, respectively.

4.4.2 Data processing of the nephelometer

Due to the truncation error of the sensing volume and for the non-Lambertian illumination from the white light source, the scattering coefficient measured by the integrating nephelometer differs from the true scattering coefficient. Numerous research studies (e.g., Anderson and Ogren (1998); Heintzenberg *et al.* (2006); Bond *et al.* (2009); Müller *et al.* (2009a)) present correction factors for a non-Lambertian illumination. In this work, the corrections were not applied to the measured scattering coefficients, since the measured nephelometer values were used to verify the calculated nephelometer signal within a closure study at dry conditions (cf. chapter 5.3.1). For further considerations, the scattering coefficient measured by the integrating nephelometer is called nephelometer scattering coefficient.

4.5 Absorption coefficient

The particulate light absorption coefficient was determined with three types of absorption photometers, which are all based on the filter measurement technique. These are the Multi Angle Absorption Photometer (MAAP), the Particle Soot Absorption Photometer (PSAP), and the Spectral Optical Absorption Photometer (SOAP). In this investigation, the data

from the MAAP were not used. Therefore, only the PSAP and the SOAP instrument are introduced.

4.5.1 PSAP

The dry absorption coefficient at $\lambda = 522\,\text{nm}$ (Müller *et al.*, 2010) was determined with two PSAPs (Radiance Research, Seattle, USA). The first PSAP (PM_{10} PSAP) measured the absorption coefficient downstream the PM_{10} inlet, while the second PSAP (PM_1 PSAP) measured the particulate absorption coefficient downstream of an extra sharp cut cyclone (ESCC). Inside the PSAP, a LED illuminates a glass fibre filter (Pallflex E70 - 2075W) with accumulated particles on it and a blank filter simultaneously. With the Lambert-Beer law, the transmitted light by the deposited particles gives a direct measure of the particulate absorption coefficient. Bond *et al.* (1999) deliver a detailed description of the PSAP. The flow rates of the PSAPs were calibrated with an electronic bubble flow meter before and after the measurement period on January 15 and February 10, respectively. As illustrated in Figure 4.14, both calibrations differ within 1%.

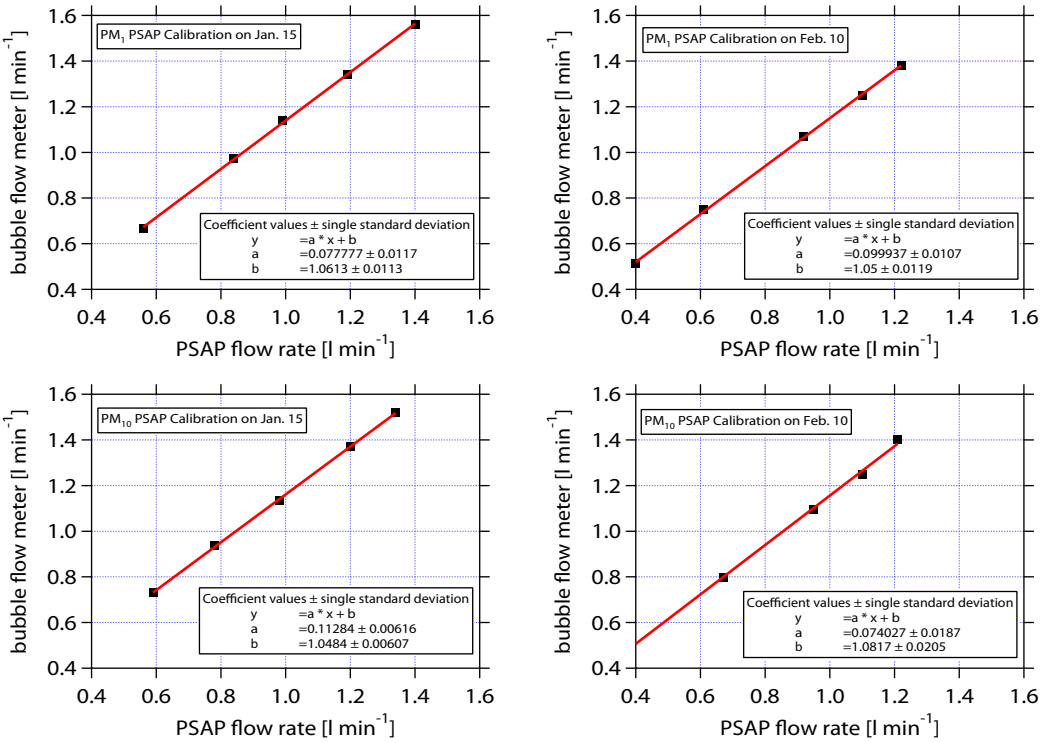

Figure 4.14: *Flow rate calibrations on January 15 and February 10 for PM_1 and PM_{10} PSAPs, respectively.*

The measurement uncertainty of both PSAPs was investigated in a laboratory experiment. For two days both PSAPs ran parallel and the average deviation of both PSAP signals was 6%, which corresponds to the device to device uncertainty given by Bond *et al.* (1999).
The cyclone upstream of the PM_1 PSAP originated from an electrical aerosol detector (Model 3070A, TSI Inc., St. Paul, USA) and is based on the work of Kenny and Gussman

(1997, 2000). The cyclone efficiency curve at a default volume flow rate of $Q = 2.5\,\mathrm{l\,min^{-1}}$ was determined with an APS during a laboratory experiment. Figure 4.15 shows a 50% penetration at $dp_a = 1.0\mu\mathrm{m}$. A sigmoidal (logistic) function (cf. Winklmayr *et al.* (1990))

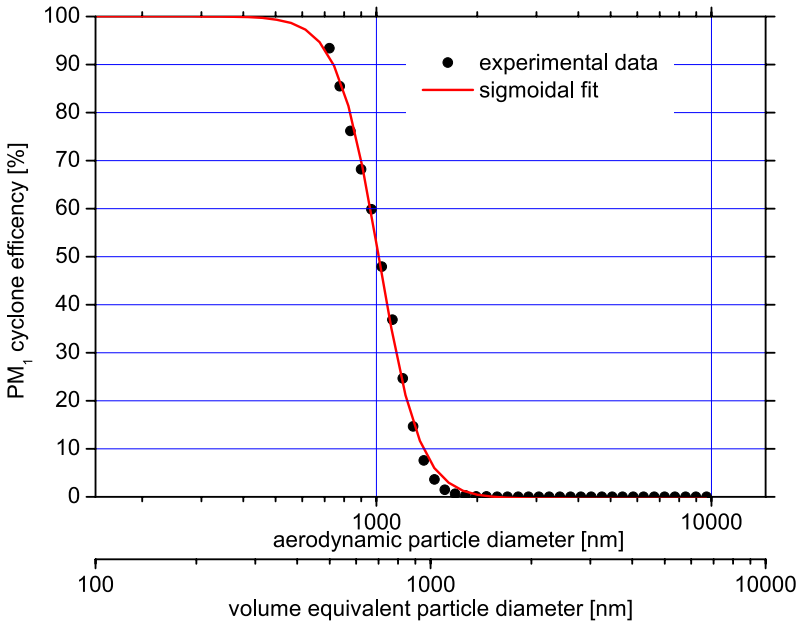

Figure 4.15: *Measured PM_1 cyclone efficiency at a flow rate of $2.5\,l\,min^{-1}$ as function of different particle diameters and sigmoidal fit represented by equation 4.16.*

was fitted to the experimental data:

$$f_{\mathrm{PM_1}}(dp_{ve}) = -0.0037 + \frac{1.0005 + 0.0037}{1 + (dp_{ve}/700.75)^{7.0556}}. \tag{4.16}$$

The PM_1 PSAP measured the particulate absorption coefficient at PM_1.

4.5.2 Data processing of the PSAP

Following the scheme described in Bond *et al.* (1999), the apparent particulate absorption coefficients derived by both PSAPs were corrected for a scattering artefact using nephelometer data, the deposition spot size of the filter, and the volume flow rate. Nevertheless, Andreae and Gelencsér (2006) point out that the cross sensitivities of the filter based absorption measurements to the size, single scattering albedo, and mixing state causes systematic errors of the absorption. Bond *et al.* (1999) proposed that the corrections cannot cover strongly scattering particles (high single scattering albedo) and are insufficient at high filter loadings. Therefore, the absorption coefficients were additionally corrected for filter loading and particle scattering effects by using a ray-tracing method reported by Müller *et al.* (2009b). This correction compensates for a loading-dependent sensitivity of the PSAP in cases of high single scattering albedo and was successfully applied to PSAP data of the SAMUM-1 field experiment. The loading effect for purely scattering particles was recently shown in Müller *et al.* (2010).

4.5.3 SOAP

The SOAP was designed to measure the absorption coefficient in a wavelength range from 300 - 950 nm. In contrast to the PSAP, the transmitted and the reflected light at 140° are detected for a blank and a particle laden filter. Key components of the SOAP are a deuterium-halogen light source, two (in the latest version) optical spectrometers with an optical resolution of 25 nm and a sensing head, which collects the particle on a filter, to illuminate the sample spot and to measure the transmittance and the reflectance. A detailed description of the device is delivered by Müller *et al.* (2009b) and in the latest version by Meusinger (2009). The measurement uncertainty of the SOAP caused by photon noise is estimated to 15% by Müller *et al.* (2009b) during the SAMUM-1 experiment.

4.5.4 Data processing of the SOAP

Basic data provided by SOAP are intensities in transmission and reflection over time and wavelength. In the end, absorption and scattering coefficients are wanted for output. Several steps are needed to get there. After applying some simple corrections and averaging procedures, optical depths[3] of transmission and reflection were calculated. They provide the basis for the constrained two stream method (CTS), where the optical depths of the particle and filter system were transformed to CTS-corrected optical depths (particle properties only). Hence, corrected optical depths were used to calculate particulate absorption and scattering coefficients.

4.6 Particle mass concentration and single particle analysis

4.6.1 $PM_{2.5}$ and PM_{10} filter sampler

Particle mass concentrations of $PM_{2.5}$ and PM_{10} equivalent were measured daily with filter samplers. The position of the filter samplers was on top of the measurement container in a height of about 4 m above ground as shown by an arrow in Figure 3.3. Both filter samplers consist of a double slit pre-impactor with a 50% penetration at $dp_a = 2.5\mu$m and $dp_a = 10\mu$m, respectively, and a backup filter for sampling. Further details of the design of the filter sampler are given in Kandler *et al.* (2009). The mass concentrations were determined by weighing the filter samples, the flow rate through the filter sampler (8 $m^3\,h^{-1}$) and the measurement duration of the filter. The weighing in terms of a microbalance was performed at a constant relative humidity of about 55% and thus, the mass concentrations were derived at the same RH. The uncertainty for the mass concentrations was specified to 10% (Kandler, 2010).

[3]The optical depth is a measure of the proportion of radiation absorbed or scattered along a path through a partially transparent medium

4.6.2 High volume sampler

Total suspended (TSP) particle mass concentrations were measured daily with a high volume sampler on a wind vane (same height as filter sampler) to achieve isoaxial sampling (Kandler *et al.*, 2009). The particles were drawn quasi-isokinetically into the high volume sampler and were deposited on a 70 mm filter. Details for this device are given in Kandler *et al.* (2009). The determination of the TSP mass concentrations was identical to the $PM_{2.5}$ and PM_{10} filter samples.

4.6.3 Raman spectroscopy

Inelastic or Raman scattering occurred during a scattering process, when the wavelength of the incident and the scattered light changes. A detailed description of the Raman-Effect is found e.g., in Haken and Wolf (1998). The energy difference between incident and scattered light is called Raman shift. In a Raman spectrum, the intensity of the Raman scattered light is plotted in dependence of the Raman shift. In the early 1970s, Tuinstra and Koenig (1970) found bands of activated graphitic carbon in the Raman spectrum. Rosen *et al.* (1978) identified the relationship of the amount of absorbing species and the graphitic soot content of the G-Band at the wavenumber $k = 1585\,\mathrm{cm}^{-1}$ in the Raman spectrum.
From the present measurements, the mass concentration of graphitic carbon was determined using Raman spectroscopy. Glass fibre filter probes sampled with the PM_1 PSAP were analyzed with a Bruker IFS 55 spectrometer including a FRA-106 Raman module in backscatter configuration. The monochromatic light source is a Nd: YAG[4] laser with a wavelength of 1064 nm. For each filter probe, the Raman spectrometer delivers a characteristic Raman spectrum, which depends of the amount of graphitic carbon on the substrate.
The calibration of the Raman spectrometer that converts the Raman intensity into a mass load in the unit of $\mu\mathrm{g\ cm}^{-2}$ was done by Mertes *et al.* (2004) using synthetic carbon black (Monarch 71, Cabot Corporation, Billerica, USA). Hence, the calibration is valid for the graphitic carbon content in this specific synthetic carbon black. Due to the similar structure of the Raman spectrum of the synthetic carbon black compared to atmospheric soot probes (Mertes *et al.*, 2004), the measured mass load is a soot mass load.
Finally, the mass concentration of soot in the unit of $\mu\mathrm{g\ m}^{-3}$ was derived from the soot mass load, the area of the filter deposited with particles ($2.04 \cdot 10^{-5}\mathrm{m}^2$), and the total air volume sucked through the filter.
The uncertainty in the soot mass concentration is about 10% (Mertes *et al.*, 2004) including the uncertainty of the Raman spectrometer, the systematic error from the calibration, uncertainties of the measured deposited area, and the total air volume.

[4] Neodym-dotierter Yttrium-Aluminium-Granat

4.6.4 Miniature cascade impactor

Aerosol sampling for single particle analysis was carried out with a miniature cascade impactor (MINI). Samples were taken up to twice each day for 5 - 180 seconds, depending on the awaited aerosol concentration. This novel device was developed by Kandler *et al.* (2007). For isoaxial sampling the MINI was mounted on a three-dimensional wind vane on top of the container as shown in Figure 3.3. In Figure 4.16 the impactor tube holds four individual stages, with orifice diameters ranging from 0.25 to 1.5 mm, which corresponds to cutoff sizes from 0.1μm to ~3μm. Particles smaller than ~0.8μm in diameter were collected

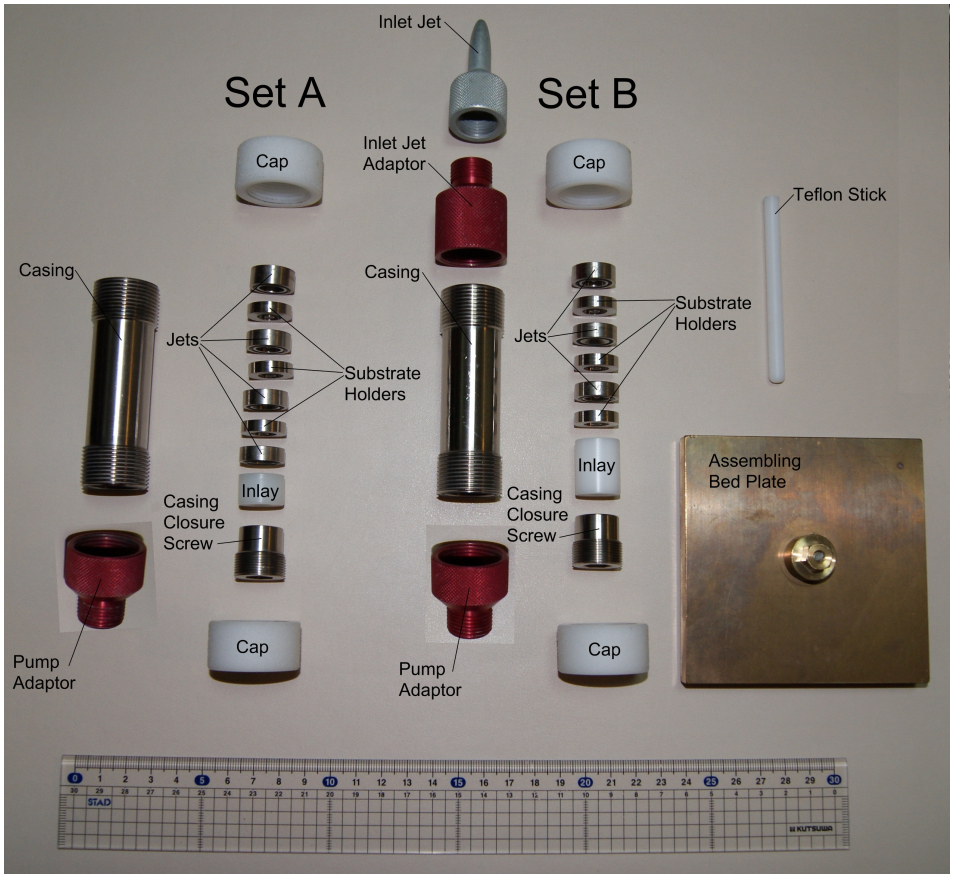

Figure 4.16: *Disassembled miniature cascade impactor. (photo from Kirsten Lieke)*

on transmission electron microscopy (TEM) grids, whereas larger particles were collected on an adhesive carbon substrate.

The samples were taken and analyzed by TU Darmstadt using scanning electron-microscopy of single particles. Analyzing all samples would take too long, therefore only some of them were analyzed. The analyzed sample dates for this work are: DOY 18.65, 19.76, 25.63, 28.39, 28.71, 35.63, 35.76, 36.58, 36.76, 37.56, 38.43, 39.43, and 40.42 LT. Based on the chemical composition derived from the X-ray count rates, particles were classified into 25 different mineralogical groups. Then, the particles were classified into logarithmically equidistant size classes according to their projected area diameter.

5 Aerosol characterization and closure studies at dry conditions

The primary goal of this section is to deliver parameters of an aerosol model (introduced in chapter 6), which describes the optical as well as the microphysical properties of the marine and Saharan dust aerosol at dry conditions. The second goal of this chapter is to characterize the aerosol measured at Cape Verde in terms of particle number size distribution, hygroscopic growth behavior and hygroscopic mixing state as well as particle shape and wavelength-dependent complex refractive index. To derive the imaginary part of the complex refractive index for mineral dust, the following steps are performed:
First, within a closure of optical properties such as scattering and absorption coefficients at dry conditions (chapter 5.3.1), the calculated optical properties are compared with measurements using refractive indices from literature. Second, with some knowledge from this closure (differences in the spectral behavior of the absorption coefficient), e.g., an optical equivalent imaginary part of mineral dust is retrieved (chapter 5.3.2). In contrast to the imaginary part of the refractive index, the optical equivalent imaginary part includes also the shape of the particle and optical properties can be calculated applying Mie theory. The optical equivalent imaginary part imaginary is compared with imaginary parts of pure Saharan dust.

5.1 Dry parameterized PNSD

Figure 5.1 shows a statistical analysis of the discrete dry PNSD for the entire period. For illustration, four lognormal size distributions (equation 4.4) were fitted to the median value. Two fine particle modes (blue solid lines) represent the typical bimodal submicrometer marine PNSD composed of an Aitken and an accumulation mode. In a review article about marine aerosols (Fitzgerald, 1991), the geometric mean diameters of the bimodal marine PNSD are reported in the range of $d_{gN} = 40$ - $60\,\mathrm{nm}$ and $d_{gN} = 180$ - $300\,\mathrm{nm}$, respectively. The fine fraction of the marine (background) aerosol, typically in the size range $dp_{ve} < 600\,\mathrm{nm}$ is explained primarily as non-sea-salt sulfate (NSS), formed by gas-to-particle conversion of the oxidation products of organosulfur gases (such as DMS[1]) emitted by the ocean (Fitzgerald, 1991). The double peak characteristic is caused through cloud processing of non-precipitating clouds (Hoppel *et al.*, 1990). In clouds, trace gases such as SO_2

[1] dimethyl sulfide

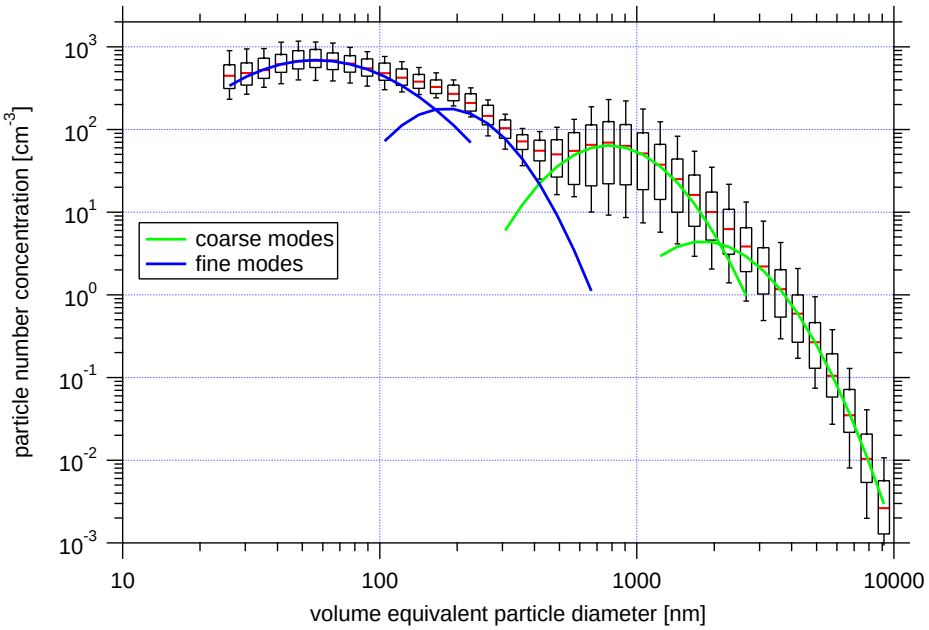

Figure 5.1: *Box plot of the dry particle number size distribution for the entire measurement period as well as fitted lognormal size distributions to the median value.*

are absorbed by cloud droplets and are converted to particulate matter such as sulfates (Fitzgerald, 1991). The aerosol particles remaining after the evaporation are larger than the original ones. The new particles are potential cloud condensation nuclei (CCN) on which the cloud droplets maybe formed (Fitzgerald, 1991).

The average mineralogical composition shown in Figure 5.2 revealed that a high portion of sulfate particles in the fine mode are ammonium sulfate, which is in accordance to former studies (Mészáros and Vissy, 1974; Gras and Ayers, 1983). Therefore, a dry particle density of $\rho_p = 1700\,\mathrm{kg\,m^{-3}}$ for the fine mode was estimated.

The coarse mode (green solid lines in Figure 5.1) represents the external mixture of sea-salt and mineral dust particles. Gras and Ayers (1983) pointed out that in the clean marine aerosol essentially all particles larger than $dp_{ve} = 600\,\mathrm{nm}$ consist of sea-salt. The process of production of sea-salt aerosol is due to agitation of the sea surface by the wind. The wind over the sea surface produces water drops which burst, producing both film and jet drops. As illustrated in Figure 5.2, components of mineral dust particles, such as silicates and quartz, occur nearly in the same size range as sea-salt particles, which mainly consist of sodium chloride and sodium sulfate.

During SAMUM-1, the geometric mean diameter of a mineral dust PNSD was 715 nm on average (Kaaden *et al.*, 2009), which agrees to the fitted (first) coarse mode geometric mean diameter shown in Figure 5.1. Hence, the first coarse mode can be directly attributed to sea-salt and mineral dust particles, while the second coarse mode is a virtual mode (no physical meaning) to achieve conservation, especially for the particle surface and volume concentration. It is assumed that the second (virtual) coarse mode has the same chemical composition as the first coarse mode.

The time series of the discrete dry PNSD was automatically fitted with a least square al-

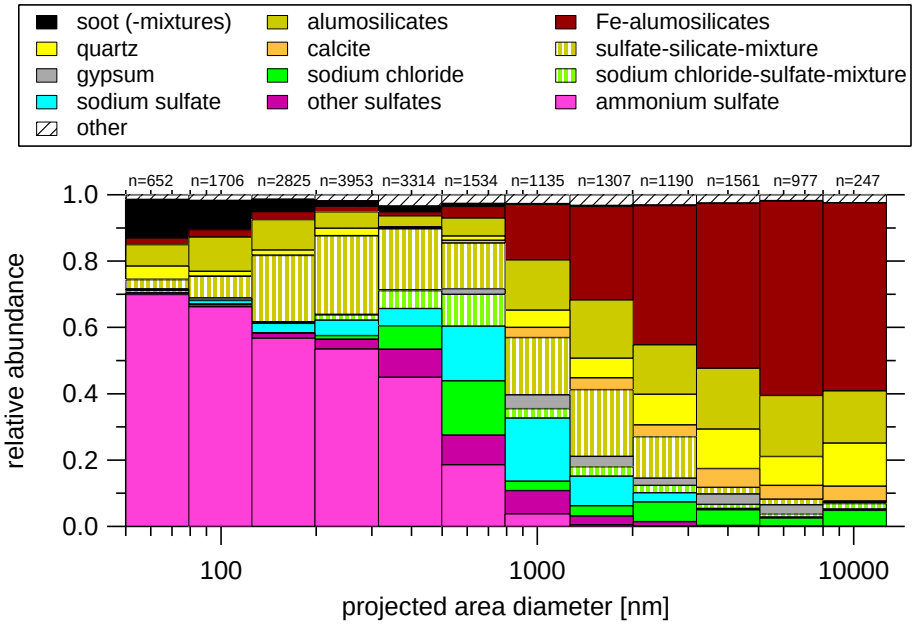

Figure 5.2: *Average mineralogical composition for 12 components. Components which have a relative abundance <1% are grouped into "other".*

gorithm (Birmili, 1998) yielding the fit parameters N, d_{gN}, and σ_g for each lognormal size distribution. From the parameterized PNSD, a discrete PNSD was recalculated and compared with the initial discrete PNSD. It was found, that the deviations in total number, surface and volume concentrations were always lower than 5%. Table 5.1 summarizes the arithmetic mean value and single standard deviation for the lognormal size distribution parameters. In general, within each particle mode, the variation of the total particle number

Table 5.1: *Arithmetic mean value and single standard deviation (std) of the total particle number concentration N, geometric mean diameter d_{gN}, and geometric standard deviation σ_g of the four fitted lognormal size distributions.*

mode #	mode name	$N \pm 1$ std	$d_{gN} \pm 1$ std	$\sigma_g \pm 1$ std
1	combined sea-salt & dust	3.9±5.4 cm^{-3}	1790±328 nm	1.54±0.07
2	combined sea-salt & dust	39.4±37 cm^{-3}	780±49 nm	1.52±0.05
3	accumulation	84±42.5 cm^{-3}	177±17.5 nm	1.5±0.07
4	Aitken	541±247 cm^{-3}	53±11 nm	1.9±0.11

concentration is larger than the variation of the geometric mean diameter and geometric standard deviation. The largest variations of the total particle number concentration show the coarse particle modes, followed by the accumulation and Aitken modes. Typical total particle number concentrations for the Aitken and accumulation particle modes over central regions of the Atlantic are 600 cm^{-3} on average (Junge and Jaenicke, 1971) and 50 - 100 cm^{-3} (O'Dowd *et al.*, 1997), respectively. These values agree with the values found in this study of 541±241 cm^{-3} for the Aitken mode and 84±42 cm^{-3} for the accumulation mode.

The large variation of N in the coarse mode is exemplified in the following: Some investigations (e.g., Fitzgerald (1991); O'Dowd and Smith (1993); O'Dowd *et al.* (1997)) found

a connection of the particle number concentration of the marine aerosol - in particular for the sea-salt aerosol - and the actual wind speed over the ocean. In our study, the sea-salt variation in the total number concentration is superimposed by the contribution of mineral dust particles in the coarse particle mode. Hence, the following section confirms that the variation of the amount of Saharan mineral dust particles is much larger than the variation of the sea-salt content in the coarse mode.

5.2 Hygroscopicity parameter κ and number fractions

Figure 5.3 shows a box plot of the κ parameters for the hygroscopic and hydrophobic particles for the entire measurement period. For the hygroscopic particles, the κ parameter is

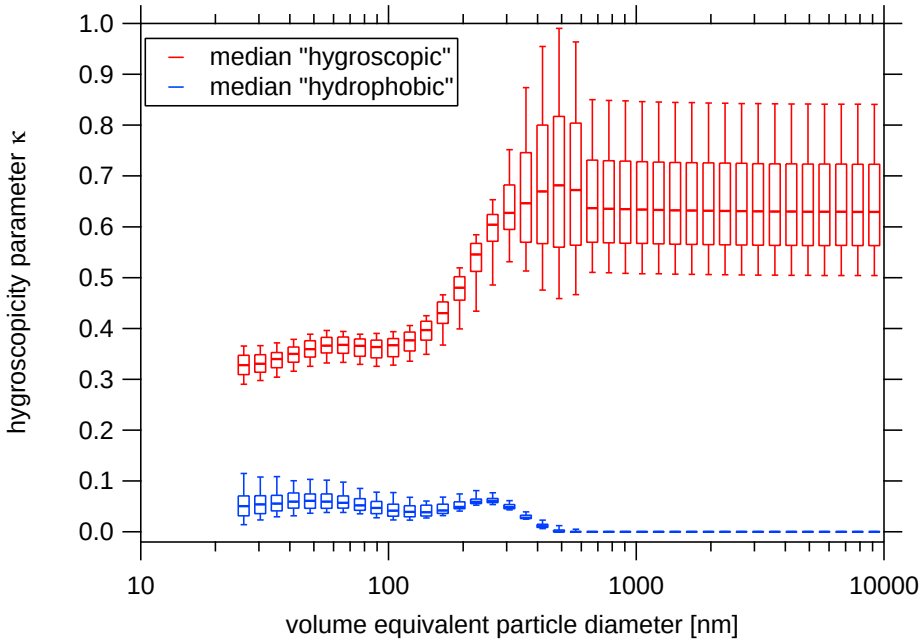

Figure 5.3: *Box plot of the hygroscopicity parameter κ for the entire measurement period.*

nearly constant in the size range $dp_{ve} < 100\,\text{nm}$ with a median around 0.35 and increases to $\kappa = 0.65$ in the subsequent size range from $100\,\text{nm} < dp_{ve} < 350\,\text{nm}$. In the adjacent size range, κ was set to a constant (cf. chapter 4.2.4). For the hydrophobic particles, κ varies between 0 and 0.1 in the size range up to $dp_{ve} < 250\,\text{nm}$. The small hump around 250 nm is possibly caused by a broadening of the hygroscopic particle mode to smaller hygroscopic growth factors. Because of the separation of $GF < 1.2$ to hydrophobic particles, the mean hygroscopic growth factor of the hydrophobic mode is therefore enhanced. For larger particles $dp_{ve} > 250\,\text{nm}$, κ decreases towards 0 and remains constant (cf. chapter 4.2.4). The variation within κ is largest for the hygroscopic particles in the size range $dp_{ve} > 250\,\text{nm}$. The size dependency of κ can be explained by hygroscopic materials from the mineralogical composition. From the mineralogical composition (Figure 5.2), it is obvious that different species of hygroscopic materials are present: sodium chloride, sodium chloride-sulfate-mixtures, sodium sulfate, ammonium sulfate, and other undetermined and mixed

sulfates. Averaged, size segregated fractions of the three main inorganic salts (sodium chloride, sodium sulfate, and ammonium sulfate) are shown in Figure 5.4. Note that Figure 5.3 and Figure 5.4 are based on different particle diameter definitions. It is seen from

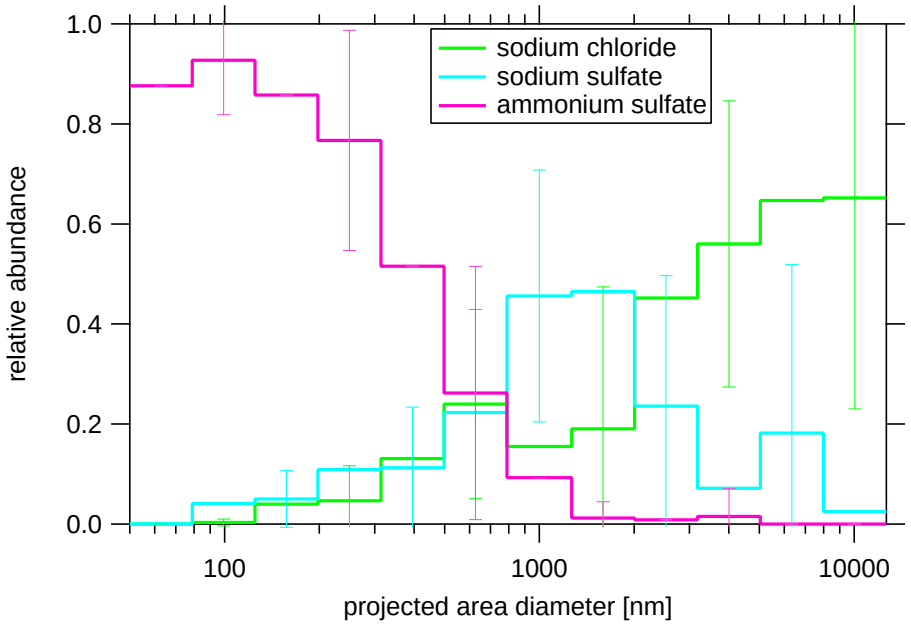

Figure 5.4: *Average fractions of sodium chloride, sodium sulfate, and ammonium sulfate from the mineralogical composition. The error bars (± single standard deviation) represent the variability for each fraction.*

Figure 5.4 that in the size range $dp < 100\,\text{nm}$, ammonium sulfate is the predominant hygroscopic component. In Petters and Kreidenweis (2007), κ parameters were derived from hygroscopic growth factors and CCN measurements for pure inorganic salts. The non-ideal growth behavior of hygroscopic substances near 100% RH causes the differences of CCN and hygroscopic growth factor derived κ values. For comparison issues, the hygroscopic growth factor derived κ values were chosen, since the κ values in this investigation was also derived from measured hygroscopic growth factors.

The measured κ value in the size range $dp_{ve} < 100\,\text{nm}$ is on the lower end of the reported values for pure ammonium sulfate particles that ranges from 0.33 to 0.72. A possible reason is the internal mixture with one or more hydrophobic substances and organic material, which can be less hygroscopic or hydrophobic. This assumption was supported by Kandler *et al.* (2011), who found ammonium sulfate particles internally mixed with soot, as well as hints of a possibly organic coating.

In the size range from $100\,\text{nm} < dp_{ve} < 300\,\text{nm}$, the increase of the hygroscopicity parameter κ with particle size is caused by the large fraction of sulfate within the particle, which was produced through cloud processing. The subsequent increase of the hygroscopicity parameter κ with particle size correlates with the increasing fractions of more hygroscopic materials, e.g., sodium chloride and sodium sulfate. The reported κ values for sodium chloride and sodium sulfate are 0.91 to 1.33 and 0.68, respectively. Again, the measured values are on the lower scale of the literature values. Nevertheless, Niedermeier *et al.* (2008) reported slightly

lower hygroscopic growth of sea-salt particles compared to pure sodium chloride particles. Furthermore, organic compounds in the uppermost thin layers of the sea water reduce the hygroscopic growth compared to pure sodium chloride. The larger variation of κ in the size range $dp_{ve} > 250\,\text{nm}$ is caused by the variability, represented by the standard deviation of the sodium sulfate and sodium chloride fraction in Figure 5.4.

Figure 5.5 illustrates the mean number fraction of hydrophobic particles. The difference

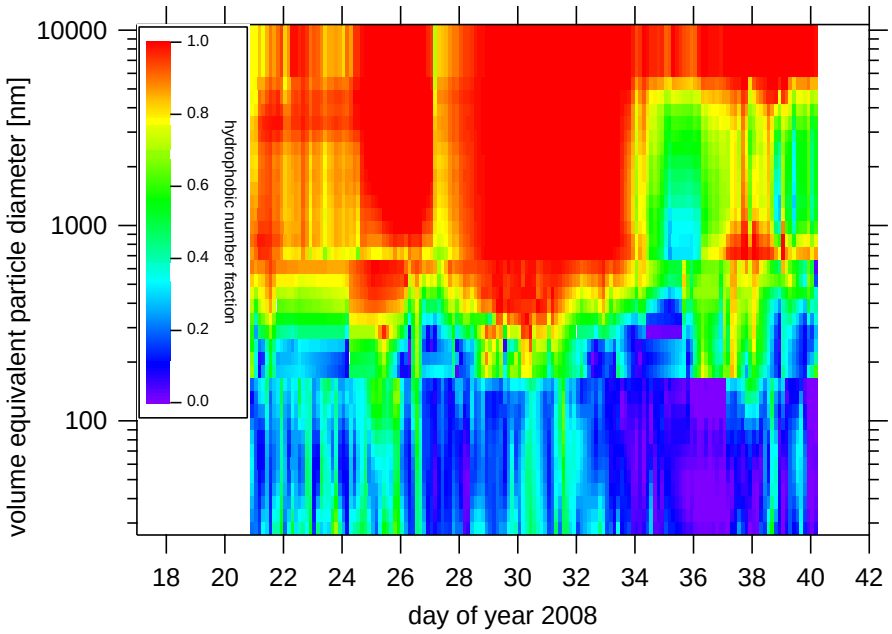

Figure 5.5: *Image plot of the mean hydrophobic number fraction for the entire measurement period.*

to unity equals the mean number fraction of hygroscopic particles. In general, the mean hydrophobic number fraction is larger in the coarse mode than in the fine particle mode. The highest (reddish) values occur for the hydrophobic mineral dust particles in the coarse particle mode. For this mode, the mean number fraction of mineral dust is still variable, with maxima close to 100%, between DOY 24.5 - 26.5 LT and DOY 28 - 34 LT. The lowest values with minima of ∼30% occur in the last period from DOY 34 LT. From Figure 5.5, the influence of dust particles reaches down to $dp_{ve} = 300\,\text{nm}$, which agrees with the smallest observed dust particles during SAMUM-1 (Kaaden *et al.*, 2009). Figure 5.2 reveals that soot and probably some silicate particles are the main hydrophobic component in the fine particle mode. Assuming that soot particles were completely externally mixed, the hydrophobic mass concentration derived from the hydrophobic number fraction in the fine mode and the mass concentration of soot, derived from Raman spectroscopy, would be positively correlated. However, this is not the case. Cheng *et al.* (2006) for instance pointed out that soot from long range transport is more internally mixed. Kandler *et al.* (2011) found some ammonium sulfate particles internally mixed with soot, as well as sulfate particles without soot and pure soot particles externally mixed. Moreover, Massling *et al.* (2007) argued that the hydrophobic particle fraction in the fine mode can be attributed to freshly emitted externally mixed soot particles. Hence, from the argumentation above it is

concluded that soot particles at Cape Verde were internally as well as externally mixed and the temporal variation of the hydrophobic number fraction in the fine particle mode was caused by changes in the mixing ratio of externally and internally mixed soot particles.

5.3 Wavelength-dependent complex refractive index

To compare calculated dry scattering and absorption coefficients with the measurements, literature values for the complex refractive index were used. The complex refractive index is taken from the OPAC database (Hess *et al.*, 1998), which is based in the original version on D'Almeida *et al.* (1991). To each lognormal size distribution (fine, coarse mode), and state of mixing in terms of hygroscopicity (hygroscopic, hydrophobic), a wavelength-dependent complex refractive index was addressed (Table 5.2). For the coarse mode, the complex

Table 5.2: *Corresponding complex refractive indices for the different particle modes and hygroscopic mixing state.*

mode name	coarse (hydrophobic)	coarse (hygroscopic)	fine (hydrophobic)	fine (hygroscopic)
name of aerosol component (Hess *et al.*, 1998)	mineral (transported)	sea-salt (0% RH)	92% water insoluble, 8% soot	92% water soluble (0% RH), 8% soot
dry particle density [kg m^{-3}]	2700	2170	1700	1700
imaginary part n				
$\lambda = 300$ nm	1.53-2.5·10^{-2}i	1.51-2.00·10^{-6}i	1.55-4.50·10^{-2}i	1.55-4.50·10^{-2}i
$\lambda = 350$ nm	1.53-1.7·10^{-2}i	1.51-3.24·10^{-7}i	1.55-4.46·10^{-2}i	1.55-4.18·10^{-2}i
$\lambda = 400$ nm	1.53-1.3·10^{-2}i	1.50-3.00·10^{-8}i	1.55-4.42·10^{-2}i	1.55-4.14·10^{-2}i
$\lambda = 450$ nm	1.53-8.5·10^{-3}i	1.50-2.43·10^{-8}i	1.55-4.38·10^{-2}i	1.55-4.10·10^{-2}i
$\lambda = 500$ nm	1.53-7.8·10^{-3}i	1.50-1.55·10^{-8}i	1.55-4.34·10^{-2}i	1.55-4.06·10^{-2}i
$\lambda = 550$ nm	1.53-5.5·10^{-3}i	1.50-1.00·10^{-8}i	1.55-4.26·10^{-2}i	1.55-4.07·10^{-2}i
$\lambda = 600$ nm	1.53-4.5·10^{-3}i	1.49-1.60·10^{-8}i	1.55-4.22·10^{-2}i	1.55-4.03·10^{-2}i
$\lambda = 650$ nm	1.53-4.5·10^{-2}i	1.49-4.24·10^{-8}i	1.55-4.22·10^{-2}i	1.55-4.12·10^{-2}i
$\lambda = 700$ nm	1.53-4.0·10^{-3}i	1.49-2.00·10^{-7}i	1.55-4.18·10^{-2}i	1.55-4.08·10^{-2}i
$\lambda = 750$ nm	1.53-4.0·10^{-3}i	1.49-1.08·10^{-6}i	1.55-4.18·10^{-2}i	1.55-4.22·10^{-2}i
$\lambda = 800$ nm	1.53-4.0·10^{-3}i	1.48-1.95·10^{-6}i	1.54-4.18·10^{-2}i	1.54-4.36·10^{-2}i
$\lambda = 900$ nm	1.53-4.0·10^{-3}i	1.48-4.24·10^{-5}i	1.54-4.22·10^{-2}i	1.54-4.68·10^{-2}i

refractive index for "sea-salt (0% RH)" was assigned to the hygroscopic particles, while "mineral transported" (is the same as "mineral" in Hess *et al.* (1998)) was assigned to the hydrophobic particles. The complex refractive index for the fine mode was calculated by using an internal mixture of "soot" and "insoluble" for the hydrophobic particles, and "soot" and "water soluble (0% RH)" for the hygroscopic particles. The average soot fraction in the fine particle modes is 7.7±3.1 vol%, and was determined as the ratio of soot mass concentration to total mass concentration in the fine particle modes. To calculate the mixed refractive indices for the hydrophobic and hygroscopic particles in the fine particle modes,

the Maxwell-Garnet relation (Maxwell-Garnett, 1904) was used, which is a two component mixing rule for refractive index.

5.3.1 Closure of optical properties at dry conditions

For an intercomparison of measured and calculated nephelometer scattering coefficients, Mie calculations were performed. For the Mie calculations, homogeneous spherical particles were assumed. The nephelometer response was calculated using equations 2.12 and 2.13, and $\sin(\theta)$ in equation 2.13 was replaced by the angular illumination function $I(\theta)$. The angular illumination function for the present TSI nephelometer is taken from Müller *et al.* (2009a), which confirms former measurements made by Anderson *et al.* (1996). Müller *et al.* (2009a) show in their Figure 2 that the angular illumination function obviously deviates from an ideal nephelometer, with $I(\theta) = \sin(\theta)$.
Figures 5.6(a) and (b) show the results of the calculation as a time series and scatter plot, respectively. In general, there is a good correlation between the calculated and measured

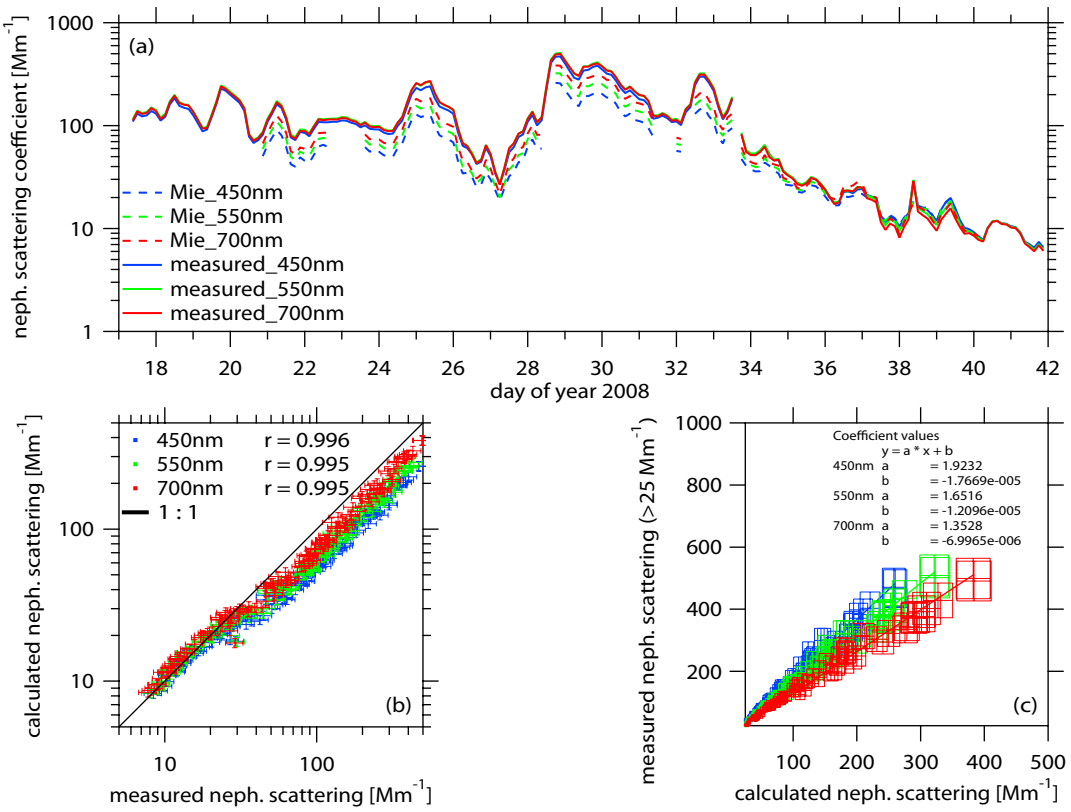

Figure 5.6: *(a) Time series of Mie calculated and measured nephelometer scattering coefficients at $\lambda = 450$, 550, and 700 nm. (b) Scatter plot of Mie calculated versus measured nephelometer scattering coefficients at $\lambda = 450$, 550, and 700 nm. (c) Scatter plot and linear fits of measured nephelometer scattering >25Mm^{-1} versus calculated nephelometer scattering. The error for the measured values are given by the nephelometer uncertainties, while the error for the calculated values is 7% and taken from Wex* et al. *(2002).*

values. The "Pearson's correlation" coefficient (r) is 0.99 for the three wavelengths $\lambda = 450$,

550, and 700 nm. Moreover, for scattering coefficients $\sigma_s^{\text{neph}} < 25\,\text{Mm}^{-1}$ calculated and measured values agree within the range of uncertainty. For larger scattering coefficients $\sigma_s^{\text{neph}} > 25\,\text{Mm}^{-1}$ the measured values are larger than the calculated values. Figure 5.6(c) shows a scatter plot of measured and calculated scattering coefficients with coefficients larger $25\,\text{Mm}^{-1}$. Linear fits applied to the data show wavelength-dependent slopes, which are 1.92±0.02 for the blue, 1.65±0.02 for the green, and 1.35±0.02 for the red wavelength, respectively. To interpret this behavior, the dry dust volume fraction was plotted against the measured scattering coefficient σ_s^{neph} in Figure 5.7, and the ratio of measured to calculated scattering was indicated through color coding. The dry dust volume fraction vf_{dust} is the ratio of the (hydrophobic) mineral dust volume concentration in the coarse mode to the total volume concentration and defined as

$$vf_{dust} = \frac{V_{hyd}(\text{coarse mode})}{V(\text{fine+coarse mode})} = \frac{\sum \frac{dN}{d\log dp}(\text{coarse mode}) \cdot nf_{hyd} \cdot dp_{ve}^3}{\sum \frac{dN}{d\log dp}(\text{fine+coarse mode}) \cdot dp_{ve}^3}. \tag{5.1}$$

As shown in Figure 5.7, σ_s^{neph} increases with increasing vf_{dust} in most of the cases. The

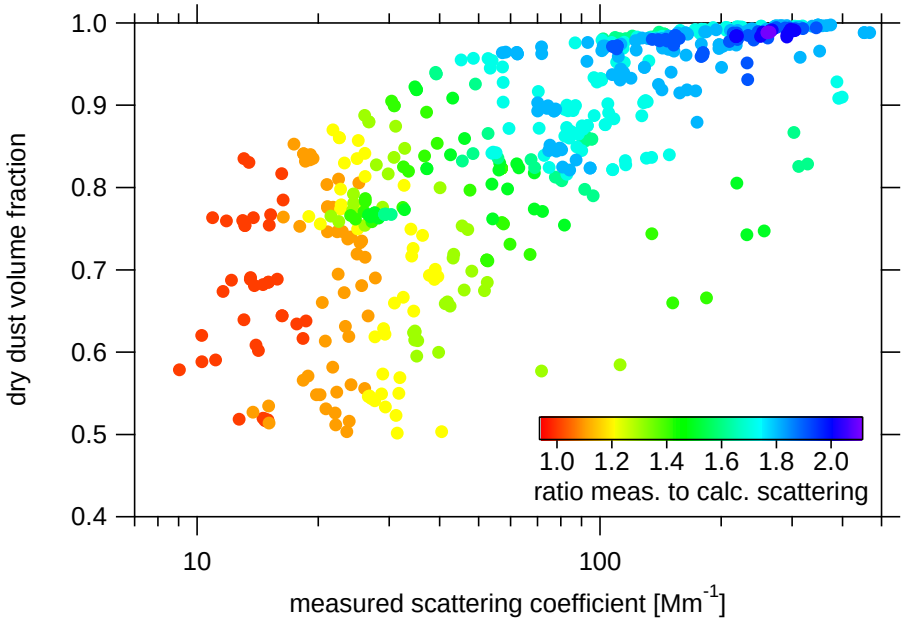

Figure 5.7: *Relationship between measured scattering coefficient and dry dust volume fraction. The data are sorted by the ratio of measured to calculated scattering at $\lambda = 450\,nm$.*

ratio of measured to calculated scattering increases with both σ_s^{neph} and vf_{dust}. Only for $\sigma_s^{\text{neph}} < 25\,\text{Mm}^{-1}$, the ratio of measured to calculated scattering is independent of vf_{dust}. The deviations of measured and calculated scattering coefficients can be explained by effects of non-spherical mineral dust particles. In this case, the assumption of spherical particles for mineral dust particles underestimates the real scattering coefficient. The magnitude of these deviations was investigated in a laboratory experiment and by numerical calculations of certain non-spherical shaped particles in chapter 5.4. To mention in advance, only the laboratory experiment can reproduce the observed differences between measured and Mie

calculated scattering coefficients. For this case, a wavelength-dependent non-sphericity factor for the scattering coefficient of mineral dust is introduced, which is the slope of the linear regression lines in Figure 5.6(c). Figure 5.8 illustrates the scattering non-sphericity factor of mineral dust for the three nephelometer wavelengths. A power function given in Figure 5.8 reproduces the wavelength dependency of the non-sphericity factor very well.

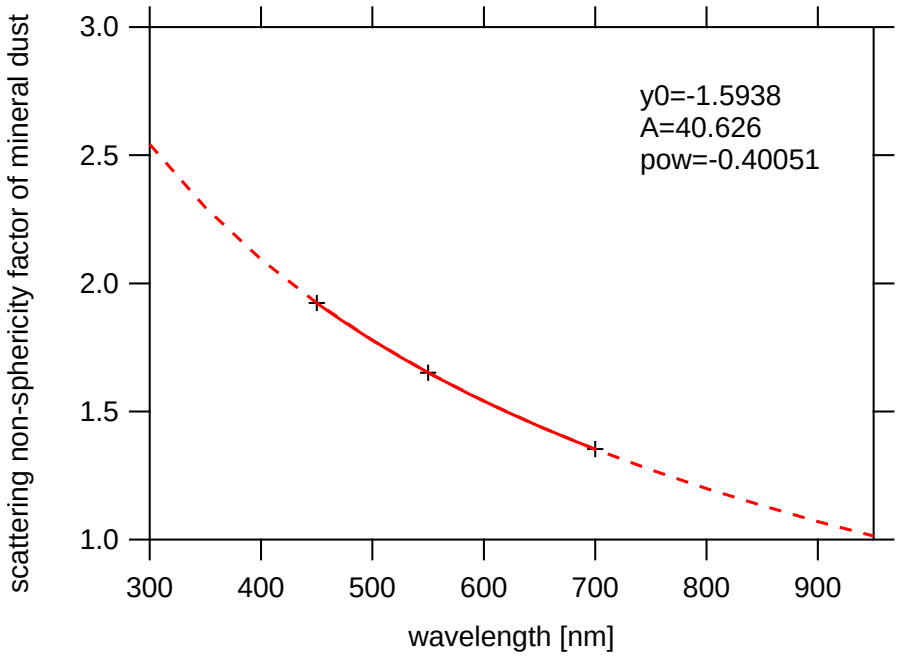

Figure 5.8: *Average non-sphericity factor for the nephelometer scattering coefficient (black crosses), and fitted power function* $y = y_0 + A \cdot \lambda^{pow}$ *(red solid line). Extrapolated power function in the wavelength range from* $\lambda = 300$ *-* $950\,nm$ *(red dashed line). The parameters of the power function are added.*

In order to calculate aerosol optical properties at the dry state and at a certain relative humidity in the wavelength range between $\lambda = 300$ - $950\,nm$, the power function was used to extrapolate the non-sphericity factors in the desired wavelength range.

Besides the scattering coefficient, closure studies were performed for absorption coefficients, measured by the PM_1 PSAP, PM_{10} PSAP, and SOAP. To calculate the PM_1 PSAP response, using equation 2.11, the fitted sigmoidal function (equation 4.16) of the PM_1 penetration curve shown in Figure 4.15 was considered. In contrast to the SOAP, both PSAPs were not measuring directly behind the aerosol inlet. Therefore, aspiration particle losses due to a tee connector and the reduction of the flow rate (from $10.5\,l\,min^{-1}$ to $3.5\,l\,min^{-1}$; see Figure 4.1), impaction in bends ($1 \times 90°$, $1 \times 45°$), and sedimentation in horizontal lines ($40\,cm$ in sum) were considered in the PSAP calculations. The formulas used for calculating the particle losses in the sampling lines are summarized in chapter 6.

Time series and corresponding scatter plots of measured and calculated absorption coefficients of the PM_1 and PM_{10} PSAPs are shown in Figure 5.9. Generally speaking, with the simple classification of the absorbing species soot and mineral dust into fine and coarse mode, the calculations reproduce the measured values. For a more quantitative discussion,

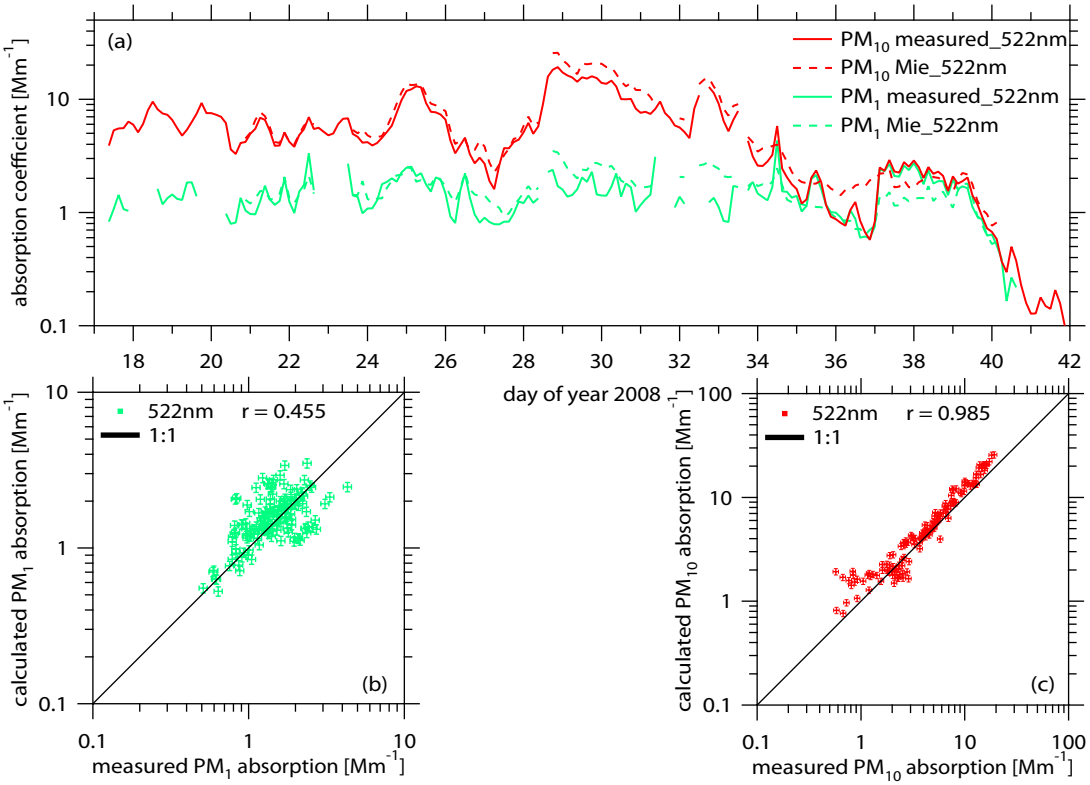

Figure 5.9: *(a) Time series of Mie calculated and measured absorption coefficients by PM_1 and PM_{10} PSAPs at $\lambda = 522\,nm$. (b) Scatter plot of calculated and measured absorption of PM_1 PSAP. (c) Scatter plot of calculated and measured absorption of PM_{10} PSAP.*

the PM_{10} PSAP calculations correlate much better ($r = 0.985$) with the measurements than the PM_1 PSAP calculations ($r = 0.455$). The weaker correlation is caused by the assumption of a constant imaginary part of the complex refractive index of the fine mode. In chapter 5.3 it was found that the soot fraction in the fine particle mode derived from Raman spectroscopy is however variable (7.7 ± 3.1 vol%). It is reasonable that the variation during the measurement period (represented by the single standard deviation) caused a variable imaginary part of the complex refractive index of the fine mode.

Figure 5.10 shows time series and corresponding scatter plots of measured and calculated absorption coefficients of the SOAP at $\lambda = 400$, 550, 700, and 850 nm.

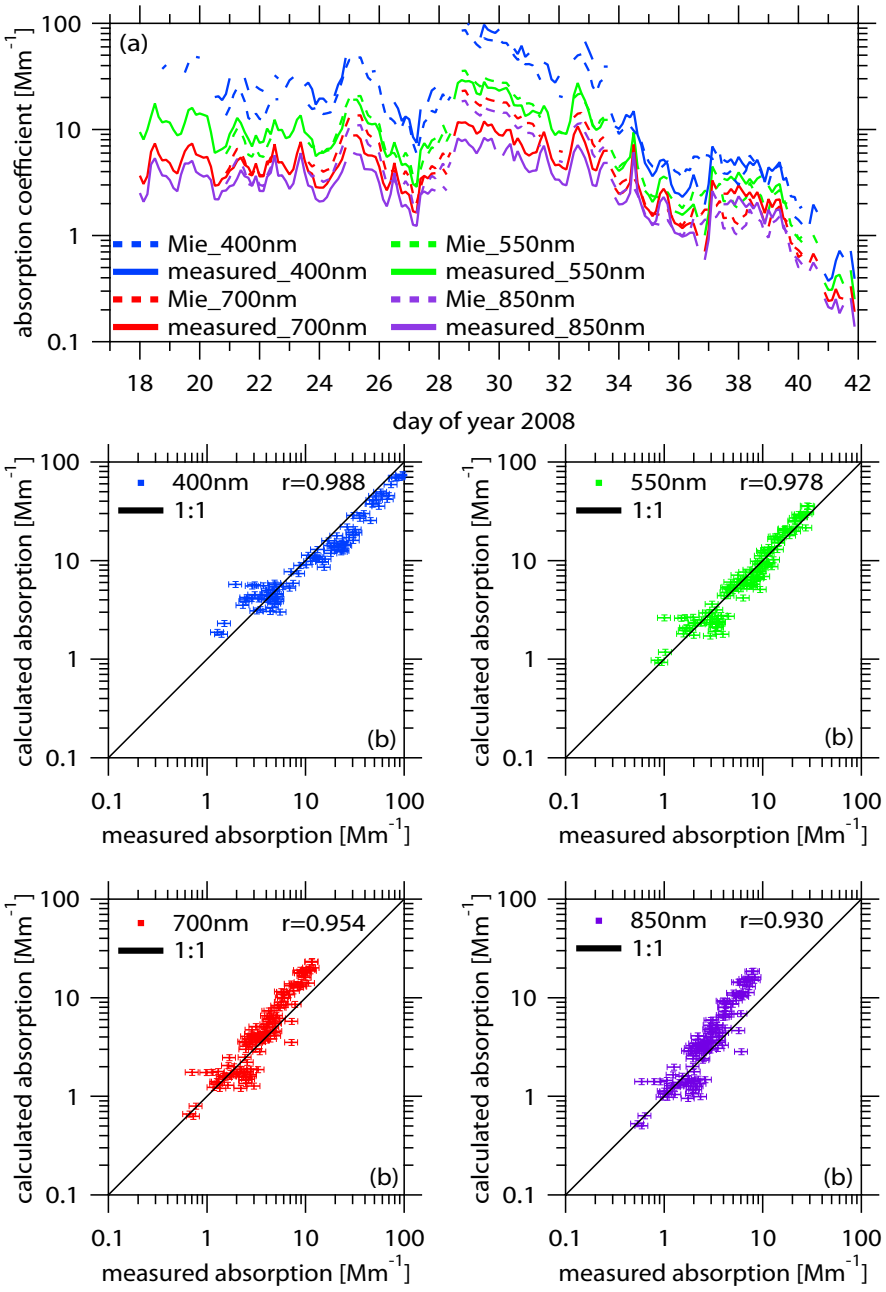

Figure 5.10: *(a) Time series of Mie calculated and measured absorption coefficients by the SOAP at $\lambda = 400$, 550, 700, and 850 nm. (b) Scatter plots of calculated and measured absorption at the four wavelengths.*

In general, the calculations reproduce the measured values. However, the correlation is highest at $\lambda = 400\,\text{nm}$ ($r = 0.988$) and lowest at $\lambda = 850\,\text{nm}$ ($r = 0.930$). The "weaker" correlation for the larger wavelengths can be explained again by a variable imaginary part of the complex refractive index of the fine mode as follows: As shown in Table 5.2 for larger wavelengths in the visible spectral range, the fine mode imaginary part of the complex refractive index is about one magnitude higher than for the coarse mode. In contrast to the smaller wavelengths, the absorption for the larger wavelengths is therefore more dominated by particles from the fine particle modes. Particles from the coarse particle modes with lower imaginary parts for larger wavelengths have a lower contribution to the absorption. Nevertheless, Figure 5.10(b) shows that for larger absorption coefficients at $\lambda = 400$, 700, and 850 nm, the calculated and measured values deviate from the 1:1 line. For $\lambda = 400\,\text{nm}$ the calculations underestimate the measurements, while for $\lambda = 700\,\text{nm}$ and $\lambda = 850\,\text{nm}$ the calculations overestimate the measurements systematically. Illustrated by time series in Figure 5.10(a), differences between calculations and measurements are higher in dust dominated periods (DOY 24.5 - 26.5 LT and DOY 28 - 34 LT) than in the low dust period (from DOY 34 LT on). The reason for this result could be a slightly different spectral behavior of the calculated absorption coefficient, and hence the imaginary part of mineral dust. Therefore, the next section describes the retrieval of an optical equivalent imaginary part of the refractive index for mineral dust.

5.3.2 Soot mass closure at dry conditions and retrieval of an optical equivalent imaginary part of mineral dust

As mentioned in the last section, the goal of this section is to retrieve an optical equivalent imaginary part of the refractive index for mineral dust, based on the measured absorption coefficients and particle number size distributions. One possibility would be, to calculate the fine mode absorption with a constant imaginary part as done in chapter 5.3.1 and to vary the dust imaginary part until calculated absorption fits the measured absorption. The disadvantage of this approach is that inaccuracies in determining the fine mode absorption lead to inaccuracies in determining the wavelength-dependent imaginary part of the refractive index of mineral dust. The following approach is more accurate and starts with the absorption coefficients for the PM_1 PSAP and PM_{10} PSAP:

$$\sigma_a^{\text{PM}_1\ \text{PSAP}} = vf_{dust,\text{PM}_1} \cdot \sigma_{a,dust} + \sigma_{a,soot} \tag{5.2}$$

$$\sigma_a^{\text{PM}_{10}\ \text{PSAP}} = \sigma_{a,dust} + \sigma_{a,soot}, \tag{5.3}$$

where $\sigma_{a,dust}$ and $\sigma_{a,soot}$ are the absorption coefficients of dust and soot, respectively. vf_{dust,PM_1} is the time-dependent fraction of mineral dust within PM_1, and is illustrated in Figure 5.11 for clarification.

vf_{dust,PM_1} was calculated analogously to equation 5.1 and incorporates the sampling efficiency to the PSAP, and the PM_1 penetration curve (equation 4.16).

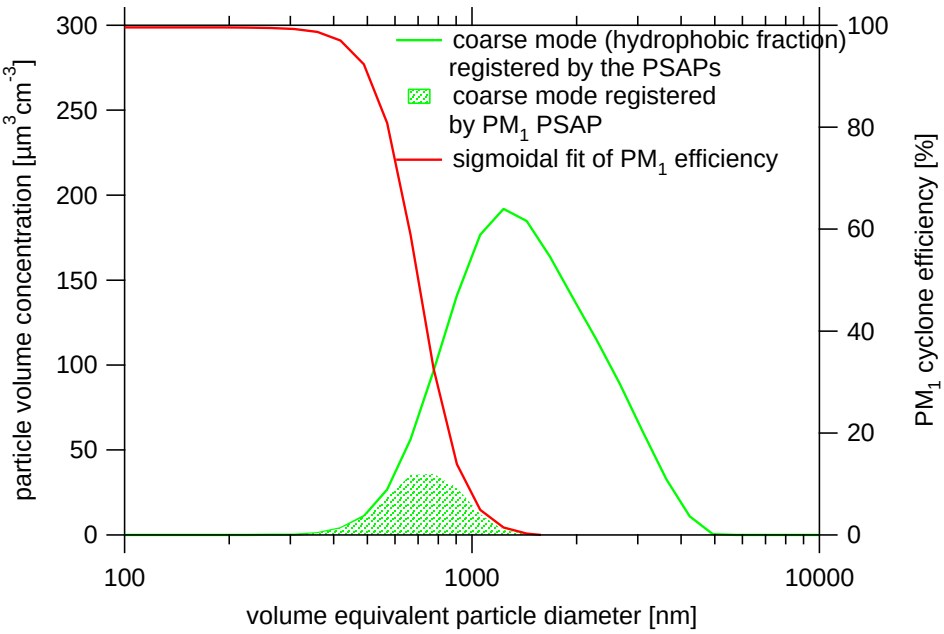

Figure 5.11: *Illustration of the dust volume fraction within PM_1 as a shaded area. The shaded area is enclosed by the sigmoidal fit of the PM_1 penetration curve (red solid line) and the fitted hydrophobic (mineral dust) fraction of the coarse mode (green solid line).*

Subsequently, both equations were rearranged yielding a formula for the absorption coefficient of soot:

$$\sigma_{a,soot} = \frac{\sigma_a^{\mathrm{PM_1\ PSAP}} - vf_{dust,\mathrm{PM_1}} \cdot \sigma_a^{\mathrm{PM_{10}\ PSAP}}}{1 - vf_{dust,\mathrm{PM_1}}}. \tag{5.4}$$

For validation, the retrieved absorption coefficient of soot was averaged within the time interval of the measured soot mass concentration from the Raman spectrometer. Figure 5.12 shows the result of the soot closure as a scatter plot. The mass absorption cross section (MAC) converts the absorption coefficient into a mass concentration and vice versa. Bond and Bergstrom (2006) and references therein report MACs of soot ranging from 3 - 16 $\mathrm{m^2 g^{-1}}$ at $\lambda = 550\,\mathrm{nm}$ including laboratory aerosol, diesel engines, and carbon black. However, values given in 16 of 21 references lie between 6.3 - 8.6 $\mathrm{m^2 g^{-1}}$. The wavelength for the reported MAC is close to the PSAP wavelength of $\lambda = 522\,\mathrm{nm}$. The lowermost and uppermost reported values are represented in Figure 5.12 as a straight line with a slope of 3 $\mathrm{m^2 g^{-1}}$ and 16 $\mathrm{m^2 g^{-1}}$, respectively. Regarding the large uncertainty (∼30%) of the method, the data points lie within the boundaries and therefore the soot mass closure was successful. Finally, the spectral absorption coefficient of soot was calculated using an Ångström-absorption-exponent of 1 (Bergstrom *et al.*, 2002; Kirchstetter *et al.*, 2004). The spectral absorption coefficient of dust was determined using the measured absorption coefficient by the SOAP σ_a^{SOAP}:

$$\sigma_{a,dust}(\lambda) = \sigma_a^{\mathrm{SOAP}}(\lambda) - \sigma_{a,soot}(\lambda). \tag{5.5}$$

Applying Mie calculations, an optical equivalent imaginary part of the refractive index of mineral dust was retrieved using the secant method. The secant method is based on the

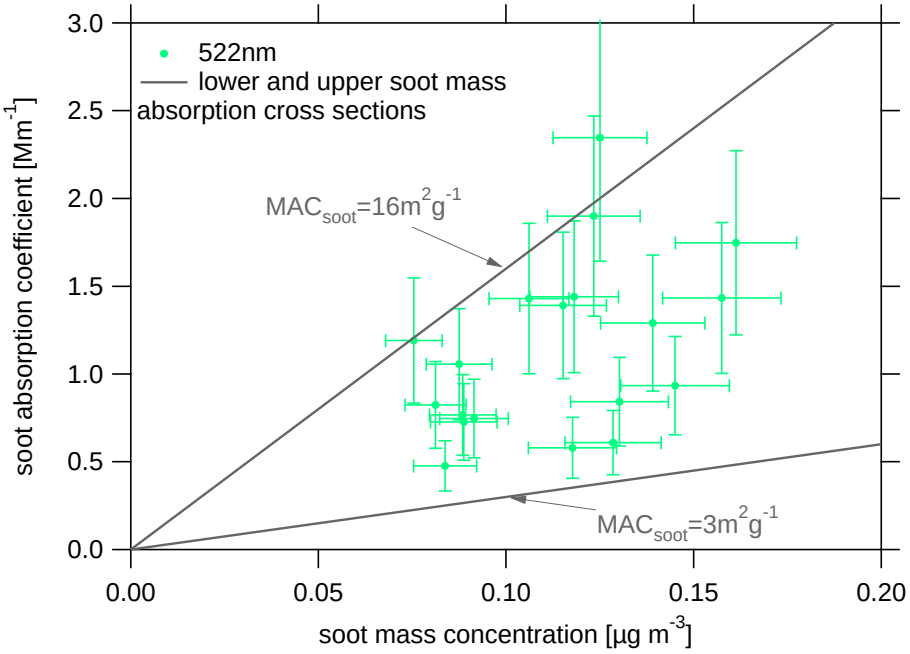

Figure 5.12: *Scatter plot of retrieved soot absorption versus measured soot mass concentration. The error for the soot absorption is about 30% on average and was calculated using error propagation.*

Newton-Raphson method, where the derivative of the function is replaced by the differential quotient. During the iteration, only the imaginary part was varied, while the real part of the complex refractive index was set constant (1.53, cf. Table 5.2). The iteration was repeated until Mie calculated ($\sigma^{\mathrm{Mie}}_{a,dust}$) and measured absorption coefficients of dust fit within a small residual $\epsilon = \left(\frac{\sigma^{\mathrm{Mie}}_{a,dust} - \sigma_{a,dust}}{\sigma_{a,dust}}\right)^2 < 1.0 \cdot 10^{-6}$ (cf. Cheng *et al.* (2006)). In Figure 5.13, a box plot show the optical equivalent imaginary part of mineral dust for this investigation. For comparison, literature values for mineral dust imaginary parts from Hess *et al.* (1998) and Müller *et al.* (2009b) are added.

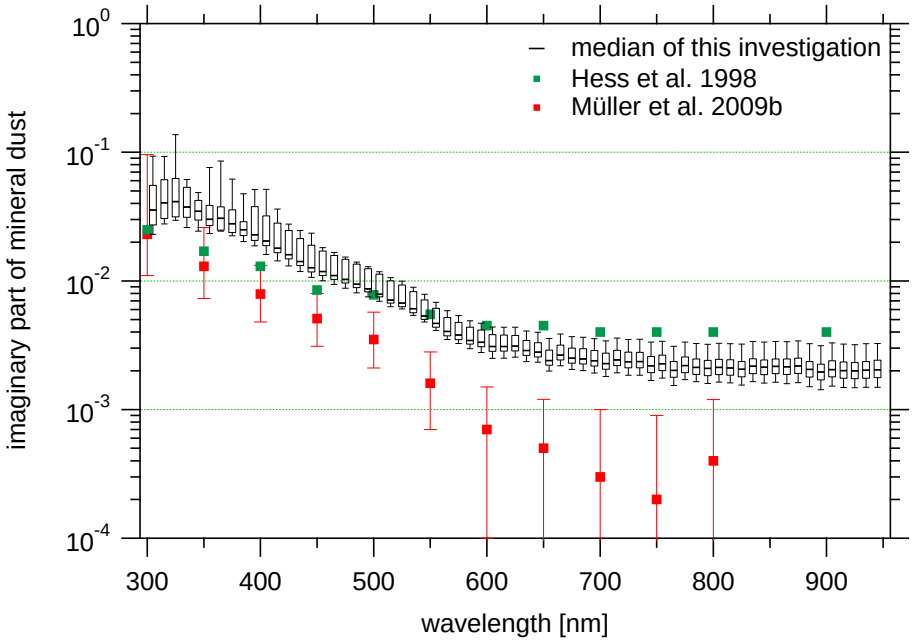

Figure 5.13: *Box plot of the imaginary part of the refractive index of mineral dust. The statistical analysis contains a dust volume fraction of at least 90% and data of at least 55 of 66 wavelengths per time interval. Literature values of imaginary parts for mineral dust are added for comparison.*

Table 5.3: *Literature values and arithmetic mean values from this investigation for the imaginary part of the refractive index for mineral dust. The data in the last column are arithmetic mean values from a time series containing a dust volume fraction of at least 90% and data of at least 55 of 66 wavelengths per time interval.*

wavelength [nm]	imaginary part n for mineral dust (Hess *et al.*, 1998)	imaginary part n for mineral dust (this investigation)
300	$2.5{\cdot}10^{-2}$	$4.5{\cdot}10^{-2}$
350	$1.7{\cdot}10^{-2}$	$3.7{\cdot}10^{-2}$
400	$1.3{\cdot}10^{-2}$	$2.8{\cdot}10^{-2}$
450	$8.5{\cdot}10^{-3}$	$1.5{\cdot}10^{-2}$
500	$7.8{\cdot}10^{-3}$	$1.0{\cdot}10^{-2}$
550	$5.5{\cdot}10^{-3}$	$5.6{\cdot}10^{-3}$
600	$4.5{\cdot}10^{-3}$	$3.7{\cdot}10^{-3}$
650	$4.5{\cdot}10^{-3}$	$2.9{\cdot}10^{-3}$
700	$4.0{\cdot}10^{-3}$	$2.7{\cdot}10^{-3}$
750	$4.0{\cdot}10^{-3}$	$2.7{\cdot}10^{-3}$
800	$4.0{\cdot}10^{-3}$	$2.5{\cdot}10^{-3}$
900	$4.0{\cdot}10^{-3}$	$2.4{\cdot}10^{-3}$

As expected from the dry absorption optical closure, the retrieved optical equivalent imaginary part for $\lambda < 550\,\text{nm}$ is larger than the values reported by Hess *et al.* (1998). In contrast to that, the imaginary parts of this investigation are somewhat lower for $\lambda > 550\,\text{nm}$. Comparing the imaginary parts with values for pure Saharan mineral dust derived by Müller *et al.* (2009b) during SAMUM-1, the imaginary parts from this investigation are shifted to larger values, which may have several reasons: Comparing the trajectory analysis for the lower air layers in Knippertz *et al.* (2009) with Knippertz *et al.* (2011), the Saharan dust during SAMUM-2 originated from more southeastward sources (Sahel region) than during SAMUM-1. Different chemical compositions of the Saharan dust may change the imaginary part of the refractive index. Another investigation (Kandler *et al.*, 2011) point out that the volume fraction of iron oxides was slightly higher than during SAMUM-1. Another reason might be aged soot particles, which accumulated on a mineral dust particle during transport, and causes an increase of the imaginary part of mineral dust. However, such a soot-dust mixture was rarely observed (Lieke *et al.*, 2011).
Table 5.3 shows the arithmetic mean values from this study, and additionally the literature values of the imaginary part for mineral dust. In the following, the optical equivalent imaginary part is used to describe the optical properties of the hydrophobic fraction of the coarse particle mode.

5.4 Influence of particle shape on AOPs at dry and humidified conditions

Many investigators (e.g., Koepke and Hess (1988); Nakajima *et al.* (1989); West *et al.* (1997); Kahnert *et al.* (2007)) used laboratory experiments to calculate non-sphericity effects of mineral dust particles. As pointed out in Mishchenko *et al.* (1997), the weakness of this method are missing values at scattering angles close to 0° and 180° due to the arrangement of source of light and detector. A widely used approach to simulate non-spherical effects is the semi-empirical theory by Pollack and Cuzzi (1980). The advantage of this method that is based on Mie theory is the easy implementation and the low computation effort. The disadvantage of this method is to determine the three free parameters to simulate a particle shape. Hence, this method is more convenient to adjust the semi-empirical theory to measurements of particle properties (e.g., the scattering phase function of non-spherical particles). Nevertheless, there are numerous studies (e.g., Kalashnikova and Sokolik (2002); Kalashnikova *et al.* (2005); Mishchenko *et al.* (1995, 1997); Bi *et al.* (2010)) that gave numerical solutions of optical properties for arbitrarily shaped particles, reproducing the non-spherical shape of mineral dust particles. The results from these studies can however be only approximations of non-sphericity effects on optical properties for this study, since the used PNSD, complex refractive indices, and equivalent particle diameter often deviate from each other, and additionally from this investigation. For this case, a database for spheroids, deformed spheroids and aggregates (Gasteiger *et al.*, 2011) was used. The database includes the S_{11} component

of the scattering matrix $\mathcal{M}$ (equation 2.2) as well as extinction (Q_e) and scattering efficiencies (Q_s). Here, the particle diameter of the non-spherical particle is defined as the diameter of a sphere that has the same volume (volume equivalent particle diameter). To simulate the effect on optical properties of modelled non-spherical dust particles, the optical equivalent imaginary parts from Table 5.3, and the corresponding real parts of the complex refractive index from Table 5.2 were used. The database for the deformed spheroids and aggregates include imaginary parts only up to $n = 3.44 \cdot 10^{-2}$. For this case, computations for these particle shapes were made only for wavelengths $\geq 400\,\text{nm}$. Beyond that, the computations of the deformed spheroids and aggregates using DDA are limited to a size parameter of $x \approx 25$. Hence, to compare the DDA results with results made with TMM (spheroids), and the reference case (spheres), the upper particle diameter of the PNSD was fixed to $dp_{ve} = 2650\,\text{nm}$.

For the calculation of the scattering matrix $\mathcal{M}$ of spheroids, a particle size independent aspect ratio distribution was taken from Wiegner *et al.* (2009) shown in their right column in Table 1. The optical properties of the deformed spheroids were averaged over three aspect ratios (1.4, 1.8, and 2.4). The deformed spheroids are prolate spheroids with surface deformations according to the Gardner series, as described in Gasteiger *et al.* (2011). For aggregate particles, a single shape is considered only. Figure 5.14 summarizes the ratio of non-spherical to spherical optical properties (non-sphericity factor) for the mineral dust particles in the coarse mode.

Non-sphericity factors of the extinction coefficient (scattering coefficient) range from 1.085 - 1.305 (1.094 - 1.363) at $\lambda = 450\,\text{nm}$ to 1.034 - 1.129 (1.035 - 1.133) at $\lambda = 880\,\text{nm}$, and are highest for the aggregates and lowest for the prolate spheroids. In other words, the smoother the particle the smaller is the non-sphericity factor. The non-sphericity factor of the extinction and the scattering coefficient shows additionally a wavelength dependency, and the influence of non-spherical particle shape decreases with increasing wavelength. This wavelength dependency is in agreement with the wavelength dependency of the scattering non-sphericity factors (cf. Figure 5.8) and with other investigations (e.g., Koepke and Hess (1988); Kalashnikova *et al.* (2005)). The enhancement of the extinction by non-spherical particles at short wavelengths may be explained by the fact that the cross section of a particle is the driving parameter for extinction, if particles are larger than the wavelength. For a given particle volume, the cross section of the particle and, as a consequence, the extinction increases with increasing non-sphericity of the particle.

An investigation by Kalashnikova and Sokolik (2002) reveals a non-sphericity factor for the extinction of about 1.3 at $\lambda = 550\,\text{nm}$. There, the particle shape was reconstructed from Saharan dust samples in the atmosphere yielding a so called representative composition-shape-size (CSS) distribution for Saharan dust particles. In another study, Kalashnikova *et al.* (2005) found differences in extinction up to a factor of 1.45 for weakly absorbing dust at $\lambda = 550\,\text{nm}$ by using modelled grain and plate-like particles.

Nevertheless, the aforementioned scattering and extinction non-sphericity factors are signif-

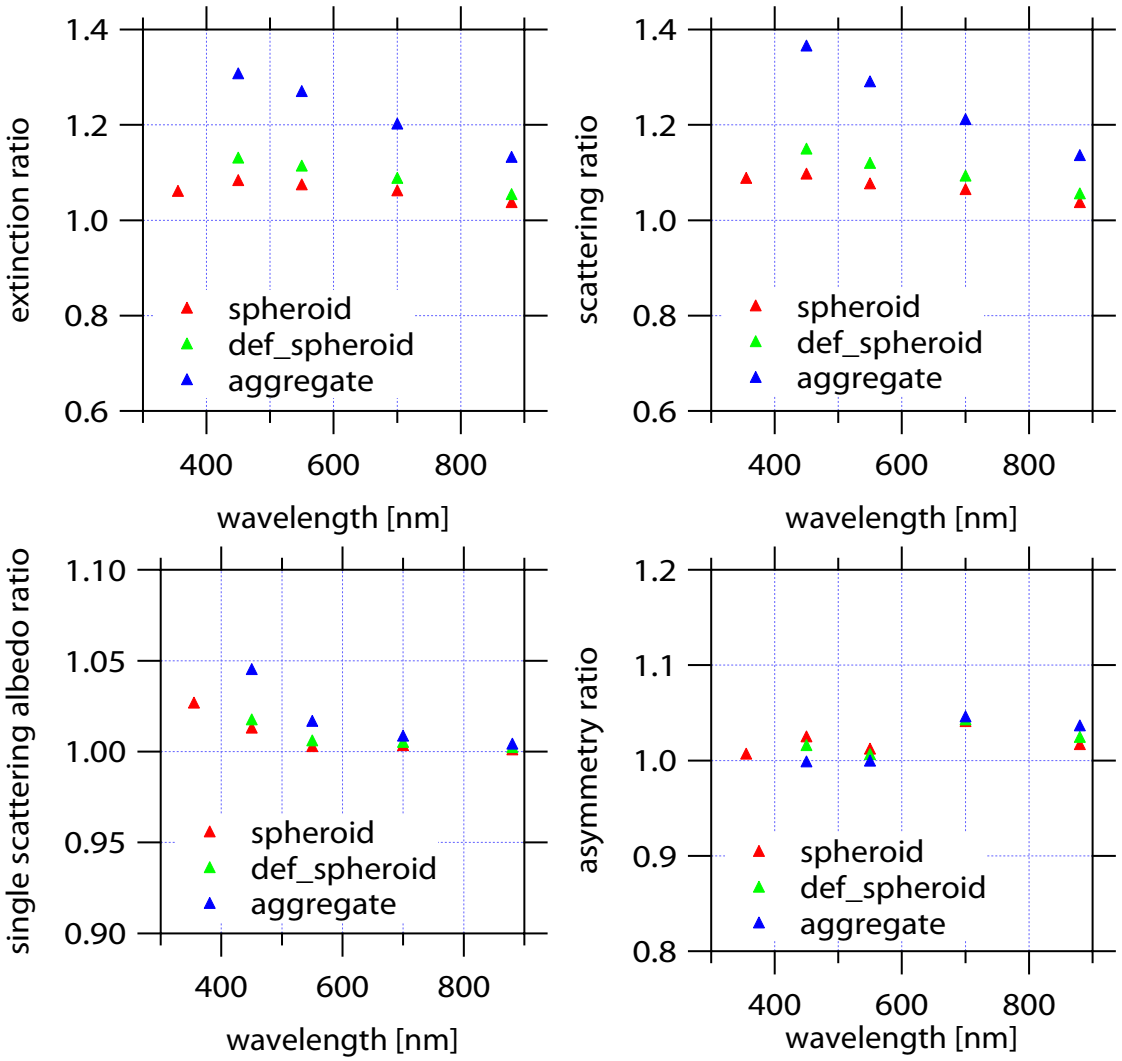

Figure 5.14: *Non-sphericity factors of optical properties for the mineral dust fraction of the coarse mode at several wavelengths. Optical properties are extinction and scattering coefficients as well as single scattering albedo and asymmetry parameter. Non-spherical approximations are prolate spheroids, prolate spheroids with surface deformations, and aggregates.*

icantly lower than the derived non-sphericity factors of mineral dust from this investigation (cf. Figure 5.8). For this instance, a laboratory experiment was performed, using a soil dust sample, collected near Zagora, Morocco during SAMUM-1. The setup of the laboratory study is shown in Figure 5.15.

Two nephelometer (Serial no. 1027 and 70847344, both: Model 3563, TSI Inc.) were connected with an aerosol chamber with a volume of about 0.5 m^3 to measure the nephelometer scattering coefficient. Downstream of the two nephelometers, an external pump of the MAAP sucked the aerosol through the nephelometer. This setup, using the MAAP pump as a vacuum supply for the nephelometer, was identical to the setup during the field campaign (cf. Figure 4.1). Two APS (Serial no. 1026 and 1089, both: model 3321, TSI Inc.) measured the PNSD in the size range from $0.57\mu m < dp_a < 10\mu m$. To make sure, that both APS and nephelometer measure the same aerosol, the connection tubes from the aerosol

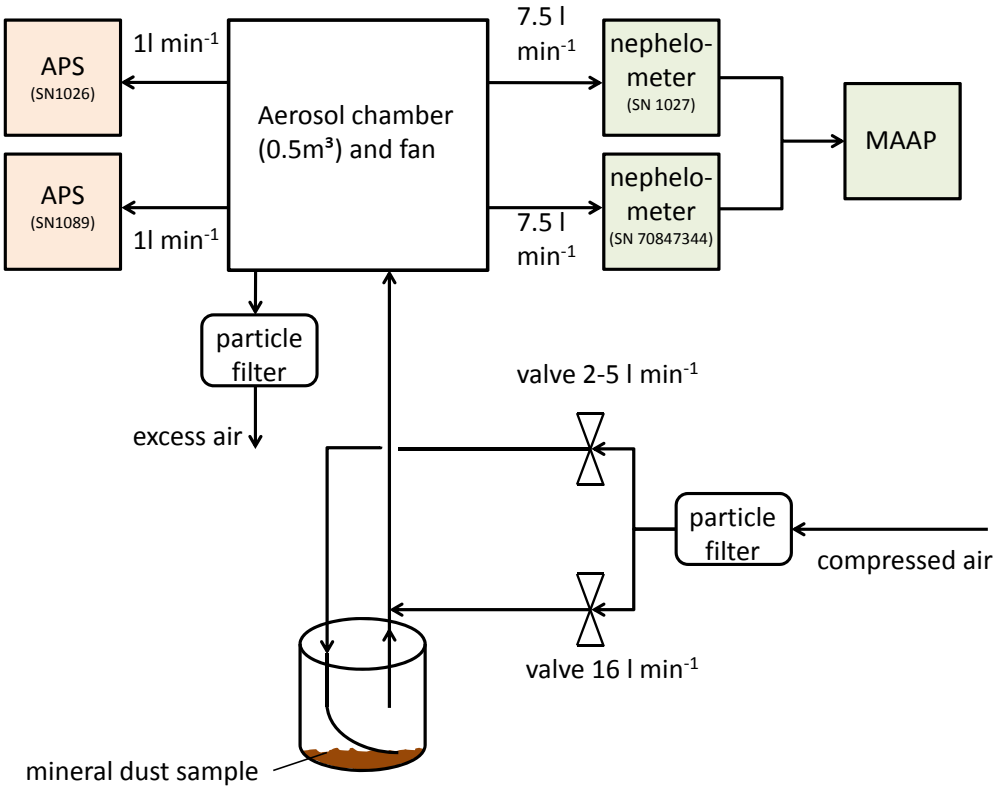

Figure 5.15: *Instrumental setup of the laboratory experiment to investigate differences in measured and Mie calculated nephelometer scattering coefficients.*

chamber to the instruments had nearly the same length and were as short as possible. Before starting the measurement, the aerosol chamber was flushed with particle free compressed air, to obtain a total particle number concentration $< 3\,\mathrm{cm}^{-3}$ in the APS size range. Afterwards, the mineral dust sample was dispersed in a reservoir using particle free compressed air with a variable flow rate of $2\text{-}5\,\mathrm{l\,min}^{-1}$. The subsequent mineral dust aerosol was additionally diluted and then drawn into the aerosol chamber. To guarantee that no contamination of particles occurred from outside, the excess flow in Figure 5.15 was checked to be always positive.

The correction of recorded aerodynamic particle diameters of both APS to volume equivalent particle diameters, was made according to chapter 4.1.2 by using the same effective particle density for mineral dust. The resulting particle number, surface, and volume size distribution of the dispersed mineral dust is shown in Figure 5.16. The particle size distributions show a narrow mono-modal shape, while the d_{gN} is around 600 nm, which is close to the d_{gN} of the first coarse particle mode (cf. Table 5.1). Because of the sizing limitations of the APS for the smaller particles, the left branch of the PNSD could not be completely resolved. However, with regard to compare measured and calculated scattering coefficients, the scattering is more correlated with the particle surface and particle volume. Figure 5.16 clarifies that more than 99% of the particle surface and volume was measured by the APS. In a next step, Mie calculations were performed, using the PNSD of both APS. As an input

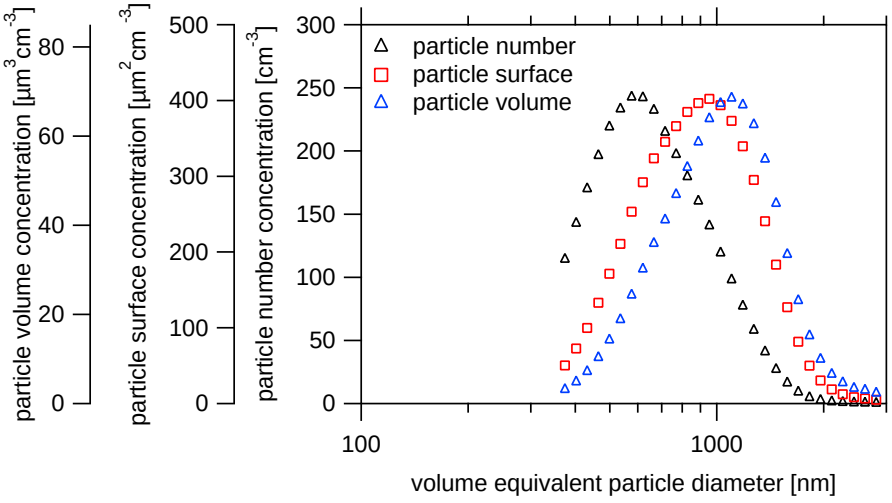

Figure 5.16: *Particle number, surface, and volume concentration of dispersed mineral dust soil sample.*

parameter for the Mie calculations, the complex refractive index of mineral dust derived by Müller *et al.* (2009b) during SAMUM-1 was used. It was not determined that the complex refractive index of the soil mineral dust and the mineral dust aerosol were the same. However, considering the fact that the particle surface and volume are the driving parameters for the scattering coefficient, this assumption is reasonable.

Figure 5.17 shows scatter plots of measured and calculated nephelometer scattering coefficient for each APS and nephelometer. In general, the measured values are higher than the calculated nephelometer scattering coefficients. The slope of the linear fits show a wavelength dependence, and values between 1.75 - 1.88, 1.55 - 1.67, and 1.39 - 1.46 at 450, 550, and 700 nm wavelength, respectively. The intercept of the fit around 1 Mm^{-1} can be explained by the lower detection limit of the nephelometer and is negligible. In spite of different mineral dusts at Cape Verde and in Morocco, the laboratory study quantitatively confirms the derived non-sphericity factors from the field campaign.

Now, coming back to the spheroids, deformed spheroids, and aggregates. Lower non-sphericity factors were found for the single scattering albedo (1 - 1.044) and the asymmetry parameter (0.997 - 1.045). For the three shape classes, the non-sphericity factor of the single scattering albedo shows a wavelength dependency and increases for smaller wavelengths. This property is basically caused by the stronger increase of the scattering non-sphericity factor in contrast to the extinction non-sphericity factor with decreasing wavelength. The non-sphericity factor of the asymmetry parameter doesn't show such a characteristic pattern.

Other investigations (e.g., Mishchenko *et al.* (1995, 1996); Kalashnikova and Sokolik (2002); Otto *et al.* (2009); Wiegner *et al.* (2009)) qualitatively confirm these small non-sphericity factors for the single scattering albedo and the asymmetry parameter by using spheroidal particles and randomly oriented, polydisperse circular cylinders. On the other hand, larger differences up to 1.2 for g for sharp edged modelled grain and plate-like particles was reported by Kalashnikova *et al.* (2005). Beside this large discrepancy in g, it seems unrealistic

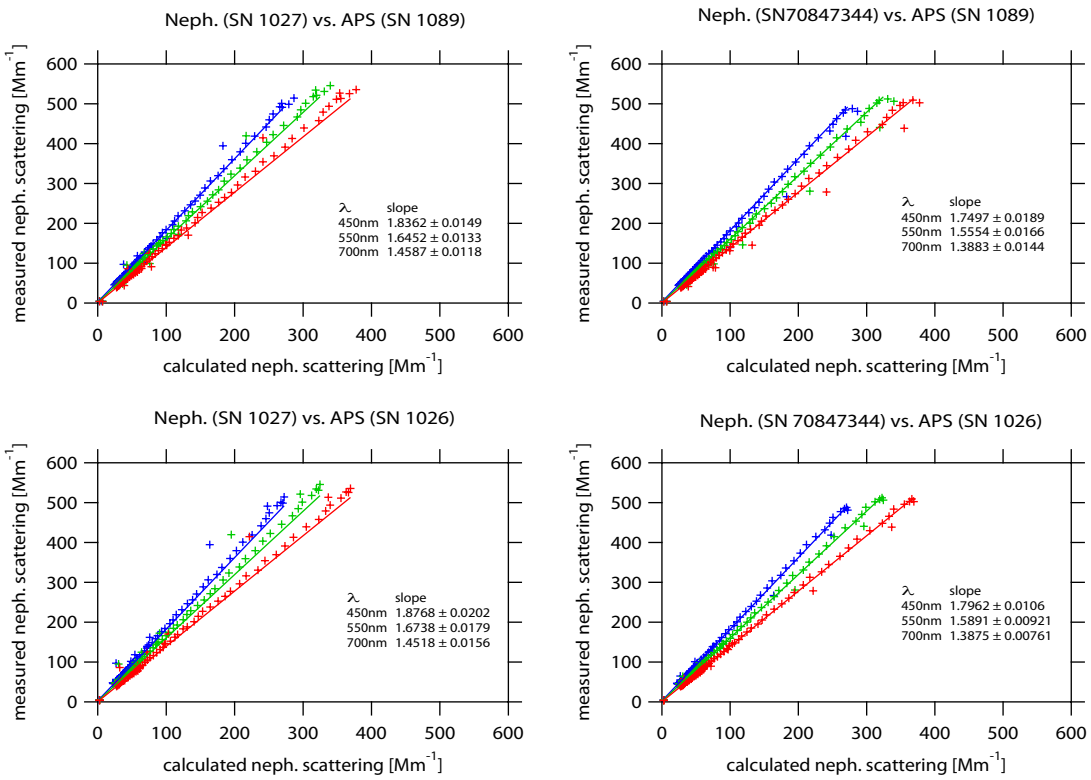

Figure 5.17: *Scatter plots of measured versus calculated nephelometer scattering coefficients at $\lambda = 450$, 550, and 700 nm of dispersed mineral dust. The parameters of the linear fits are added for each wavelength.*

that these sharp edged grain and plate-like represent the mineral dust particles well. Differences in the aerosol optical properties (AOPs) due to the non-spherical particle shape of mineral dust at dry conditions lead to consequences for quantification of AOPs at humidified conditions. Due to the nearly hydrophobic behavior of the Saharan mineral dust at Cape Verde, it is assumed that the AOPs and hence the non-sphericity factors do not change during the humidification process. For this case, the scattering non-sphericity factor (Figure 5.8) for the mineral dust component in the coarse particle mode is included in the aerosol model introduced in the following chapter 6.

6 Aerosol model calculations at ambient conditions

The aim of the aerosol model is to calculate microphysical and optical properties at ambient conditions, e.g., ambient mass concentration and ambient extinction coefficient. For this, the relative humidity measured at ambient conditions (cf. Figure 3.4b) is the single input parameter. A Mie-code for homogeneous spherical particles taken from Bohren and Huffman (1983) was applied to calculate optical properties.

The aerosol model describes the optical and microphysical properties of the marine and Saharan dust aerosol. The microphysical part of the aerosol model is described by time series of the lognormal size distributions and corresponding dry particle densities given in Table 5.2. Further microphysical properties are the hygroscopicity parameters κ and the corresponding mean hygroscopic and hydrophobic number fractions. The optical part in terms of the complex refractive index for each lognormal size distribution and mixing state is given in Tables 5.2 and 5.3. To describe the non-spherical shape of Saharan mineral dust, the wavelength-dependent non-sphericity factor for the particle scattering (Figure 5.8) is implemented.

The first step to calculate microphysical and optical properties at ambient condition, is to transform the dry PNSD being measured outside the measurement container. During the aerosol transport from outside to the measurement systems, sedimentation and impaction losses appeared for larger particles, while ultrafine particles underlie diffusion losses. In this thesis, the microphysical properties (e.g., particle mass concentration) and optical properties are more dominated by particles in the coarse particle mode than in the fine particle mode. Losses due to diffusion were neglected for this study. Particle losses were calculated for the particle segregation through the PM_{10} inlet and the transport system to the size spectrometers. The transport system consists of the automatic aerosol diffusion dryer, the aerosol splitter, and connection tubes to the size spectrometer. The aspiration efficiency for anisoaxial and anisokinetic sampling and the formulas for the impaction through inertia in bends and the sedimentation through gravitation in tubes are needed for laminar and turbulent flows and were taken from Brockmann (1993).

Starting at the inlet, the penetration curve of a PM_{10} inlet with a flow rate of $Q = 18\,\mathrm{l\,min^{-1}}$ (see Figure 4.1) that is close to the required flow rate of $Q = 16.7\,\mathrm{l\,min^{-1}}$ is given by Lee *et al.* (1986) and Liu *et al.* (1983). The particle transmission efficiency through the aerosol dryer is taken from Tuch *et al.* (2009). As shown in Figure 4.1, the aerosol splitter splits

the sample flow rate of the APS ($Q = 1\,\mathrm{l\,min^{-1}}$) from the total flow. The tube diameter reduces to 1/4" and thus the aerosol flow was split nearly isokinetically with minimal particle losses (cf. Figure 6.1). Downstream of the aerosol splitter, the APS was connected

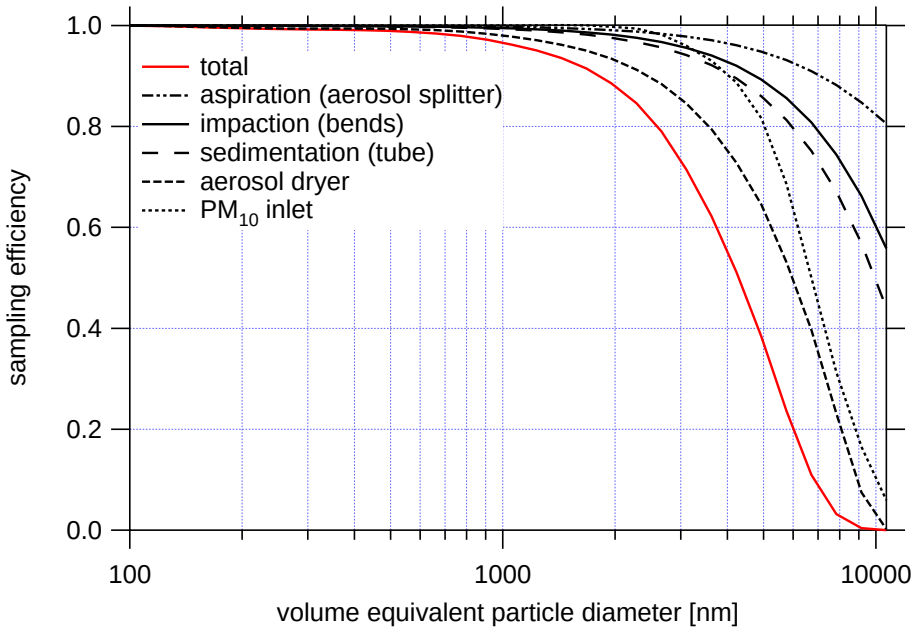

Figure 6.1: *Sampling efficiencies for the dry PNSD through particle transport losses in the sampling lines and particle segregation in the PM_{10} inlet.*

by 2 x 45° bends and a 0.5 m tube with an inclination angle of about 30°. The product of all transmission efficiencies is the total transmission efficiency for the dry PNSD, which is illustrated in Figure 6.1. For the following calculations, the dry PNSD was divided by the total transmission efficiency, yielding a dry PNSD, which was corrected for inlet particle losses.

6.1 Aerosol model validation at ambient conditions

6.1.1 Mass closure at ambient conditions

In order to carry out a closure for particle mass concentrations at ambient conditions, ambient temperature, pressure, and relative humidity, has to be considered. Since the ambient mass concentration was calculated from the dry PNSD, the thermodynamic conditions from the container have to be considered. The temperature and pressure during the measurement of the dry PNSD and during the measured PM_{10} and TSP mass concentrations at ambient conditions were nearly the same. However, PM_{10} and TSP mass concentrations were determined at about ∼55% RH, which deviates from the actual measured ambient RH at the site (cf. Figure 3.4). A RH of 55% is relevant, because the particle mass on the filter was determined at this RH.

First, the inlet loss corrected PNSD at dry state was transformed to ambient conditions. Therefore, each bin of the dry PNSD was multiplied with the time- and size-dependent mean

hygroscopic and hydrophobic number fractions (cf. mean hydrophobic number fraction in Figure 5.5), yielding a hygroscopic and a hydrophobic PNSD. The dry diameters of the hygroscopic and hydrophobic PNSDs were multiplied bin-wise with the mean hygroscopic growth factors at RH = 55%, which were in turn calculated from time- and size-dependent hygroscopicity parameters κ using equation 2.28. To ensure conservation of the total particle number concentration, the number concentrations of the size bins of the PNSDs were modified according to the change of the size interval width.

The solution droplet density $\rho(55\%)$ was determined bin-wise using the volume mixture rule (equation 4.13) and the time- and size-dependent mean hygroscopic growth factors at RH = 55%.

The upper panel of Figure 6.2 shows the time series of measured $PM_{2.5}$, PM_{10}, and TSP as well as calculated ambient mass concentrations (averaged according to the chemical sampling periods) at RH = 55% based on the procedure described above. Measured TSP mass

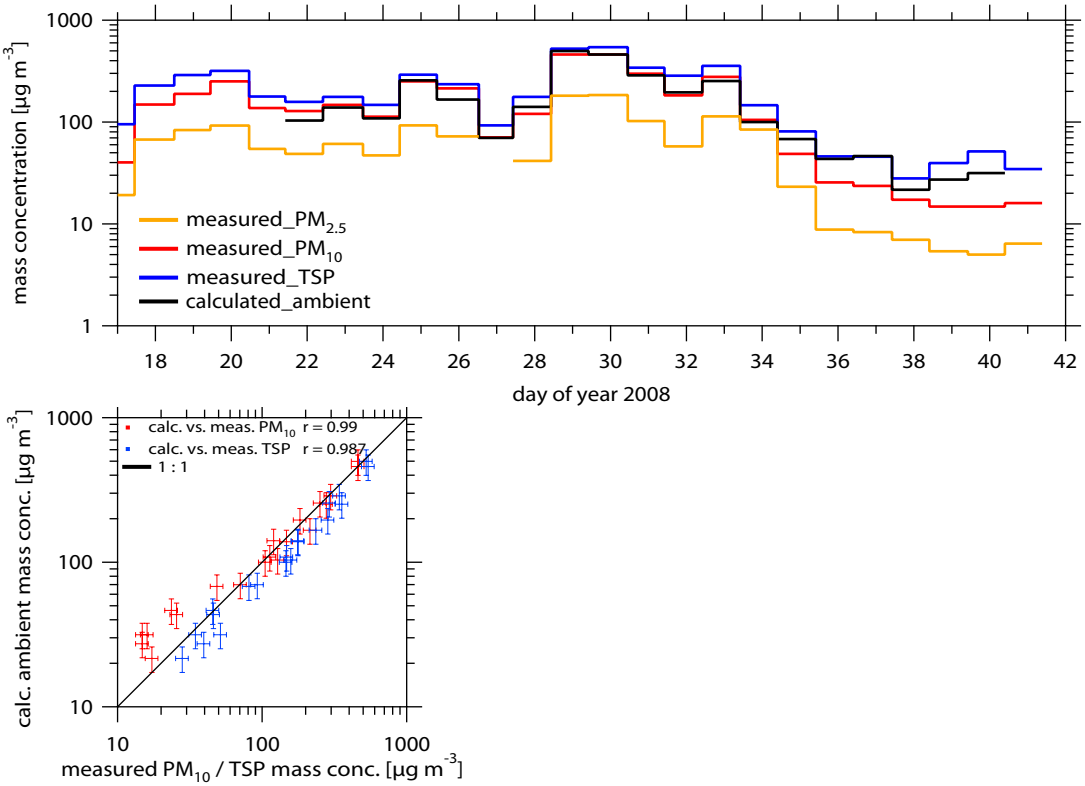

Figure 6.2: *Ambient mass closure at ∼55% RH. The upper panel shows a time series of measured $PM_{2.5}$, PM_{10}, and TSP as well as calculated ambient mass concentration. The lower panel shows a scatter plot of calculated ambient mass concentration versus measured PM_{10} and TSP mass concentration, respectively. The error of the calculated mass concentration was set to 20%, regarding uncertainties in quantifying the sampling efficiency of the dry PNSD (Figure 6.1).*

concentrations range from 28 to 542 $\mu g\,m^{-3}$, while the measured PM_{10} to TSP mass concentration ratio range from 28% to 91% with an arithmetic mean value of 68%. The lowest PM_{10} to TSP mass concentration ratio occurs in the last period starting DOY 34, with the lowest mass concentrations during the entire measurement period. The time series of the

$PM_{2.5}$ mass concentration shows a similar trend when comparing with the PM_{10} and TSP mass concentration. The coarse particle mode has a larger mass contribution to $PM_{2.5}$ than the fine particle mode. The lower panel of Figure 6.2 shows a scatter plot of calculated ambient mass concentration at RH = 55% versus measured PM_{10}, and TSP mass concentration. In general, the calculations and the measurements are highly correlated (r = 0.99) and lie close to the 1:1 line indicating the successful recalculation of particle mass concentrations by particle number based measurements. To be more specific, for high measured mass concentrations before DOY 34 LT, the calculated ambient and measured PM_{10} mass concentrations lie directly on the 1:1 line. In contrast to that, for lower mass concentrations (starting DOY 34 LT), the calculated ambient mass concentration is closer to the measured TSP than to the PM_{10} values. This finding gives a hint that the mass increase due to hygroscopic growth of large sea-salt particles significantly exceeds the measured PM_{10} value as the calculations are sensitive to these large particles and their hygroscopic behavior. In summary, the ratio of calculated ambient mass concentration to measured TSP mass concentration is between 61% and 101% with an arithmetic mean value of 79%. Hence, taking error bars into account, as illustrated in Figure 6.2, the aerosol model was successful to calculate almost the total mass of particles at ambient conditions.

6.1.2 Closure of optical properties at ambient conditions

The aim of this subsection is to validate the optical part of the aerosol model with the ambient measured extinction coefficient. The PNSD for each mode at the actual RH was calculated according to chapter 6.1.1. The complex refractive index at the actual RH was calculated bin-wise using the Maxwell-Garnet relation and the mean hygroscopic growth factor as:

$$\frac{\tilde{m}(\mathrm{RH})^2 - \tilde{m}^2}{\tilde{m}(\mathrm{RH})^2 + 2\tilde{m}^2} = \left(1 - \frac{1}{GF^3}\right) \cdot \frac{\tilde{m}_w^2 - \tilde{m}^2}{\tilde{m}_w^2 + 2\tilde{m}^2}. \tag{6.1}$$

The dry complex refractive indices are tabulated in Tables 5.2 and 5.3, while the wavelength-dependent complex refractive index of water $\tilde{m}_w$ is taken from Hale and Querry (1973). The calculations were done without the scattering non-sphericity for mineral dust, because the influence of particle non-sphericity at this wavelength is expected to be marginal when comparing with Figure 5.8. The thermodynamic conditions during measuring and calculating the extinction coefficient are different, because the calculations are based on container conditions. Thus, the extinction coefficient calculated for container conditions was adjusted to the actual ambient temperature T_{amb} and atmospheric pressure p_{amb} (Figure 3.4a and c) using equation:

$$\sigma_e(T_{amb}, p_{amb}) = \sigma_e \cdot \frac{293\,\mathrm{K}}{T_{amb}} \frac{p_{amb}}{1000\,\mathrm{hPa}}, \tag{6.2}$$

The extinction coefficient was measured at $p_{amb} \approx 1000\,\mathrm{hPa}$ (1.5 m above the container) that means the atmospheric pressure equals the pressure inside the measurement container. The closure between measured and calculated extinction requires a constant factor (cf. chapter 4.3.2) between calculated visibility sensor signal and extinction coefficient for the entire

measurement period. Figure 6.3(c) shows the result of these calculations as a scatter plot. It

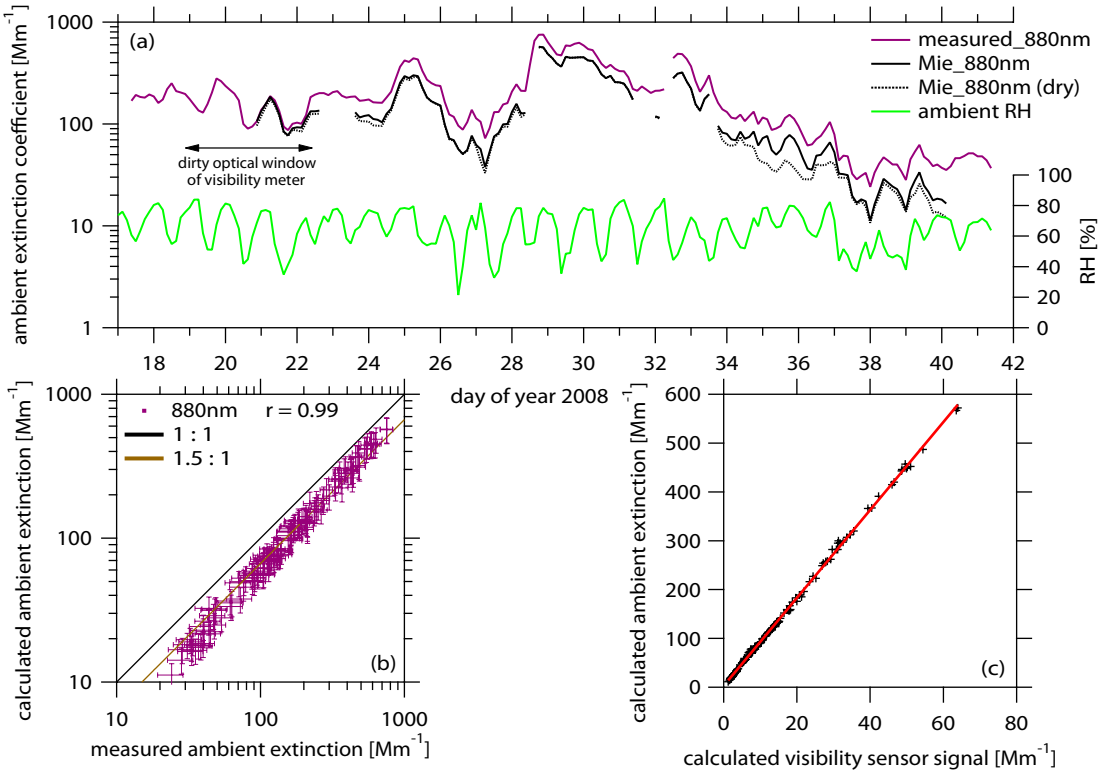

Figure 6.3: *Ambient extinction closure at ambient RH. (a) Time series of measured extinction as well as calculated extinction at the actual RH and under dry conditions. (b) Scatter plot of calculated versus measured extinction coefficient. The error of the calculated extinction coefficient was assumed to 20%, regarding uncertainties in quantifying the sampling efficiency of the dry PNSD (Figure 6.1). (c) Scatter plot of calculated extinction coefficient versus calculated receiver signal of the visibility sensor. The data were fitted using a linear regression.*

is obviously seen from the plot that the calculated visibility signal and extinction coefficient show a linear dependency and are connected by a constant factor. Figure 6.3(a) shows a time series of measured as well as calculated extinction at dry and ambient conditions. The measured ambient RH is added to the plot. The aerosol model reproduces the measured extinction very well, but deviated from it by a constant factor of about 1.5. Until DOY 34 LT, the calculated dry and ambient (RH) extinction do not differ significantly from each other. However, from DOY 34 LT on, the calculated dry and ambient (RH) extinction deviates. This behavior is caused by a lower dust fraction and thus a higher fraction of sea-salt particles. A higher fraction of hygroscopic sea-salt particles are grown up at RH between 40% and 80%, and this may enhance the extinction significantly. The calculated extinction reproduces the measured extinction for this last time period, which is evidence that the particles are in a metastable equilibrium (upper branch of the hysteresis of hygroscopic growth).

Figure 6.3(b) shows a scatter plot of calculated versus measured ambient extinction. Both values correlate very well ($r = 0.99$). In general, the measured ambient extinction is a con-

stant factor of ∼1.5 higher than the calculated ambient extinction. A possible reason for this discrepancy might be caused by the fog calibration of the visibility sensor. It is concluded that for the measurements at Cape Verde, the fog calibration overestimates the measured extinction coefficient. Despite of the discrepancy between measured and calculated ambient extinction, the aerosol model is able to simulate RH effects and thus hygroscopic growth effects on aerosol optical properties.

6.2 Comparison of calculated extinction coefficient with lidar measurements

This section proofs the applicability of the calculated extinction coefficient by the aerosol model in the atmospheric boundary layer. Vertical profiles of the extinction coefficient were measured with various lidar systems at the measurement site. Tesche *et al.* (2009) give an overview of the lidar systems. One of them, the MULIS lidar (Wiegner *et al.*, 1995; Freudenthaler *et al.*, 2009) has the strength, to measure columnar extinction and backscatter coefficients within the atmospheric boundary layer down to a height of ≈100 m above ground level. Therefore, the extinction coefficients from this lidar were compared with the calculated extinction from the ground. The lidar profiles of the particle extinction coefficients were analyzed with the Fernald-algorithm (Fernald, 1984), using the lidar ratio derived from simultaneous Raman measurements. For further details concerning the data processing and the determination of measurement errors refer to Groß*et al.* (2011).
In contrast to the lidar, the aerosol model wasn't developed to resolve the vertical structure of the extinction coefficient. For this issue, aerosol transport models were developed that can model e.g., the aerosol layering in the atmosphere. Now, the applicability of the aerosol model in the vertical was checked, assuming a height-independent PNSD from the ground. Vertically resolved meteorological parameters, e.g., relative humidity, atmospheric pressure, and temperature were provided at least once a day by radiosonde (Vaisala RS80, RS92) launches at the site. The relative humidity served as input for the aerosol model to calculate the RH-dependent vertical extinction coefficient.
Calculations of extinction coefficients of the total aerosol were done twice, from scattering coefficients including spherical dust particles (without consideration of non-sphericity factor), and from scattering coefficients including non-spherical dust particles (with consideration of non-sphericity factor). Employing equation 6.2, information about temperature and atmospheric pressure were used to adjust the calculated extinction coefficient from container to ambient conditions. Figures 6.4 and 6.5 show average vertical lidar profiles of the extinction coefficient at $\lambda = 532\,\text{nm}$ from DOY 29.786 - 29.8375 LT and DOY 37.604 - 37.625 LT, respectively. The calculated vertical profiles of the extinction coefficient are shown in the figures for comparison.
Figure 6.4 shows a case of high dust concentrations and therefore high extinction coefficients at the ground, while Figure 6.5 shows a case of low dust concentrations with more influence

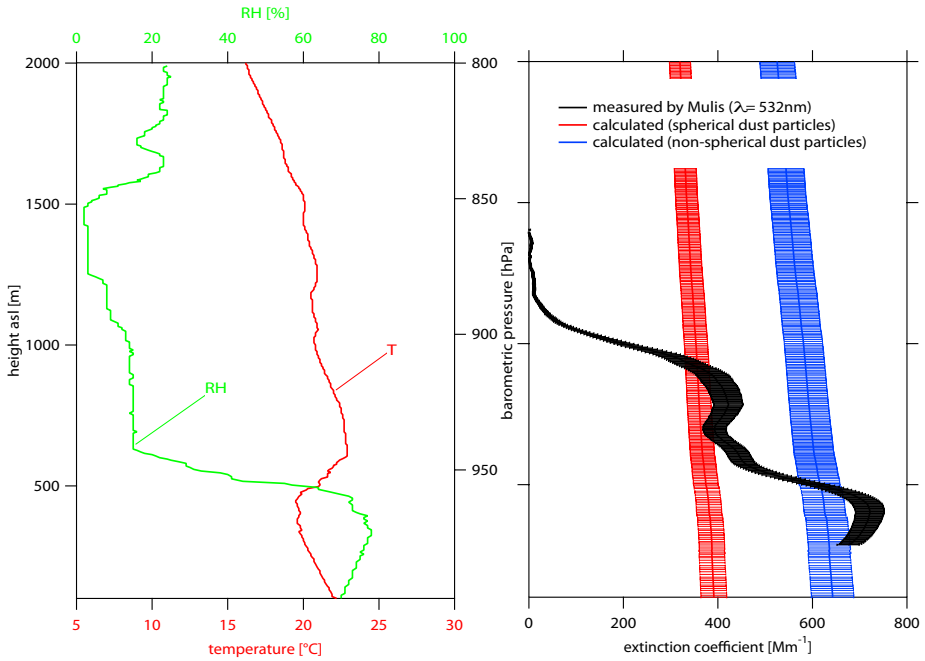

Figure 6.4: *(a) Radiosonde humidity and temperature profiles up to 2 km height at DOY 29.829 LT. (b) Measured (black line) and calculated (non-spherical dust particles: blue solid line, spherical dust particles: red solid line) profiles of the extinction coefficient averaged from DOY 29.744 - 29.796 LT.*

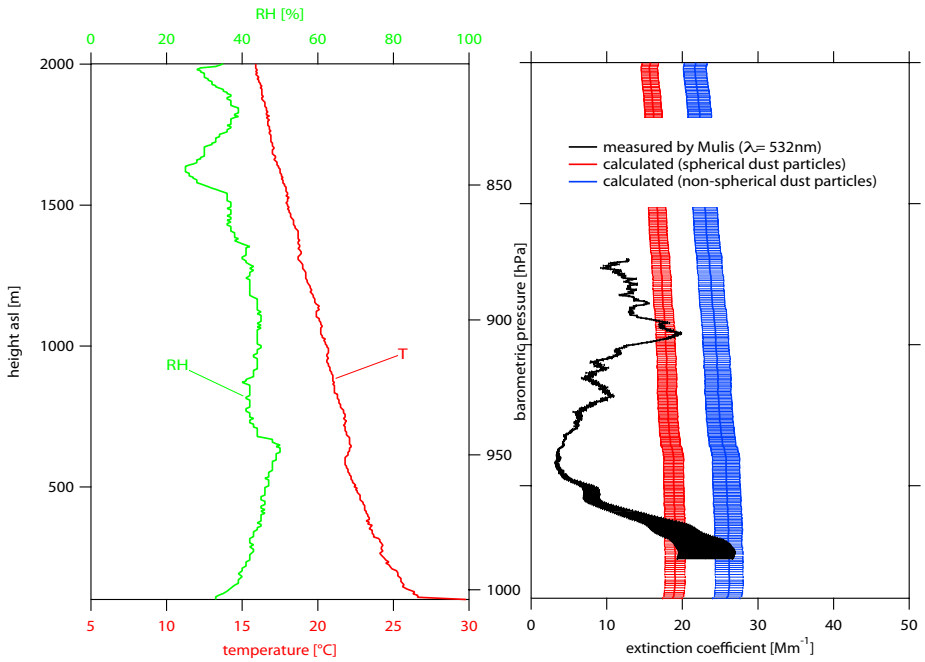

Figure 6.5: *(a) Radiosonde humidity and temperature profiles up to 2 km height at DOY 37.572 LT. (b) Measured (black line) and calculated (non-spherical dust particles: blue solid line, spherical dust particles: red solid line) profiles of the extinction coefficient averaged from DOY 37.563 - 37.583 LT.*

of marine aerosol. The radiosonde humidity and temperature profiles in Figure 6.4 indicate a shallow marine boundary layer (MBL) up to 400 m above sea level. The adjacent temperature inversion and a decreasing relative humidity indicate the Saharan dust layer. In the MBL, the measured extinction coefficient increases up to 700 Mm^{-1}. The calculated profiles show large differences applying spherical and non-spherical dust particles. In the MBL the non-spherical approach agrees within the measured extinction coefficient (relative deviation of 6%±11%), while the spherical model does not (relative deviation of 73%±13%). The comparison at high dust concentrations clearly revealed that an assumption of spherical dust particles significantly underestimates the extinction coefficients.

In contrast to Figure 6.4, Figure 6.5 indicates not such a clear layering in the radiosonde profiles. The radiosonde profiles revealed only a small temperature inversion at about 650 m height asl, which assigns the top of the MBL. As illustrated in Figure 1 in Knippertz *et al.* (2011), the adjacent upper aerosol layer is composed of dust and smoke. In the MBL, the measured extinction coefficient increases up to 25 Mm^{-1}. For the lowermost layer, the spherical as well as the non-spherical calculations agree with the measured extinction profile (relative deviation of 17%±29% and 12%±23%, respectively). This fact is not surprising, because the lower the dust particle number concentration is, the lower is the effect of non-sphericity of the extinction coefficient. The quantification of aerosol optical properties at ambient conditions, e.g., extinction coefficients is a great afford, especially when non-sphericity effects have to be taken into account.

To summarize, both case studies revealed that on the one hand the aerosol model is not capable to reproduce the extinction profile in the MBL. On the other hand, with the aerosol model it is however possible to extend the extinction profile of lidar measurements to the ground. It is important to have a complete profile from the ground to the uppermost layers, when comparing the column integrated aerosol optical thickness, with directly measured from the sun-photometer. In both presented case studies, the extinction coefficient is highest in the lowermost layers. Disregarding of these not by lidar detectable layers may lead to systematic errors for such intercomparison studies.

7 Parameterizations

7.1 Parameterizations of humidity effects of optical aerosol properties

Time series of aerosol optical properties were calculated at the dry state and at relative humidities of 55, 75, and 90% for the wavelength range from 300 to 950 nm in steps of 50 nm using the aerosol model. The calculated aerosol optical properties are the absorption, scattering, and extinction coefficients as well as the single scattering albedo, and asymmetry parameter. As revealed in chapter 5.3.1 and confirmed in a laboratory study in chapter 5.4, the scattering coefficient of mineral dust particles differ significantly between non-spherical and spherical particle shape. Therefore, calculations of the scattering coefficient for the hydrophobic fraction of the coarse mode were made for spherical and non-spherical mineral dust particles. Extinction coefficients for the hydrophobic fraction of the coarse particle mode were calculated from the sum of the scattering coefficient (with and without scattering non-sphericity factor) and the absorption coefficient. As revealed in chapter 5.3.2, the absorption coefficient of the hydrophobic fraction of the coarse mode was calculated using the optical equivalent imaginary part. Also, the single scattering albedo of the total aerosol was calculated twice, from scattering and extinction coefficients including spherical dust particles, and from scattering and extinction coefficients including non-spherical dust particles.

The RH dependence of the aerosol optical properties (AOP) can be described by the humidification factor

$$\xi_{\mathrm{AOP}}(\lambda, \mathrm{RH}) = \frac{\mathrm{AOP}(\lambda, \mathrm{RH})}{\mathrm{AOP}(\lambda, \mathrm{dry})}, \tag{7.1}$$

in analogy to the definition of the growth factor (cf. equation 2.26). Here, AOP(dry) refer to $\mathrm{RH} < 30\%$. This value is close enough to dry conditions, because it is supposed that further drying of the air does not change the AOP (Charlson *et al.*, 1984). Humidification factors were calculated for the extinction (ξ_e), scattering (ξ_s), and absorption coefficient (ξ_a) as well as for the single scattering albedo (ξ_{ω_0}) and the asymmetry parameter (ξ_g). An often used parametrization of ξ_{AOP} is based on a power law, (e.g., Kasten (1969); Hänel (1976); Hegg *et al.* (1996); Grant *et al.* (1999); Anderson *et al.* (2003); Carrico *et al.* (2003); Quinn *et al.* (2005); Nessler *et al.* (2005); Cheng *et al.* (2008)). The dependency of ξ_{AOP} on RH results from the power law characteristic of the metastable branch of the hysteresis of hygroscopic growth (cf. Figure 2.3). The goal of this investigation was to find a simple parametrization

of ξ_{AOP} for further use in radiative transfer models. The best fit for all AOPs was found by using equation:

$$\xi_{\mathrm{AOP}}(\lambda, \mathrm{RH}) = \left(1 - \frac{\mathrm{RH}}{100}\right)^{\gamma(\lambda)\cdot\frac{\mathrm{RH}}{100}}, \tag{7.2}$$

where the free parameter $\gamma(\lambda)$ was derived using a nonlinear least-squares routine (Levenberg-Marquardt method). This was done for $\xi_e, \xi_s, \xi_a, \xi_g$, whereas ξ_{ω_0} can be derived from ξ_e and ξ_s and the humidification factor for the single scattering albedo is given as

$$\xi_{\omega_0} = \frac{\xi_s}{\xi_e}. \tag{7.3}$$

Equation 7.2 equals equation 5 in Cheng *et al.* (2008) for $\mathrm{RH}_0 = 0\%$ and is valid in the range from 0% - 90% RH. In equation 7.2, the power increases with increasing RH, accounting for the steeper behavior of ξ_{AOP} at high RH. The advantage of this formulation is to describe the RH dependency of the power with no further parameter. For instance, Hänel (1984) used different power functions to parameterize the humidification factors for several RH ranges.

A general correlation of $\gamma(\lambda)$ and λ was not found, but Cheng *et al.* (2008) reported that the free parameter $\gamma(\lambda)$ depends on the chemical composition. Figures A.1 to A.6 show the $\gamma(\lambda)$ value versus the dry dust volume fraction vf_{dust} in the wavelength range from 300 to 950 nm. The lowest γ values and thus the largest humidification factors are found for the scattering coefficient followed by the extinction and the absorption coefficients. This is in consistency to Hänel (1984). Quinn *et al.* (2005) parameterized the γ value as a linear function of the relative amount of organic particulate matter for submicrometer aerosol. Similar to this investigation, Howell *et al.* (2006) showed a measured ξ_s dependence on the dust volume fraction during ACE-Asia. On the basis of Howell *et al.* (2006), it was found to be adequate to parameterize $\gamma(\lambda)$ as a function of vf_{dust} using a power law formalism:

$$\gamma(\lambda) = y_0(\lambda) + A(\lambda) \cdot (vf_{dust})^{pow(\lambda)}. \tag{7.4}$$

For this study, the three free parameters $y_0(\lambda)$, $A(\lambda)$, and $pow(\lambda)$ were determined for each AOP by a nonlinear least-squares fit. The best fit function and the fit parameters ± single standard deviation are shown in Figures A.1 to A.6. Beyond that, Tables 7.1 to 7.4 summarize the fit parameters for ξ_e, ξ_s, ξ_a, ξ_g and for each wavelength. For ξ_e and ξ_s, the fit parameters are added for non-spherical dust particles, following the remarks in chapter 5.4. In contrast to $\gamma(\lambda)$, the three fit parameters $y_0(\lambda)$, $A(\lambda)$, and $pow(\lambda)$ and the wavelength are clearly connected. For the extinction, scattering, and absorption y_0 decreases, and A increases with increasing wavelength. For the extinction and scattering, pow decreases with increasing wavelength.

In a special case, when $vf_{dust} = 0$, equation 7.4 simplifies to $\gamma(\lambda) = y_0(\lambda)$. This means, the parameter $y_0(\lambda)$ represents the pure marine aerosol. During the measurement campaign, the dry dust volume fraction varied between 0.5 and 1.0. Strictly speaking, equation 7.4

is only valid in the range of vf_{dust} given above. The aim is to extend the applicability of equation 7.4 from $vf_{dust} = 0$ to $vf_{dust} = 1$. To check the validity of this equation at $vf_{dust} = 0$, the humidification factors $\xi_e, \xi_s, \xi_a, \xi_{\omega_0}$, and ξ_g were calculated in the range from 0 to 90% RH and compared with literature values.

In literature, humidification factors for specific aerosols, several AOPs and additionally for a wide range of RH are primarily based on model calculations. Directly measured humidification factors of several AOPs for marine aerosol are rare. One humidification factor, ξ_s was measured by Covert *et al.* (1972) and Anderson *et al.* (2003) using a combination of a humidified and a dry nephelometer. By using the same measurement technique, Hegg *et al.* (1996), Carrico *et al.* (1998), Kotchenruther *et al.* (1999), and Carrico *et al.* (2003) reported measured ξ_s ranging from 2.0 - 2.5 for marine aerosol at 80% RH. The humidification factors for the scattering coefficient from this investigation (cf. Figure 7.2 lie within this range).

Now, the calculated humidification factors for pure marine aerosol (setting $\gamma(\lambda) = y_0(\lambda)$ in equation 7.2) were compared with modelled humidification factors from literature at RH = 50, 70, 80, and 90%. First, the models are introduced, which are the "maritime-polluted" aerosol (D'Almeida *et al.*, 1991), the "maritime model" (Shettle and Fenn, 1979), and the "maritime aerosol (model 3)" (Hänel, 1976). The humidification factors from D'Almeida *et al.* (1991) are valid for polluted maritime environment in the Mediterranean and the north Atlantic and based on three lognormal size distributions. The "maritime-polluted" aerosol comprises water-soluble, soot, and sea-salt lognormal size distribution. The particle growth to equilibrium size at a distinct relative humidity is based on Köhler theory, whereas the AOPs are calculated with Mie theory. The humidification factors from Hänel (1976) are based on measured particle mass, mean particle density, and real part of the complex refractive index for specific relative humidities onboard the research vessel "Meteor" in 1969 over the central Atlantic. The AOPs of interest (here: ξ_e, ξ_a, and ξ_{ω_0} at $\lambda = 300$ and 550 nm) for the "maritime aerosol (model 3)" were calculated by Hänel (1976) using Mie theory. The "maritime model" from Shettle and Fenn (1979) is composed of a so called "rural model" and a sea-salt component. The respective particle growth factors stem from Hänel (1976) from his "model 6" and "model 2". The calculation of the AOPs of interest (here: ξ_e, ξ_s, ξ_a, ξ_{ω_0}, and ξ_g at $\lambda = 300$, 550, and 700 nm) was also done with Mie theory.

For ξ_e and ξ_s (Figures 7.1 and 7.2), the best agreement (average relative deviation[1] of 5.7% and 7.6%, respectively) - in particular for higher relative humidities - is found for the "maritime-polluted" aerosol from (D'Almeida *et al.*, 1991). The values for ξ_a (Figure 7.3) of this study lie between the "maritime - polluted" aerosol and the "maritime model", while the latter show $\xi_a < 1$. In contrast to this, for ξ_{ω_0} (Figure 7.5), the best agreement (average relative deviation of 0.1%) is found for the "maritime model" by Shettle and Fenn (1979). For ξ_{ω_0}, the "maritime aerosol (model 3)" by Hänel (1976) shows the largest values at all. Hänel (1976) reported very low single scattering albedos around 0.7 at dry conditions in the visible

[1] The average relative deviation is the relative deviation for the humidification factor from literature and this investigation, averaged for 3(4) wavelengths and 4 RHs.

spectral range. The difference from the dry value to single scattering albedos larger than 0.9 at humidified conditions induces such large values for ξ_{ω_0}. For ξ_g (Figure 7.4), the best agreement (average relative deviation of 0.5%) is again found for the "maritime-polluted" aerosol. To conclude, in literature there are still differences between humidification factors of one aerosol type. The humidification factors for pure marine aerosol from this investigation agree within the variability of literature values. Therefore, it seems reasonable to extend the validity of the parametrization (equation 7.4) from $vf_{dust} = 0$ to $vf_{dust} = 1$.

Table 7.1: *Coefficients ± single standard deviation for the humidification factor of the extinction coefficient for spherical (sph) and non-spherical (nsp) dust particles.*

λ [nm]	y_0(sph)	y_0(nsp)	A(sph)	A(nsp)	pow(sph)	pow(nsp)
300	-0.521±0.026	-0.587±0.055	0.483±0.024	0.567±0.053	3.145±0.355	1.777±0.273
350	-0.546±0.029	-0.618±0.061	0.512±0.027	0.599±0.059	2.932±0.339	1.71±0.273
400	-0.561±0.031	-0.635±0.065	0.533±0.029	0.619±0.062	2.792±0.325	1.664±0.27
450	-0.576±0.033	-0.659±0.07	0.552±0.031	0.646±0.068	2.669±0.305	1.568±0.259
500	-0.575±0.034	-0.661±0.073	0.555±0.032	0.65±0.071	2.535±0.291	1.505±0.254
550	-0.582±0.035	-0.666±0.074	0.566±0.033	0.657±0.071	2.457±0.282	1.501±0.251
600	-0.582±0.037	-0.661±0.072	0.568±0.034	0.653±0.07	2.364±0.275	1.506±0.25
650	-0.584±0.039	-0.661±0.073	0.572±0.037	0.653±0.071	2.234±0.269	1.488±0.249
700	-0.587±0.041	-0.651±0.069	0.576±0.039	0.643±0.067	2.181±0.268	1.552±0.252
750	-0.593±0.044	-0.647±0.068	0.583±0.041	0.64±0.066	2.096±0.269	1.585±0.256
800	-0.594±0.047	-0.638±0.067	0.585±0.045	0.631±0.064	2.003±0.27	1.601±0.261
850	-0.604±0.052	-0.636±0.066	0.595±0.049	0.628±0.064	1.953±0.282	1.673±0.275
900	-0.603±0.052	-0.621±0.06	0.596±0.05	0.614±0.058	1.908±0.275	1.753±0.272
950	-0.615±0.055	-0.619±0.056	0.609±0.052	0.612±0.054	1.891±0.278	1.86±0.277

Table 7.2: *Coefficients ± single standard deviation for the humidification factor of the scattering coefficient for spherical (sph) and non-spherical (nsp) dust particles.*

λ [nm]	y_0(sph)	y_0(nsp)	A(sph)	A(nsp)	pow(sph)	pow(nsp)
300	-0.529±0.017	-0.576±0.039	0.469±0.017	0.55±0.037	4.821±0.475	2.284±0.289
350	-0.55±0.02	-0.602±0.043	0.497±0.019	0.578±0.041	4.313±0.431	2.194±0.288
400	-0.564±0.022	-0.619±0.048	0.522±0.021	0.599±0.045	3.846±0.386	2.077±0.282
450	-0.583±0.026	-0.65±0.057	0.552±0.024	0.635±0.055	3.271±0.331	1.825±0.264
500	-0.583±0.029	-0.655±0.062	0.56±0.027	0.644±0.06	2.922±0.303	1.689±0.256
550	-0.593±0.032	-0.668±0.067	0.575±0.03	0.659±0.064	2.667±0.284	1.608±0.25
600	-0.593±0.034	-0.667±0.067	0.579±0.032	0.658±0.065	2.498±0.272	1.579±0.246
650	-0.594±0.037	-0.667±0.069	0.582±0.034	0.659±0.067	2.331±0.264	1.545±0.244
700	-0.596±0.038	-0.657±0.065	0.585±0.036	0.65±0.063	2.266±0.261	1.605±0.246
750	-0.601±0.041	-0.654±0.064	0.592±0.039	0.647±0.062	2.17±0.261	1.635±0.249
800	-0.601±0.044	-0.644±0.063	0.593±0.042	0.637±0.06	2.073±0.261	1.662±0.253
850	-0.609±0.048	-0.64±0.062	0.601±0.046	0.633±0.06	2.021±0.273	1.729±0.267
900	-0.608±0.049	-0.625±0.056	0.602±0.046	0.619±0.054	1.97±0.266	1.807±0.263
950	-0.62±0.051	-0.623±0.052	0.614±0.049	0.617±0.05	1.951±0.269	1.919±0.268

Table 7.3: *Coefficients ± single standard deviation for the humidification factor of the absorption coefficient.*

λ [nm]	y_0	A	pow
300	-0.017±0.006	0.017±0.006	1±0.483
350	-0.014±0.005	0.013±0.004	1±0.449
400	-0.013±0.004	0.013±0.004	1±0.472
450	-0.018±0.006	0.018±0.005	1±0.415
500	-0.024±0.007	0.024±0.007	1±0.404
550	-0.036±0.011	0.035±0.011	1±0.407
600	-0.049±0.014	0.047±0.014	1±0.391
650	-0.054±0.012	0.051±0.012	1.175±0.392
700	-0.061±0.015	0.059±0.014	1.14±0.392
750	-0.068±0.016	0.065±0.016	1.148±0.39
800	-0.074±0.019	0.071±0.019	1.091±0.391
850	-0.08±0.023	0.077±0.023	1±0.397
900	-0.083±0.022	0.08±0.021	1.072±0.393
950	-0.087±0.024	0.083±0.023	1.038±0.393

Table 7.4: *Coefficients ± single standard deviation for the humidification factor of the asymmetry parameter.*

λ [nm]	y_0	A	pow
300	-0.073±0.013	0.079±0.013	1±0.221
350	-0.084±0.013	0.088±0.012	1±0.189
400	-0.079±0.008	0.081±0.008	1.343±0.188
450	-0.059±0.003	0.058±0.003	2.587±0.225
500	-0.064±0.002	0.062±0.002	2.856±0.222
550	-0.054±0.002	0.053±0.002	3.173±0.227
600	-0.062±0.002	0.061±0.002	3.367±0.231
650	-0.054±0.002	0.053±0.002	3.115±0.231
700	-0.06±0.002	0.059±0.002	3.173±0.233
750	-0.049±0.002	0.048±0.002	2.936±0.259
800	-0.058±0.003	0.057±0.003	2.895±0.28
850	-0.052±0.003	0.052±0.003	2.981±0.319
900	-0.052±0.003	0.051±0.003	2.723±0.353
950	-0.057±0.004	0.056±0.003	2.856±0.36

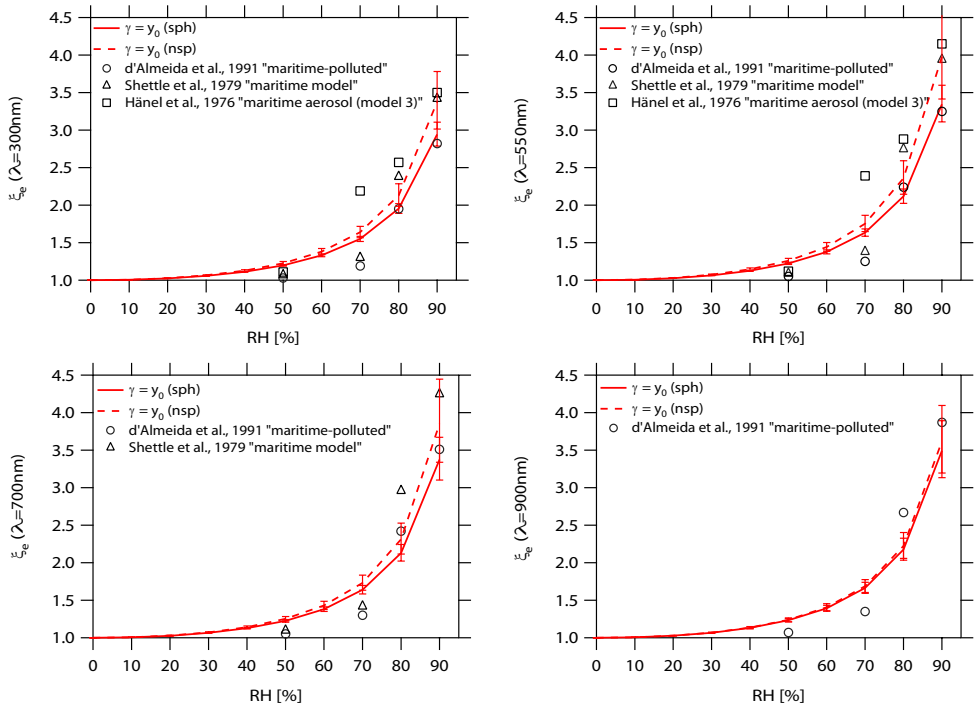

Figure 7.1: *Comparison of humidification factors for the extinction coefficient for the marine aerosol. Humidification factors from this investigation for spherical dust particles (red solid line) and non-spherical dust particles (red dashed line) are shown. The corresponding error bars result from the standard deviation of* y_0*. Additionally shown are humidification factors from D'Almeida et al. (1991) (hollow circles), from Shettle and Fenn (1979) (hollow triangles), and from Hänel (1976) (hollow squares).*

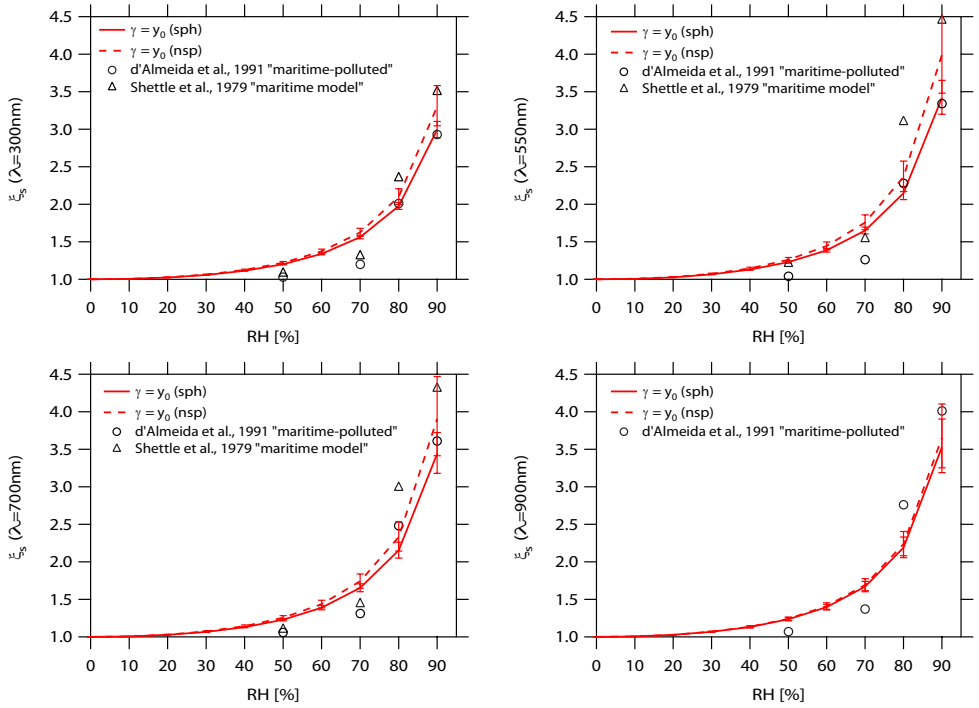

Figure 7.2: *Same as Figure 7.1 but for scattering. Additionally shown are humidification factors from D'Almeida et al. (1991) (hollow circles) and from Shettle and Fenn (1979) (hollow triangles).*

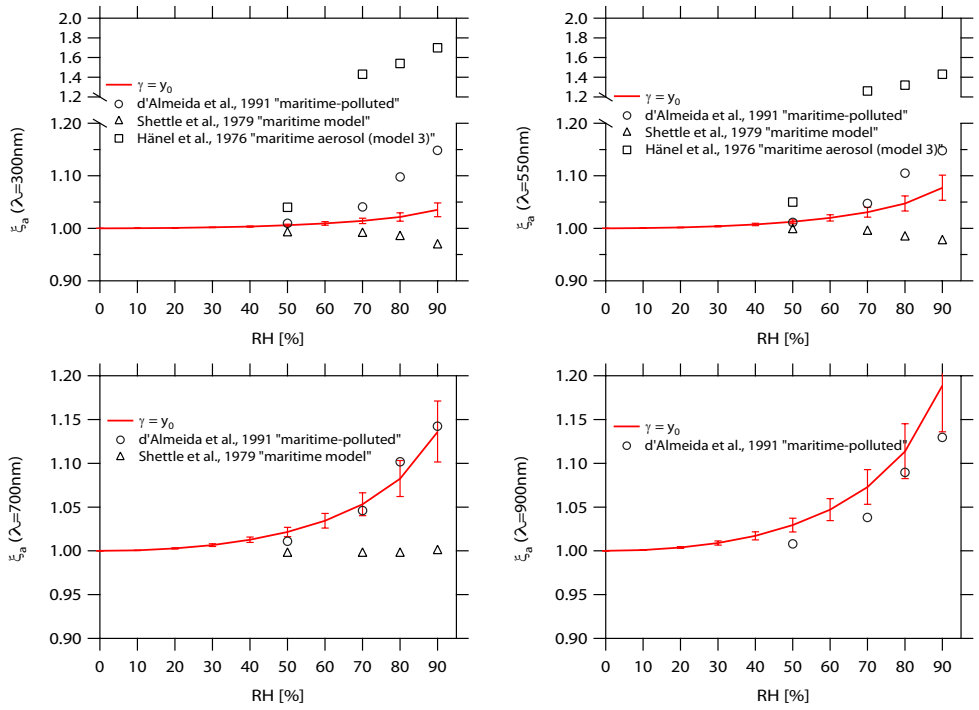

Figure 7.3: *Comparison of humidification factors for the absorption coefficient for the marine aerosol. Humidification factors from this investigation for spherical dust particles (red solid line) are shown. The corresponding error bars result from the standard deviation of y_0. Additionally shown are humidification factors from D'Almeida et al. (1991) (hollow circles), from Shettle and Fenn (1979) (hollow triangles), and from Hänel (1976) (hollow squares).*

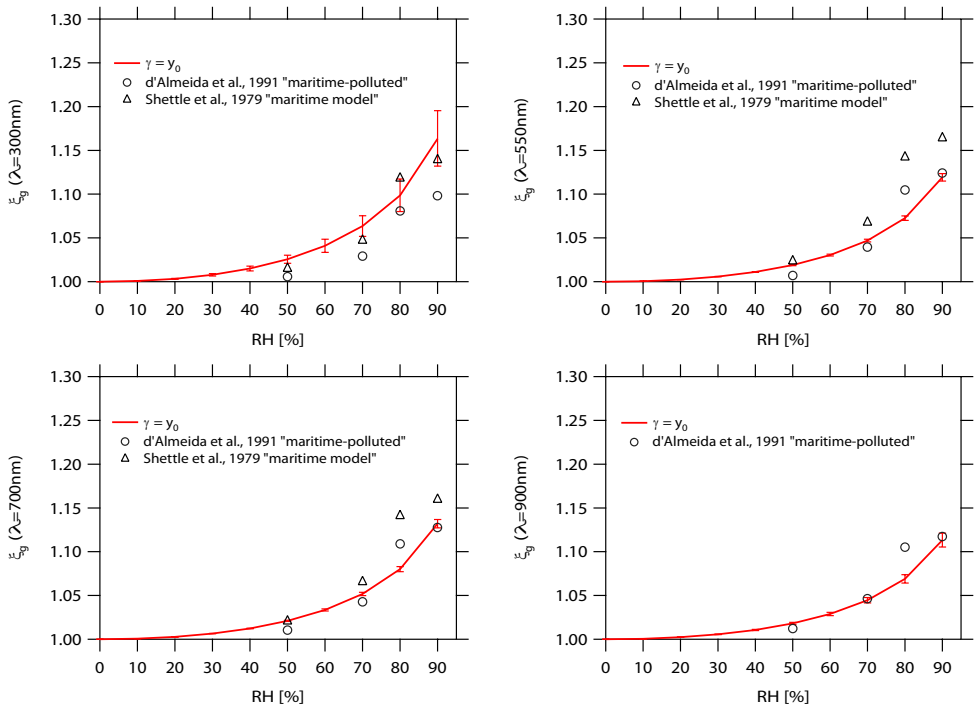

Figure 7.4: *Same as Figure 7.3 but for the asymmetry parameter. Additionally shown are humidification factors from D'Almeida et al. (1991) (hollow circles) and from Shettle and Fenn (1979) (hollow triangles).*

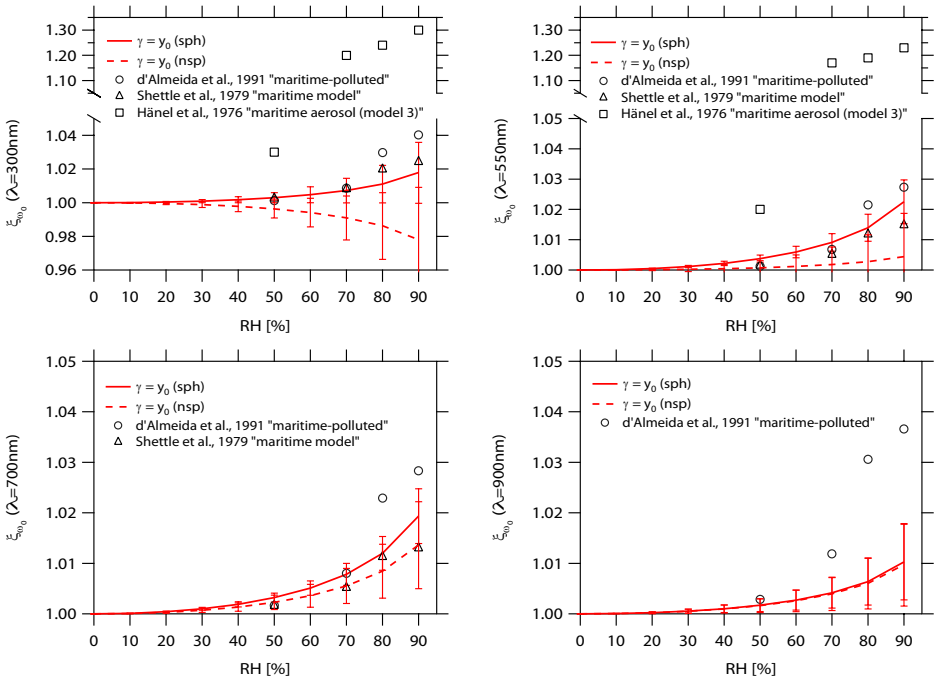

Figure 7.5: *Comparison of humidification factors for the single scattering albedo for the marine aerosol. Humidification factors from this investigation for spherical dust particles (red solid line) and non-spherical dust particles (red dashed line) are shown. The corresponding error bars result from the standard deviation of y_0. Additionally shown are humidification factors from D'Almeida et al. (1991) (hollow circles), from Shettle and Fenn (1979) (hollow triangles), and from Hänel (1976) (hollow squares).*

7.2 Parametrization of optical aerosol properties at dry conditions

In this section, time series of the dry single scattering albedo and the asymmetry parameter were parameterized according to the dry dust volume fraction (vf_{dust}, equation 5.1). The wavelength-dependent AOPs at dry state were already calculated in chapter 7.1 to determine the humidification factors of the AOPs. Figure A.7 and A.8 show scatter plots of the single scattering albedo versus vf_{dust} for spherical and non-spherical dust particles, respectively. The best fit to the data was achieved, using a power law:

$$\omega_0(\lambda) = C_1(\lambda) + C_2(\lambda) \cdot (1 - vf_{dust})^{C_3(\lambda)}. \tag{7.5}$$

The three free parameters $C_1(\lambda)$, $C_2(\lambda)$, and $C_3(\lambda)$ were determined for each wavelength using a nonlinear least-squares fit. The three fit parameters are summarized in Tables 7.5 and 7.6. From equation 7.5, the fit parameter C_1 equals the single scattering albedo for pure dust ($vf_{dust} = 1$). However, the pure dust single scattering albedo show large differences between spherical and non-spherical dust particles. The differences increases (up to $\approx 36\%$ at $\lambda = 300\,\text{nm}$) the smaller the wavelength, and the lower the single scattering albedo is. These discrepancies in ω_0 between non-spherical and spherical particle shape are much larger than the non-sphericity factors for the spheroids, deformed spheroids and aggregates (cf. Figure 5.14). There are two reasons for that. The revealed scattering non-sphericity factor from the data is larger than the scattering non-sphericity factor of the three shape classes. The influence of the scattering non-sphericity factor on the non-sphericity factor of the single scattering albedo increases, the lower the single scattering albedo is. This effect results from the particle non-sphericity and was also observed by Kalashnikova *et al.* (2005), who compared weakly absorbing dust (higher single scattering albedo) and strongly absorbing dust (lower single scattering albedo). To conclude, basically for single scattering albedos < 0.95 the effect of non-sphericity should be included in model calculations.
Literature values of ω_0 for pure Saharan dust were reported e.g., by Schladitz *et al.* (2009), Linke *et al.* (2006), Alfaro *et al.* (2004), Haywood *et al.* (2003), and Haywood *et al.* (2001). The single scattering albedo of pure dust ($vf_{dust} = 1$) are slightly lower than the values from Schladitz *et al.* (2009) during SAMUM-1. Schladitz *et al.* (2009) reported ω_0 values for high dust concentrations of about 0.96 ± 0.02 and 0.98 ± 0.01 at $\lambda = 537$ and 637 nm, respectively. A reason for these higher single scattering albedos are lower imaginary parts of the refractive index of mineral dust during SAMUM-1 as discussed in chapter 5.3.2. The dust origin during SAMUM-1 and SAMUM-2 was different and hence the single scattering albedos are necessarily not in agreement. Airborne measurements near the Cape Verde region determined by Haywood *et al.* (2001) revealed a Saharan dust single scattering albedo of 0.87 at 550 nm wavelength. Later, Haywood *et al.* (2003) reported a reassessment of this ω_0 value for Saharan dust from 0.87 to 0.94. The new ω_0 value fairly agrees with this investigation for pure Saharan dust ($\omega_0 = C_1$). Sun-photometer measurements during the SHADE

(Saharan Dust Experiment) field campaign, which took place at the Cape Verde Islands, yielded values for ω_0 of about 0.96 and 0.97 for 440 nm and 673 nm (Haywood *et al.*, 2003), respectively. Additionally, aircraft measurements were performed using a PSAP and a TSI integrating nephelometer. The derived ω_0 values range from 0.95 to 0.99 at $\lambda = 550$ nm . Laboratory measurements from dust samples of other Saharan dust sources, e.g., Nigerian and Tunisian dust revealed ω_0 values of 0.95±0.01 and 0.97±0.01 at 660 nm (Alfaro *et al.*, 2004). The single scattering albedo, e.g., from the Nigerian dust agree with this investigation, which can be interpreted as a hint for the influence of dust from these regions (cf. discussion of air mass origin in chapter 3).

Altough, the derived single scattering albedo of the marine (background) aerosol ($vf_{dust} = 0$) does not depend on the sphericity, the single scattering albedos for non-spherical (Figure 7.5) and spherical (Figure 7.6) dust particles are different. Therefore, the derived single scattering albedo of the marine aerosol should be used with caution, because it depends - especially for the lower wavelengths - strongly on the applied fit. Nevertheless, the derived ω_0 values are around 0.9 - 0.95 (derived from fit using non-spherical dust particles) and 0.95 - 0.98 (derived from fit using spherical dust particles) and show a slight wavelength dependence. For comparison, literature values from D'Almeida *et al.* (1991) and Shettle and Fenn (1979) for the same wavelength range are about 0.94 - 0.95 and 0.97 - 0.98, respectively. Figure A.9 shows a scatter plot of the dry asymmetry parameter versus vf_{dust}. The best fit to the data was achieved using the common power law:

$$g(\lambda) = B_1(\lambda) + B_2(\lambda) \cdot (vf_{dust})^{B_3(\lambda)} \tag{7.6}$$

The three fit parameters $B_1(\lambda)$, $B_2(\lambda)$, and $B_3(\lambda)$ were determined for each wavelength, and are summarized in Table 7.7. The fit parameter B_1 equals the asymmetry parameter for marine background ($vf_{dust} = 0$). The asymmetry parameter for pure dust was computed setting $vf_{dust} = 1$ in equation 7.6. Table 7.7 clarifies that the asymmetry parameter for pure dust is higher than for the marine (background) aerosol. This fact is not surprising, since the asymmetry parameter depends on the particle size. The aerosol model attributes the dust particles exclusively in the coarse particle mode, whereas the marine aerosol was attributed in the coarse mode as well as in the fine particle mode. The asymmetry parameters for the marine (background) aerosol and the pure dust increase from mid-visible to ultraviolet wavelengths. Other publications e.g., Sokolik and Toon (1999) and Otto *et al.* (2009) studying the asymmetry parameter of mineral dust, confirm this wavelength dependence. As aforementioned, the asymmetry parameter depends on the particle size, and therefore quantitative comparisons are omitted. It seems that the dust asymmetry parameters in Sokolik and Toon (1999) and Otto *et al.* (2009) are slightly higher than in this investigation. In particular, the values from Otto *et al.* (2009) are valid near the dust source region with a high concentration of large dust particles.

The asymmetry parameter of the marine (background) aerosol are around 0.7 and slightly higher than 0.67 - 0.69 found in D'Almeida *et al.* (1991) and Shettle and Fenn (1979). It

is difficult to perform a comparison for the asymmetry parameter of marine aerosol, since the sea-salt content is highly variable. It should be noted that the "error values" in Tables 7.5 - 7.7 are the error of the used fit with a confidence level of 66%.

Table 7.5: *Coefficients ± single standard deviation for the single scattering albedo for spherical dust particles at dry conditions. Values in brackets should be used with caution, because of uncertainties of the used fit (cf. Figure A.7).*

λ [nm]	$C_1 \equiv \omega_0$ ($vf_{dust} = 1$)	C_2	C_3	ω_0 ($vf_{dust} = 0$)
300	0.562±0.002	0.413±0.008	0.749±0.023	0.975±0.01
350	0.598±0.002	0.372±0.006	0.771±0.021	0.97±0.008
400	0.656±0.002	0.306±0.007	0.809±0.026	0.962±0.008
450	0.771±0.002	0.174±0.013	0.947±0.087	0.945±0.015
500	0.841±0.002	0.123±0.029	1.39±0.281	0.964±0.031
550	0.902±0.002	(0.055±0.126)	(2.5±2.88)	(0.956±0.128)
600	0.938±0.01	(-0.02±0.007)	(0.365±0.515)	(0.918±0.017)
650	0.958±0.011	(-0.031±0.007)	(0.345±0.313)	(0.927±0.018)
700	0.963±0.009	(-0.033±0.006)	(0.388±0.295)	(0.93±0.015)
750	0.968±0.007	(-0.035±0.006)	(0.418±0.276)	(0.934±0.013)
800	0.971±0.007	(-0.033±0.005)	(0.413±0.275)	(0.938±0.013)
850	0.973±0.007	(-0.034±0.005)	(0.426±0.268)	(0.94±0.012)
900	0.976±0.006	(-0.032±0.005)	(0.44±0.266)	(0.944±0.011)
950	0.976±0.006	(-0.031±0.005)	(0.431±0.268)	(0.945±0.011)

Table 7.6: *Coefficients ± single standard deviation for the single scattering albedo for non-spherical dust particles at dry conditions. For the wavelengths from 450 - 550 nm, the C_3 parameter was set to unity, to obtain a linear relationship.*

λ [nm]	$C_1 \equiv \omega_0$ ($vf_{dust} = 1$)	C_2	C_3	ω_0 ($vf_{dust} = 0$)
300	0.765±0.001	0.158±0.007	1.08±0.052	0.923±0.008
350	0.773±0.001	0.152±0.008	1.064±0.065	0.925±0.01
400	0.8±0.001	0.129±0.012	1.124±0.111	0.928±0.014
450	0.863±0.001	0.038±0.006	1±0	0.902±0.008
500	0.901±0.002	0.003±0.007	1±0	0.904±0.008
550	0.938±0.002	-0.031±0.007	1±0	0.907±0.008
600	0.96±0.005	-0.033±0.006	0.524±0.274	0.926±0.011
650	0.969±0.004	-0.038±0.006	0.559±0.249	0.932±0.01
700	0.971±0.004	-0.037±0.006	0.55±0.25	0.934±0.01
750	0.974±0.004	-0.037±0.006	0.538±0.245	0.937±0.01
800	0.975±0.005	-0.035±0.006	0.507±0.252	0.94±0.01
850	0.976±0.005	-0.034±0.005	0.487±0.251	0.942±0.01
900	0.977±0.005	-0.032±0.005	0.471±0.258	0.945±0.01
950	0.977±0.006	-0.031±0.005	0.442±0.265	0.945±0.011

Table 7.7: *Coefficients ± single standard deviation for the asymmetry parameter at dry conditions. For the wavelengths from 500 - 950 nm, the B_3 parameter was set to unity, to obtain a linear relationship.*

λ [nm]	$B_1 \equiv g\,(vf_{dust} = 0)$	B_2	B_3	$g\,(vf_{dust} = 1)$
300	0.745±0.004	0.127±0.004	4.153±0.3	0.872±0.007
350	0.726±0.004	0.116±0.004	3.57±0.27	0.842±0.008
400	0.699±0.005	0.104±0.005	2.789±0.273	0.803±0.01
450	0.676±0.013	0.072±0.012	1.684±0.457	0.748±0.025
500	0.64±0.003	0.08±0.003	1±0	0.72±0.006
550	0.656±0.003	0.053±0.003	1±0	0.709±0.005
600	0.643±0.002	0.042±0.003	1±0	0.684±0.005
650	0.647±0.002	0.049±0.003	1±0	0.696±0.005
700	0.637±0.002	0.044±0.003	1±0	0.681±0.005
750	0.65±0.003	0.048±0.003	1±0	0.698±0.006
800	0.635±0.002	0.049±0.003	1±0	0.684±0.005
850	0.641±0.002	0.05±0.003	1±0	0.69±0.005
900	0.644±0.002	0.048±0.003	1±0	0.693±0.005
950	0.636±0.002	0.048±0.003	1±0	0.684±0.005

8 Summary and Outlook

8.1 Summary

Humidity effects of optical aerosol properties of mixed aerosol species are presently a gap in knowledge. The present PhD-thesis delivers a comprehensive quantification of wavelength-dependent humidity effects of aerosol optical properties of a mixture of marine aerosol and Saharan mineral dust. The experimental basis for this work are measurements of microphysical and optical particle properties at Cape Verde Islands in the framework of the Saharan Mineral Dust Experiment (SAMUM). The measurements took place in January and February 2008, with highest occurrence of dust plumes from the Saharan desert.
During the measurement campaign dry particle number size distributions were measured with mobility and aerodynamic size spectrometers. Hygroscopic growth factors and the state of mixing were determined with humidified mobility and aerodynamic size spectrometers as well as with the tandem differential mobility analyzer technique. Optical properties in terms of light scattering and absorption were measured with nephelometry and filter-based absorption photometry at dry conditions. These measurements served as a basis for the aerosol model, which is a central point of this work.
The goal of the aerosol model was to reproduce the measured aerosol optical and microphysical properties and to predict aerosol optical and microphysical properties at ambient conditions by a few numbers of parameters. The measured particle number size distributions were parameterized by four lognormal size distributions. The Aitken and accumulation mode particles were mainly attributed to the marine aerosol, while coarse mode particles were composed of sea-salt and Saharan mineral dust. A new methodical approach was used to derive the mean hygroscopic growth factors and mixing state in almost the full particle size range from 26 nanometers to 10 micrometers. Hygroscopic growth and mixing state information in this size range are a requirement to predict optical properties (of the particle ensemble) at ambient conditions. The state of mixing in terms of hygroscopicity shows a clear distinction into hygroscopic and hydrophobic particles. From the growth measurements, mean hygroscopic growth factors for the hydrophobic and hygroscopic particles were derived. The measured mean hygroscopic growth factors at a certain relative humidity were parameterized with the common single hygroscopicity parameter κ to extrapolate the mean hygroscopic growth factors in the relative humidity range from 0 - 90%. For hygroscopic particles, κ is nearly constant for particles smaller 100 nm with a median around 0.35. For particles in the size range from 100 nm to 350 nm κ increases up to 0.65. For larger parti-

cles, time-dependent κ parameters at 350 nm were used. For hydrophobic particles, κ varies between 0 and 0.1 in the size range up to 250 nm. For larger particles, κ decreases towards 0.

With the information on hygroscopic mixing state, the lognormal size distributions, and the mineralogical particle analysis, a chemical classification of the particles was possible. According to the chemical composition, a dry density of $1700\,\mathrm{kg\,m^{-3}}$, $2170\,\mathrm{kg\,m^{-3}}$, and $2700\,\mathrm{kg\,m^{-3}}$ was assigned to the fine mode, the hygroscopic particles of the coarse mode, and the hydrophobic particles of the coarse mode, respectively.

As a first guess, literature values of complex refractive indices were used to represent optical properties in dependence of the lognormal size distribution and the hygroscopic mixing state. Complex refractive indices of "sea-salt (0% RH)" and "mineral transported" were assigned to the hygroscopic and hydrophobic particles of the coarse mode, respectively. The complex refractive index for the fine mode was calculated by using an internal mixture of "soot" and "insoluble" for the hydrophobic particles, and "soot" and "water soluble (0% RH)" for the hygroscopic particles.

Using the lognormal size distributions and the complex refractive indices, Mie-calculated optical properties were compared with measured optical properties at dry conditions. An intercomparison of measured and calculated scattering coefficients showed that the calculations underestimate the scattering coefficient at higher mineral dust concentrations. From measured and calculated scattering, a wavelength-dependent scattering non-sphericity factor was derived. In a laboratory study, this non-sphericity factor was quantitatively confirmed. Similar to the scattering coefficient, the absorption coefficients were compared at dry conditions. This closure revealed that the calculations underestimate the absorption coefficients for wavelengths smaller 550 nm and overestimate the absorption coefficients for wavelengths larger 550 nm. This effect was mainly caused by a different imaginary part of the complex refractive index for mineral dust. Thus, a new (optical equivalent) imaginary part of mineral dust was retrieved applying Mie calculations. At this stage, the aerosol model was adapted to the measured optical properties at dry conditions.

The aerosol model was validated with measured mass concentrations and extinction coefficients at ambient conditions. Intercomparison studies at ambient conditions revealed that the aerosol model is able to reproduce the effect of hygroscopic growth to the extinction coefficient and reproduce quantitatively the measured particle mass concentration. Both studies demonstrate the importance of hygroscopic growth of coarse mode sea-salt particles for relative humidities below 90%. It was shown that the aerosol model was deployed to calculate the extinction coefficients in the lowermost layers of the atmosphere up to a height of about 200 m to extend measured lidar profiles to the ground. A complete vertical profile of the extinction coefficient from the ground to the uppermost aerosol layers is necessary, when comparing column integrated aerosol optical thickness with measured aerosol optical thickness from sun-photometer.

Time series of optical properties (absorption, scattering, and extinction coefficients as well

as single scattering albedo, and asymmetry parameter) were derived at the dry state and at relative humidities of 55%, 75%, and 90% in a wavelength range from 300 to 950 nm by using the aerosol model. From these time series, humidification factors for the given relative humidities, wavelength range and aerosol optical properties were calculated. Following the common literature, the humidification factors were parameterized by a power law. From this single parameter power law, a time series of a parameter γ was derived, which depends solely on the aerosol optical property and wavelength. It was found that the parameter γ depends on the dry dust volume fraction. Hence, γ was in turn parameterized by three parameters using a power law formalism. The parameterization was extended to describe the humidity dependence of optical properties of clean marine aerosol. The humidification factors from the parameterization agreed within the literature values of the marine aerosol. In summary, with known relative humidity, wavelength and dry dust volume fraction, the humidity dependence of optical properties can be calculated from the tabulated three parameters.

The derived parameterization is a powerful tool and can be applied to calculate the humidity dependence from the dry state up to 90% RH for regions of pure Saharan dust, regions with influence of marine and Saharan dust, and regions of pure marine aerosol. However, the parameterization is only valid for particles being in a metastable equilibrium with the surrounding moist air.

Dry optical properties in terms of the single scattering albedo and the asymmetry parameter were parameterized using a power law. The parameterization was done using spherical and non-spherical dust particles. The power law is a function of the dry dust volume fraction and includes three parameters. The pure dust case is described by one of the three parameters. The single scattering albedo differs between the spherical and non-spherical dust case and the non-sphericity factor of the pure dust single scattering albedo increases with decreasing wavelength. These non-sphericity factors are much larger than predicted in literature using modelled non-spherical particle shapes. It was found that for single scattering albedos smaller 0.95, the non-sphericity effect plays an important role.

With regard to radiative transfer calculations, the role of hygroscopic growth is insufficiently considered. The present PhD-thesis delivers a simple parameterization to transform optical properties from dry state to ambient conditions. Therefore, the parameterization can be applied to radiative transfer calculations using realistic optical aerosol properties at the present ambient conditions. Beyond that, current radiative transfer models mainly based on Mie calculations. Under certain conditions, e.g., high dust concentrations and therefore a large number of non-spherical particles, the Mie approach lead to incorrect aerosol optical properties and hence incorrect radiative transfer calculations.

8.2 Outlook

The modelling of non-spherical particles, whose optical properties reproduce the measured optical properties, should be therefore one goal of future work. The question is actually unanswered, if there exist a connection between microphysical properties of non-spherical particles (e.g., dynamic shape factor) and optical properties of non-spherical particles (non-sphericity factor). Considering the measurement technique of this work for future studies, the direct measurement of the hygroscopic growth factor for supermicrometer particles is necessary. Furthermore, to obtain the mixing state in a much simpler way as described in the PhD-thesis, the HAPS and the HDMPS should simultaneously measure the humidified particle number size distribution at the same relative humidity. The expansion of the measurement devices by an aerosol polar nephelometer would lead to deeper insight in the scattering behavior of non-spherical particles. For example, an intercomparison of a polar nephelometer and an integrating nephelometer can be done, and the scattering phase function of the polar nephelometer can be compared with results from modelled non-spherical particles.

A Illustration of fitted power functions

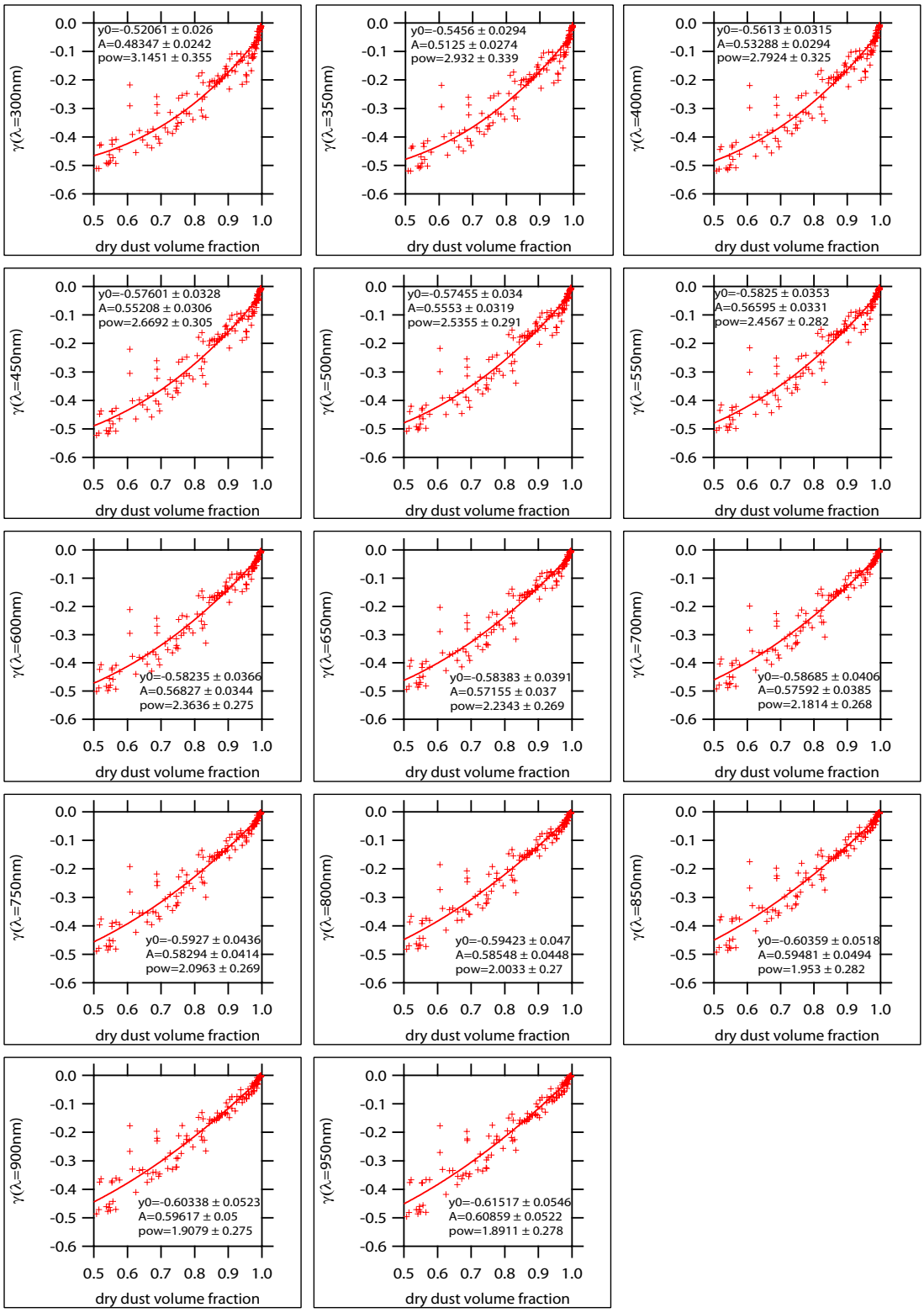

Figure A.1: *Fitted γ parameters (equation 7.2) for the humidification factor of the extinction coefficient (spherical dust particles) versus dry dust volume fraction for wavelengths from 300 - 950 nm. Shown are the respective fit parameters ± single standard deviation of y_0, A, and pow applying equation 7.4.*

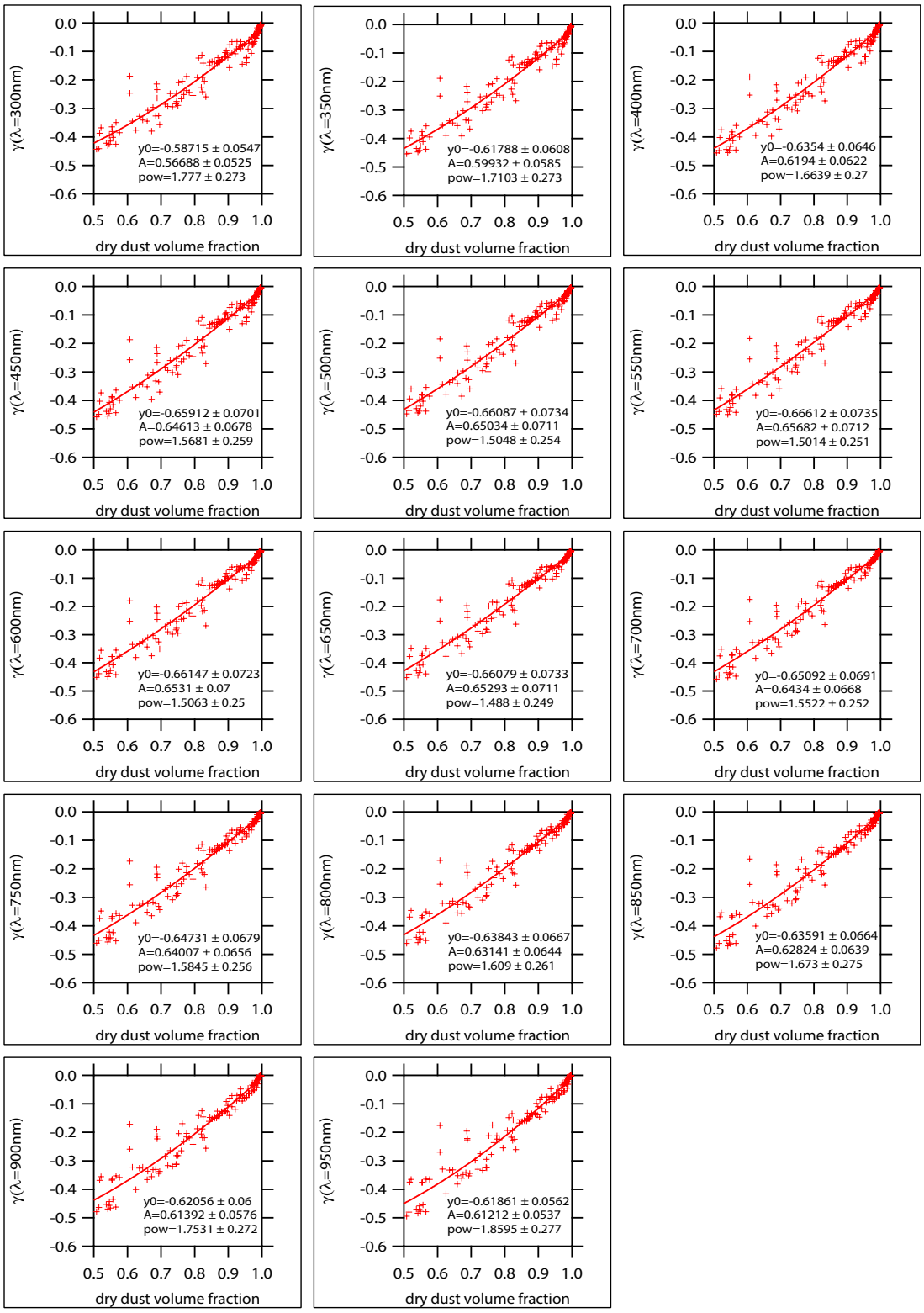

Figure A.2: *Fitted γ parameters (equation 7.2) for the humidification factor of the extinction coefficient (non-spherical dust particles) versus dry dust volume fraction for wavelengths from 300 - 950 nm. Shown are the respective fit parameters ± single standard deviation of y_0, A, and pow applying equation 7.4.*

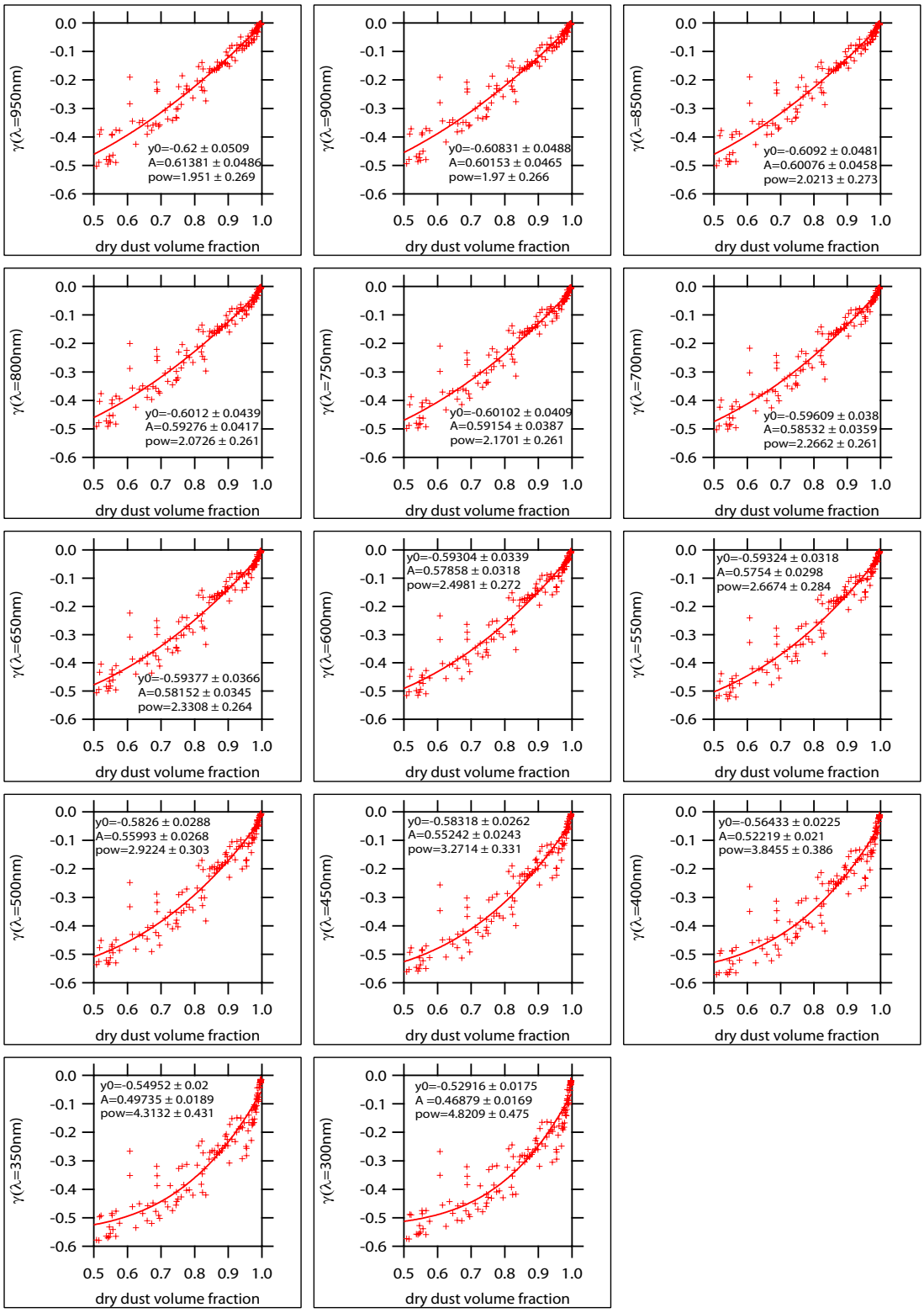

Figure A.3: *Fitted γ parameters (equation 7.2) for the humidification factor of the scattering coefficient (spherical dust particles) versus dry dust volume fraction for wavelengths from 300 - 950 nm. Shown are the respective fit parameters ± single standard deviation of y_0, A, and pow applying equation 7.4.*

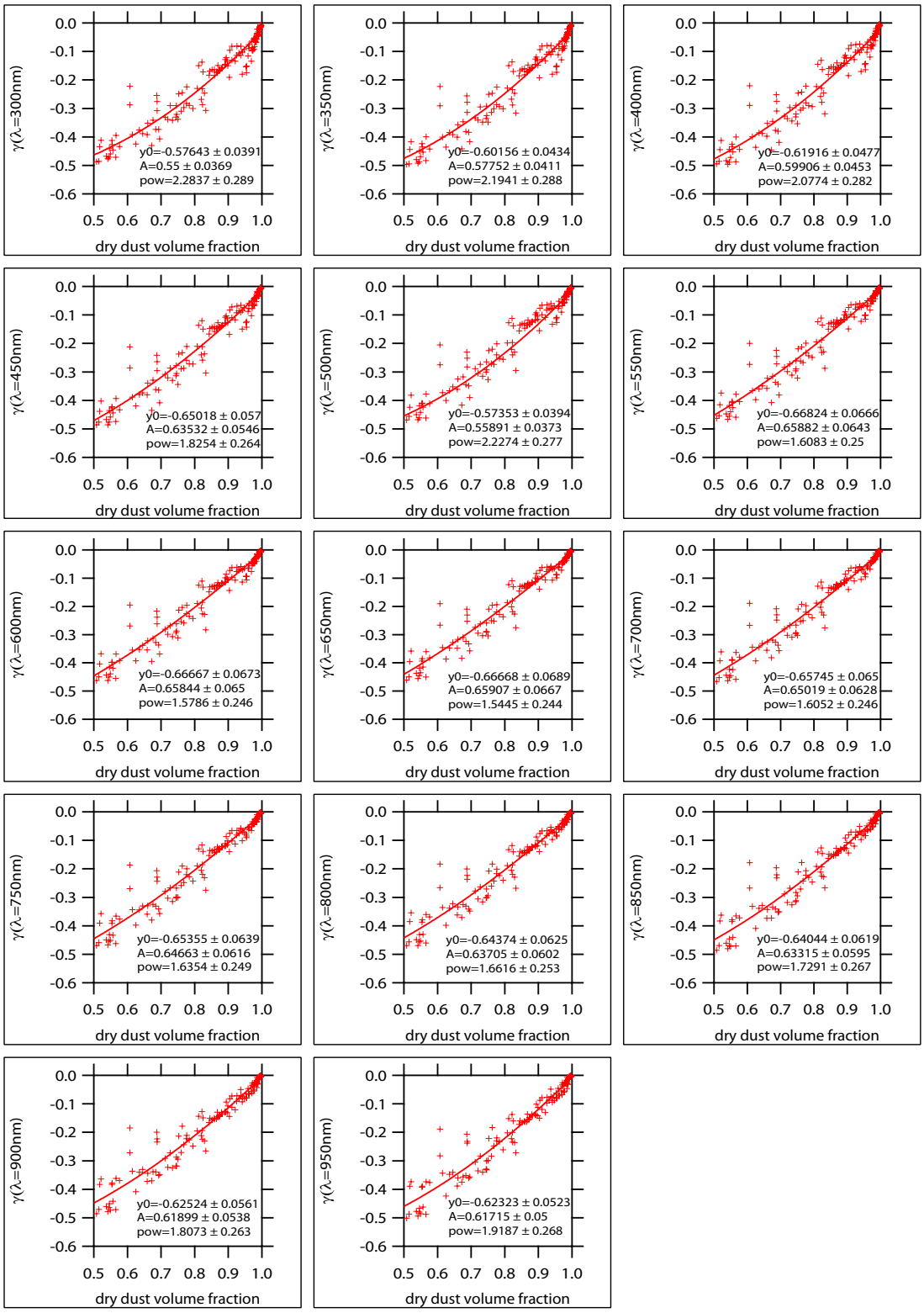

Figure A.4: *Fitted γ parameters (equation 7.2) for the humidification factor of the scattering coefficient (non-spherical dust particles) versus dry dust volume fraction for wavelengths from 300 - 950 nm. Shown are the respective fit parameters ± single standard deviation of y_0, A, and pow applying equation 7.4.*

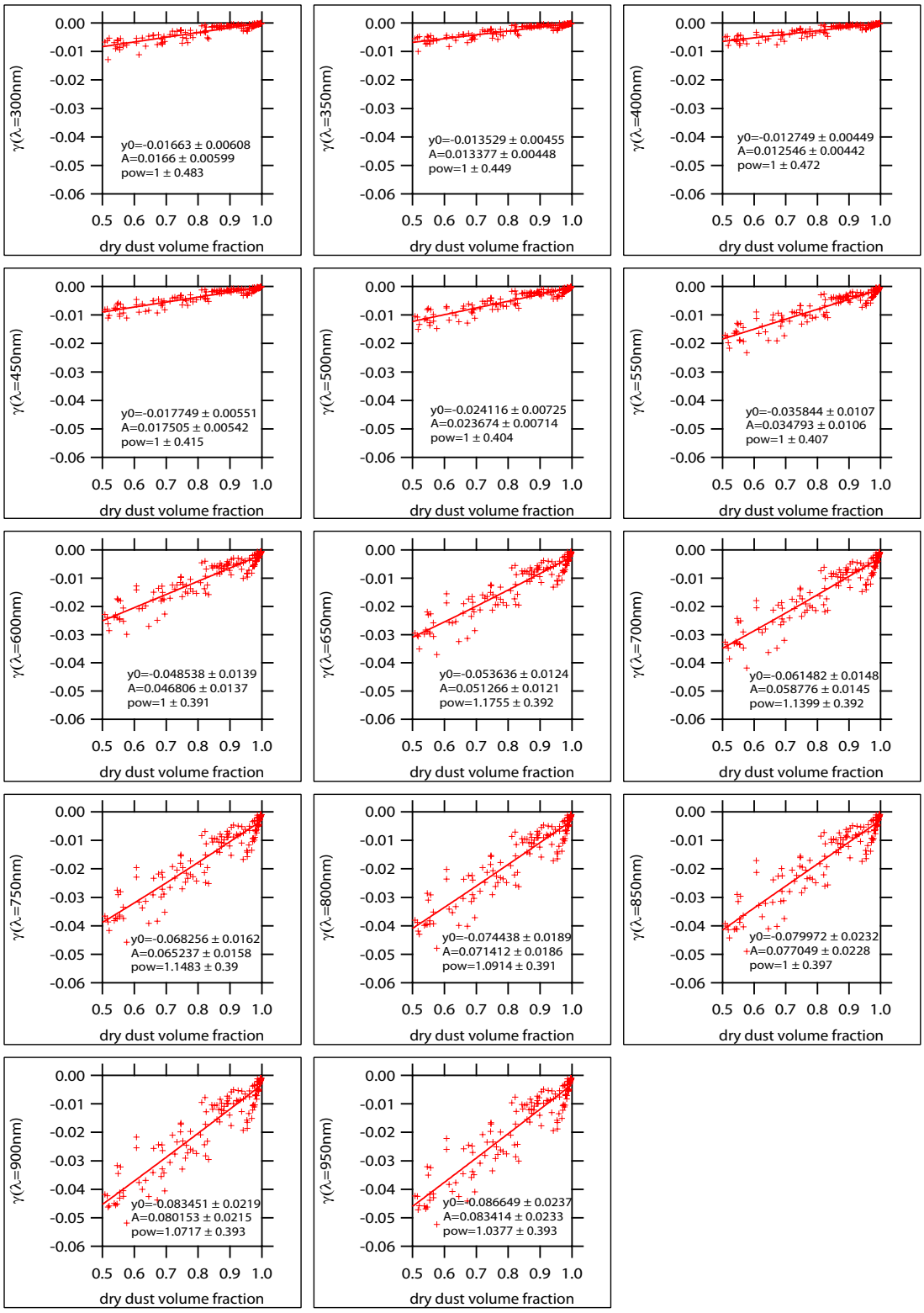

Figure A.5: *Fitted γ parameters (equation 7.2) for the humidification factor of the absorption coefficient versus dry dust volume fraction for wavelengths from 300 - 950 nm. Shown are the respective fit parameters ± single standard deviation of y_0, A, and pow applying equation 7.4.*

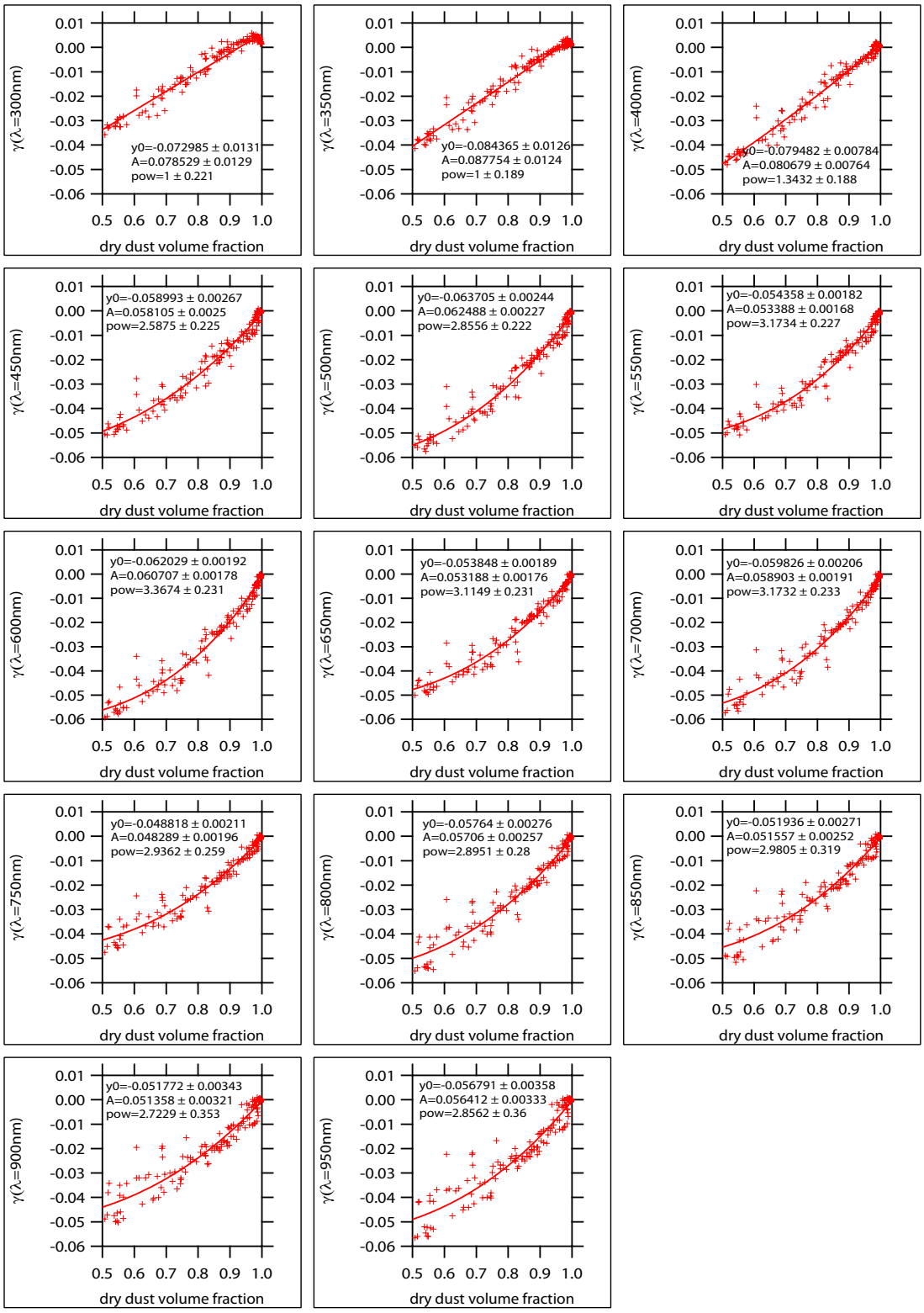

Figure A.6: *Fitted γ parameters (equation 7.2) for the humidification factor of the asymmetry parameter versus dry dust volume fraction for wavelengths from 300 - 950 nm. Shown are the respective fit parameters $\pm$ single standard deviation of y_0, A, and pow applying equation 7.4.*

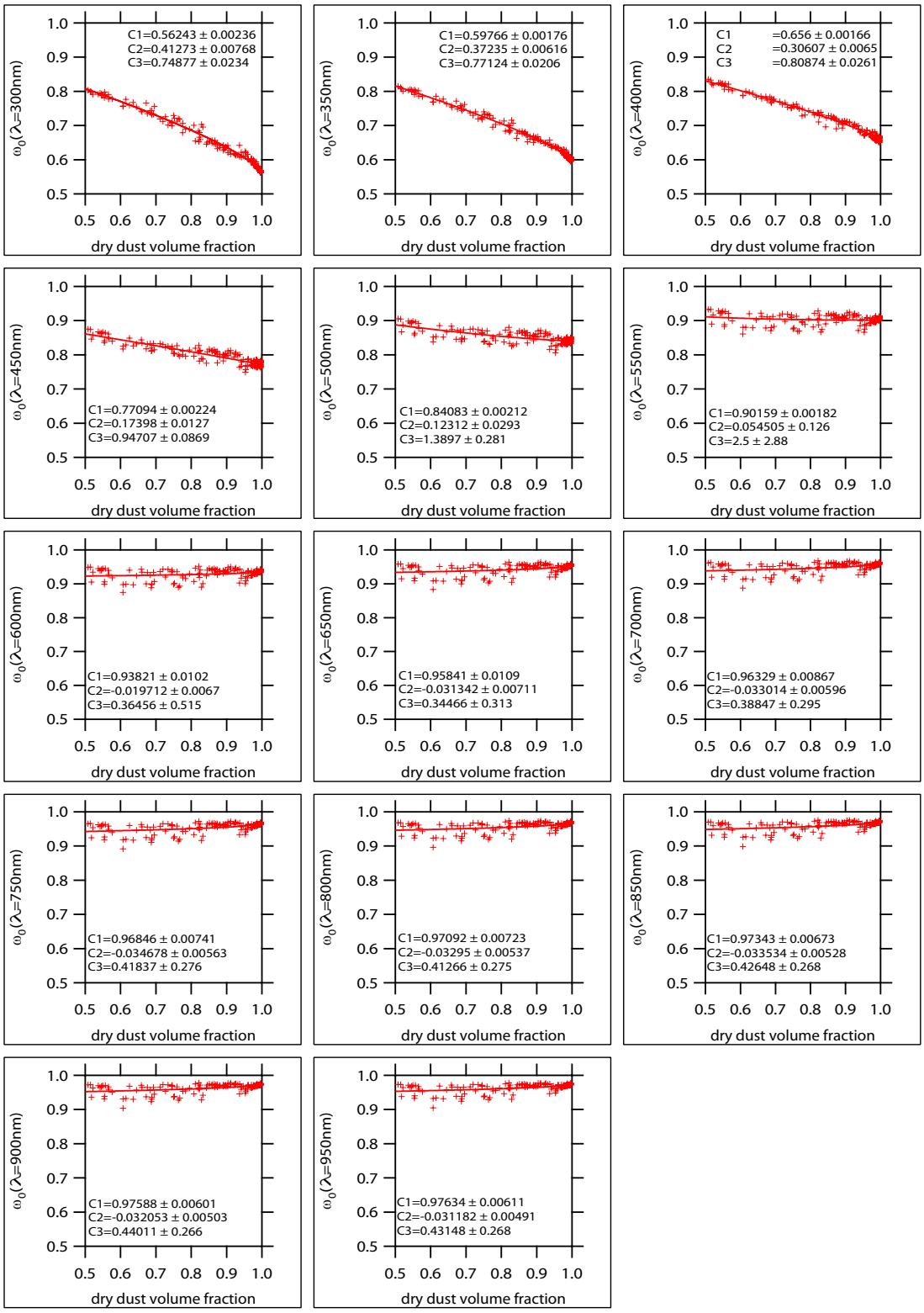

Figure A.7: *Fitted single scattering albedo (spherical dust particles) versus dry dust volume fraction for wavelengths from 300 - 950 nm. Shown are the respective fit parameters ± single standard deviation of C_1, C_2, and C_3 applying equation 7.5.*

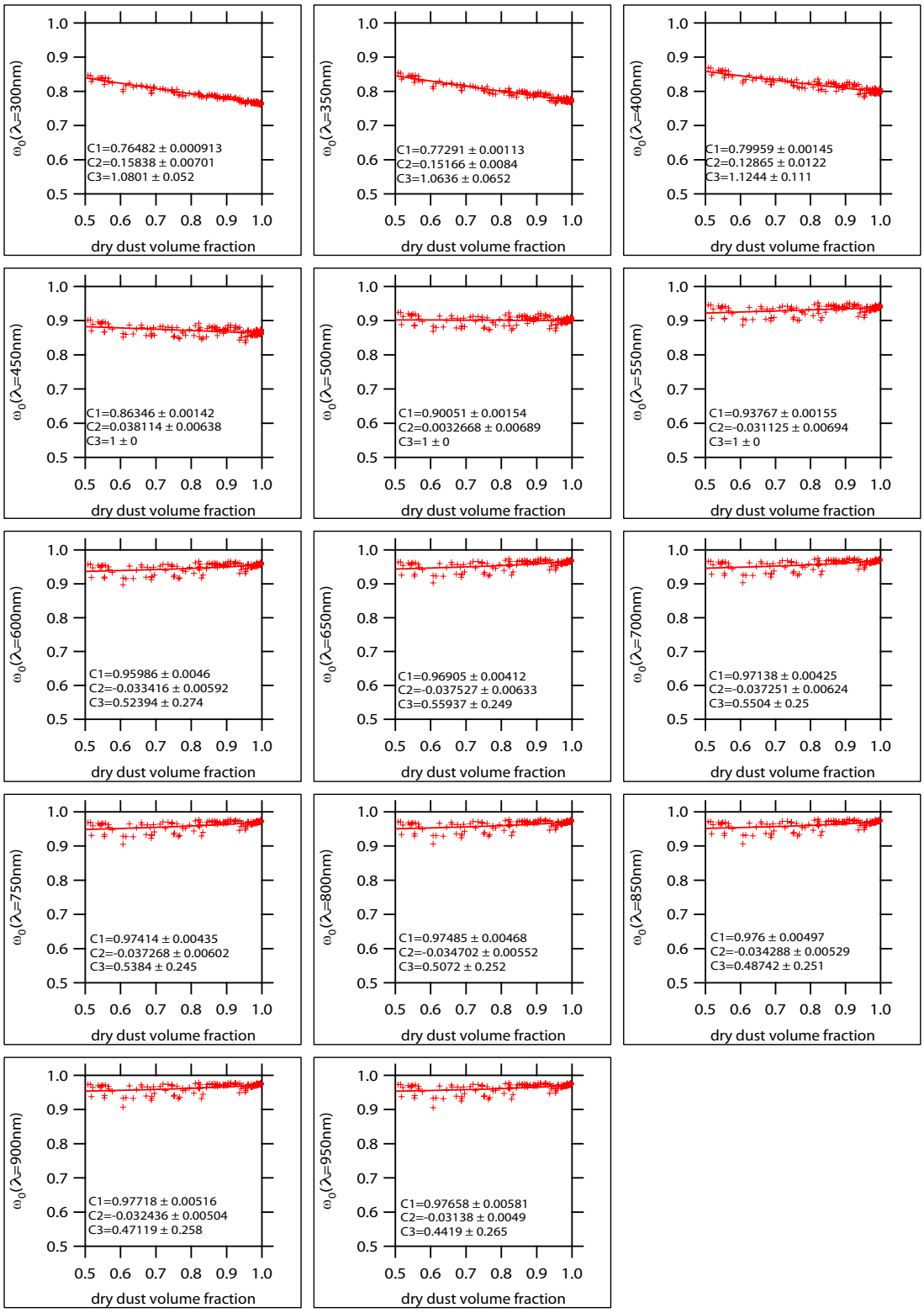

Figure A.8: *Fitted single scattering albedo (non-spherical dust particles) versus dry dust volume fraction for wavelengths from 300 - 950 nm. Shown are the respective fit parameters ± single standard deviation of C_1, C_2, and C_3 applying equation 7.5.*

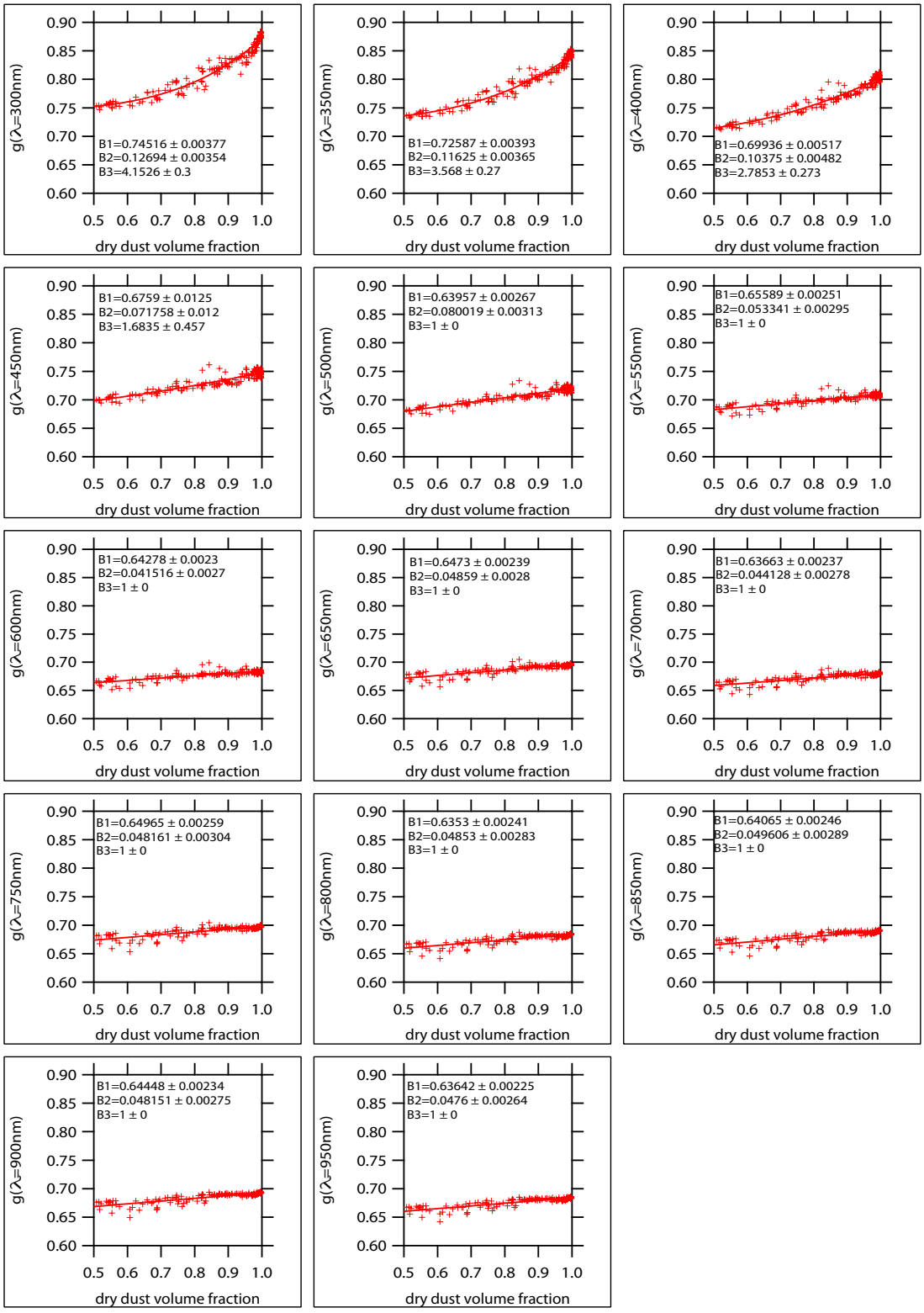

Figure A.9: *Fitted asymmetry parameter versus dry dust volume fraction for wavelengths from 300 - 950 nm. Shown are the respective fit parameters ± single standard deviation of B_1, B_2, and B_3 applying equation 7.6.*

Bibliography

Achtert, P., Birmili, W., Nowak, A., Wehner, B., Wiedensohler, A., Takegawa, N., Kondo, Y., Miyazaki, Y., Hu, M., and Zhu, T. (2009). Hygroscopic growth of tropospheric particle number size distributions over the North China Plain. *J. Geophys. Res.*, **114**(D2), D00G07. 37

Alfaro, S. C., Lafon, S., Rajot, J. L., Formenti, P., Gaudichet, A., and Maillé, M. (2004). Iron oxides and light absorption by pure desert dust: An experimental study. *J. Geophys. Res.*, **109**(D08208). 90, 91

Anderson, T. L. and Ogren, J. A. (1998). Determining Aerosol Radiative Properties Using the TSI 3563 Integrating Nephelometer. *Aerosol Sci. Technol.*, **29**(1), 57–69. 46

Anderson, T. L., Covert, D. S., Marshall, S. F., Laucks, M. L., Charlson, R. J., Waggoner, A. P., Ogren, J. A., Caldow, R., Holm, R. L., Quant, F. R., Sem, G. J., Wiedensohler, A., Ahlquist, N. A., and Bates, T. S. (1996). Performance Characteristics of a High-Sensitivity, Three-Wavelength, Total Scatter/Backscatter Nephelometer. *J. Atmos. Oceanic Technol.*, **13**(5), 967–986. 45, 59

Anderson, T. L., Masonis, S. J., Covert, D. S., Ahlquist, N. C., Howell, S. G., Clarke, A. D., and McNaughton, C. S. (2003). Variability of aerosol optical properties derived from in situ aircraft measurements during ACE-Asia. *J. Geophys. Res*, **108**(D23), 8647. 3, 82, 84

Andreae, M. O. (1995). Climatic effects of changing atmospheric aerosol levels. In A. Henderson-Sellers, editor, *Future climates of the world: A modelling perspective*, World survey of climatology, pages 347–398. Elsevier, Amsterdam. 2

Andreae, M. O. and Gelencsér, A. (2006). Black carbon or brown carbon? the nature of light-absorbing carbonaceous aerosols. *Atmos. Chem. Phys.*, **6**(10), 3131–3148. 48

Angström, A. (1929). On the Atmospheric Transmission of Sun Radiation and on Dust in the Air. *Geografiska Annaler*, **11**, 156–166. 10

Bergstrom, R. W., Russell, P. B., and Hignett, P. (2002). Wavelength Dependence of the Absorption of Black Carbon Particles: Predictions and Results from the TARFOX Experiment and Implications for the Aerosol Single Scattering Albedo. *J. Atmos. Sci.*, **59**(3), 567–577. 10, 65

Bi, L., Yang, P., Kattawar, G. W., and Kahn, R. (2010). Modeling optical properties of mineral aerosol particles by using nonsymmetric hexahedra. *Appl. Opt.*, **49**(3), 334–342. 68

Birmili, W. (1998). *Production of new ultrafine particles in continental air masses*. PhD-thesis, University of Leipzig, Germany. 26, 54

Birmili, W., Stratmann, F., Wiedensohler, A., Covert, D., Russell, L. M., and Berg, O. (1997). Determination of Differential Mobility Analyzer Transfer Functions Using Identical Instruments in Series. *Aerosol Sci. Technol.*, **27**(2), 215–223. 26

Birmili, W., Stratmann, F., and Wiedensohler, A. (1999). Design of a DMA-based size spectrometer for a large particle size range and stable operation. *J. Aerosol Sci.*, **30**(4), 549–553. 26

Birmili, W., Nowak, A., and Schwirn, K. (2004). A new method to accurately relate dry and humidified size distributions of atmospheric aerosols. In *European Aerosol Conference*, volume 35, Supplement 1, pages 15–16, Budapest. J. Aerosol Sci. 37

Birmili, W., Schepanski, K., Ansmann, A., Spindler, G., Tegen, I., Wehner, B., Nowak, A., Reimer, E., Mattis, I., Müller, K., Brüggemann, E., Gnauk, T., Herrmann, H., Wiedensohler, A., Althausen, D., Schladitz, A., Tuch, T., and Löschau, G. (2008). A case of extreme particulate matter concentrations over Central Europe caused by dust emitted over the southern Ukraine. *Atmos. Chem. Phys.*, **8**, 997–1016. 29

Birmili, W., Schwirn, K., Nowak, A., Petäjä, T., Joutsensaari, J., Rose, D., Wiedensohler, A., Hämeri, K., Aalto, P., Kulmala, M., and Boy, M. (2009). Measurements of humidified particle number size distributions in a Finnish boreal forest: derivation of hygroscopic particle growth factors. *Boreal Env. Res.*, **14**, 458–480. 30, 37

Bohren, C. F. and Huffman, D. R. (1983). *Absorption and Scattering of Light by Small Particles*. John Wiley & Sons, Inc., New York. 7, 8, 74

Bond, T. C. and Bergstrom, R. W. (2006). Light Absorption by Carbonaceous Particles: An Investigative Review. *Aerosol Sci. Technol.*, **40**, 27–67. 65

Bond, T. C., Anderson, T. L., and Campbell, D. (1999). Calibration and Intercomparison of Filter-Based Measurements of Visible Light Absorption by Aerosols. *Aerosol Sci. Technol.*, **30**, 582–600. 47, 48

Bond, T. C., Covert, D. S., and Müller, T. (2009). Truncation and Angular-Scattering Corrections for Absorbing Aerosol in the TSI 3563 Nephelometer. *Aerosol Sci. Technol.*, **43**(9), 866–871. 46

Brockmann, J. E. (1993). Sampling and Transport of Aerosols. In K. Willeke and P. Baron, editors, *Aerosol Measurement - Principles, Techniques, and Applications*, pages 77–108. Van Nostrand Reinhold, New York. 74

Carrico, C. M., Rood, M. J., and Ogren, J. A. (1998). Aerosol light scattering properties at Cape Grim, Tasmania, during the First Aerosol Characterization Experiment (ACE 1). *J. Geophys. Res.*, **103**(D13), 16565–16574. 3, 84

Carrico, C. M., Rood, M. J., Ogren, J. A., Neusüß, C., Wiedensohler, A., and Heintzenberg, J. (2000). Aerosol Optical properties at Sagres, Portugal during ACE 2. *Tellus*, **52B**(2), 694–715. 3

Carrico, C. M., Kus, P., Rood, M. J., Quinn, P. K., and Bates, T. S. (2003). Mixtures of pollution, dust, sea salt, and volcanic aerosol during ACE-Asia: Radiative properties as a function of relative humidity. *J. Geophys. Res.*, **108**(D23), 8650. 3, 82, 84

Charlson, R. J., Covert, D. S., and Larson, T. B. (1984). Observation of the effect of humidity on light scattering by aerosols. In L. Ruhnke and A. Deepak, editors, *Hygroscopic Aerosols*, pages 35–44. A. Deepak, Hampton, VA. 82

Cheng, Y. F., Eichler, H., Wiedensohler, A., Heintzenberg, J., Zhang, Y. H., Hu, M., Herrmann, H., Zeng, L. M., Liu, S., Gnauk, T., Brüggemann, E., and He, L. Y. (2006). Mixing state of elemental carbon and non-light-absorbing aerosol components derived from in situ particle optical properties at Xinken in Pearl River Delta of China. *J. Geophys. Res.*, **111**, D20204. 57, 66

Cheng, Y. F., Wiedensohler, A., Eichler, H., Heintzenberg, J., Tesche, M., Ansmann, A., Wendisch, M., Su, H., Althausen, D., Herrmann, H., Gnauk, T., Brüggemann, E., Hu, M., and Zhang, Y. H. (2008). Relative humidity dependence of aerosol optical properties and direct radiative forcing in the surface boundary layer at Xinken in Pearl River Delta of China: An observation based numerical study. *Atmos. Environ.*, **42**(25), 6373–6397. 82, 83

Chiapello, I., Bergametti, G., Gomes, L., Chatenet, B., Dulac, F., Pimenta, J., and Santos Soares, E. (1995). An additional low layer transport of Sahelian and Saharan dust over the North-Eastern Tropical Atlantic. *Geophys. Res. Lett.*, **22**(23), 3191–3194. 4

Chiapello, I., Bergametti, G., Chatenet, B., Bousquet, P., Dulac, F., and Santos Soares, E. (1997). Origins of African dust transported over the northeastern tropical Atlantic. *J. Geophys. Res.*, **102**(D12), 13701–13709. 4

Covert, D. S., Charlson, R. J., and Ahlquist, N. C. (1972). A study of the Relationship of Chemical Composition and Humidity to Light Scattering by Aerosols. *J. Appl. Meteor.*, **11**(6), 968–976. 3, 84

D'Almeida, G. A., Koepke, P., and Shettle, E. P. (1991). *Atmospheric aerosols: Global climatology and radiative characteristics*. Deepak, Hampton, Va. VI, VII, 3, 58, 84, 87, 88, 89, 91

DeCarlo, P. F., Slowik, J. G., Worsnop, D. R., Davidovits, P., and Jimenez, J. L. (2004). Particle Morphology and Density Characterization by Combined Mobility and Aerodynamic Diameter Measurements. Part 1: Theory. *Aerosol Sci. Technol.*, **38**(12), 1185–1205. 28

Duplissy, J., Gysel, M., Sjogren, S., Meyer, N., Good, N., Kammermann, L., Michaud, V., Weigel, R., Martins dos Santos, S., Gruening, C., Villani, P., Laj, P., Sellegri, K., Metzger, A., McFiggans, G. B., Wehrle, G., Richter, R., Dommen, J., Ristovski, Z., Baltensperger, U., and Weingartner, E. (2009). Intercomparison study of six HTDMAs: results and recommendations. *Atmos. Meas. Tech.*, **2**, 363–378. 35

Eichler, H., Cheng, Y. F., Birmili, W., Nowak, A., Wiedensohler, A., Brüggemann, E., Gnauk, T., Herrmann, H., Althausen, D., Ansmann, A., Engelmann, R., Tesche, M., Wendisch, M., Zhang, Y. H., Hu, M., Liu, S., and Zeng, L. M. (2008). Hygroscopic properties and extinction of aerosol particles at ambient relative humidity in South-Eastern China. *Atmos. Environ.*, **42**(25), 6321–6334. 37

Engelstaedter, S., Tegen, I., and Washington, R. (2006). North african dust emissions and transport. *Earth-Sci. Rev.*, **79**, 73–100. 4, 18

Fernald, F. G. (1984). Analysis of atmospheric lidar observations: some comments. *Appl. Opt.*, **23**(5), 652–653. 79

Fitzgerald, J. W. (1991). Marine aerosols: A review. *Atmos. Environ.*, **25**(3-4), 533–545. 52, 53, 54

Forster, P., Ramaswamy, V., Artaxo, P., Berntsen, T., Betts, R., Fahey, D., Haywood, J., Lean, J., Lowe, D., Myhre, G., Ngana, J., Prinn, R., Raga, G., Schulz, M., and van Dorland, R. (2007). Changes in Atmospheric Constituents and in Radiative Forcing. In S. Solomon, D. Qin, M. Manning, Z. Chen, M. Marquis, K. Averyt, M. Tignor, and H. Miller, editors, *Climate Change 2007: The Physical Science Basis. Contribution of Working Group I to the Fourth Assessment Report of the Intergovernmental Panel on Climate Change*. Cambridge University Press, Cambridge, United Kingdom and New York, USA. 2, 3

Freudenthaler, V., Esselborn, M., Wiegner, M., Heese, B., Tesche, M., Ansmann, A., Müller, D., Althausen, D., Wirth, M., Fix, A., Ehret, G., Knippertz, P., Toledano, C., Gasteiger, J., Garhammer, M., and Seefeldner, M. (2009). Depolarization ratio profiling at several wavelengths in pure Saharan dust during SAMUM 2006. *Tellus*, **61B**(1), 165–179. 79

Gasteiger, J., Wiegner, M., Toledano, C., Groß, S., Freudenthaler, V., Tesche, M., and Kandler, K. (2011). Modeling optical properties of complex mineral dust aerosols and comparison with SAMUM lidar and Sun photometer measurements. *submitted to Tellus*, **63B**. 68, 69

Grant, K. E., Chuang, C. C., Grossman, A. S., and Penner, J. E. (1999). Modeling the spectral optical properties of ammonium sulfate and biomass burning aerosols: parameterization of relative humidity effects and model results. *Atmos. Environ.*, **33**(17), 2603–2620. 82

Gras, J. L. and Ayers, G. P. (1983). Marine Aerosol at Southern Mid-Latitudes. *J. Geophys. Res.*, **88**(10), 10661–10666. 53

Groß, S., Gasteiger, J., Freudenthaler, V., Wiegner, M., Geiß, A., Schladitz, A., Toledano, C., Kandler, K., Tesche, M., Ansmann, A., and Wiedensohler, A. (2011). Characterization of the planetary boundary layer during SAMUM-2 by means of lidar measurements. *submitted to Tellus*, **63B**. 79

Gysel, M., Weingartner, E., and Baltensperger, U. (2002). Hygroscopicity of Aerosol Particles at Low Temperatures. 2. Theoretical and Experimental Hygroscopic Properties of Laboratory Generated Aerosols. *Environ. Sci. Technol.*, **36**(1), 63–68. 15, 16, 29

Gysel, M., McFiggans, G. B., and Coe, H. (2009). Inversion of tandem differential mobility analyser (TDMA) measurements. *J. Aerosol Sci.*, **40**(2), 134–151. 34, 35, 43

Haken, H. and Wolf, H. C. (1998). *Molekülphysik und Quantenchemie: Einführung in die experimentellen und theoretischen Grundlagen*. Springer, Berlin, Heidelberg. 50

Hale, G. M. and Querry, M. R. (1973). Optical Constants of Water in the 200-nm to 200-μm Wavelength Region. *Appl. Opt.*, **12**(3), 555–563. 77

Hänel, G. (1976). The properties of atmospheric aerosol particles as functions of the relative humidity at thermodynamic equilibrium with the surrounding moist air. *Adv. Geophys.*, **19**, 74–189. VI, VII, 3, 82, 84, 87, 88, 89

Hänel, G. (1984). Parameterization of the influence of relative humidity on optical aerosol properties. In H. Gerber and A. Deepak, editors, *Aerosols and their climatic effects*, pages 117–122. A. Deepak, Hampton, VA. 83

Haywood, J. and Boucher, O. (2000). Estimates of the direct and indirect radiative forcing due to tropospheric aerosols: A review. *Rev. Geophys.*, **38**(4), 513–543. 2

Haywood, J., Francis, P., Osborne, S., Glew, M., Loeb, N., Highwood, E., Tanré, D., Myhre, G., Formenti, P., and Hirst, E. (2003). Radiative properties and direct radiative effect of Saharan dust measured by the C-130 aircraft during SHADE: 1. Solar spectrum. *J. Geophys. Res.*, **108**(D18), 8577. 90, 91

Haywood, J. M., Francis, P. N., Glew, M. D., and Taylor, J. P. (2001). Optical properties and direct radiative effect of Saharan dust: A case study of two Saharan dust outbreaks using aircraft data. *J. Geophys. Res.*, **106**(D16), 18417–18430. 29, 90

Hegg, D. A., Covert, D. S., Rood, M. J., and Hobbs, P. V. (1996). Measurements of aerosol optical properties in marine air. *J. Geophys. Res.*, **101**(D8), 12893–12903. 3, 82, 84

Heintzenberg, J., Charlson, R. J., Clarke, A. D., Liousse, C., Ramaswamy, V., Shine, K. P., Wendisch, M., and Helas, G. (1997). Measurements and Modelling of Aerosol Single-Scattering Albedo: Progress, Problems and Prospects. *Beitr. Phys. Atmos.*, **70**(4), 249–263. 1, 10

Heintzenberg, J., Wiedensohler, A., Tuch, T. M., Covert, D. S., Sheridan, P., Ogren, J. A., Gras, J., Nessler, R., Kleefeld, C., Kalivitis, N., Aaltonen, V., Wilhelm, R., and Havlicek, M. (2006). Intercomparisons and Aerosol Calibrations of 12 Commercial Integrating Nephelometers of Three Manufacturers. *J. Atmos. Oceanic Technol.*, **23**(7), 902–914. 45, 46

Hermann, M. and Wiedensohler, A. (2001). Counting efficiency of condensation particle counters at low-pressures with illustrative data from the upper troposphere. *J. Aerosol Sci.*, **32**(8), 975–991. 26

Hess, M., Koepke, P., and Schult, I. (1998). Optical Properties of Aerosols and Clouds: The Software Package OPAC. *Bull. Am. Meteorol. Soc.*, **79**(5), 831–844. 58, 66, 67, 68

Hoppel, W. A., Fitzgerald, J. W., Frick, G. M., Larson, R. E., and Mack, E. J. (1990). Aerosol Size Distributions and Optical Properties Found in the Marine Boundary Layer Over the Atlantic Ocean. *J. Geophys. Res.*, **95**(D4), 3659–3686. 52

Howell, S. G., Clarke, A. D., Shinozuka, Y., Kapustin, V. N., McNaughton, C. S., Huebert, B. J., Doherty, S., and Anderson, T. (2006). Influence of relative humidity upon pollution and dust during ACE-Asia: Size distributions and implications for optical properties. *J. Geophys. Res.*, **111**, D06205. 3, 83

IPCC (2007). *Climate Change 2007: The Physical Science Basis. Contributions of Working Group I to the Fourth Assessment Report of the Intergovernmental Panel on Climate Change*. Cambridge University Press, Cambridge, United Kingdom and New York, USA. 2

Junge, C. and Jaenicke, R. (1971). New results in background aerosols studies from the Atlantic expedition of the R.V. Meteor, Spring 1969. *J. Aerosol Sci.*, **2**(3), 305–314. 54

Kaaden, N., Massling, A., Schladitz, A., Müller, T., Kandler, K., Schütz, L., Weinzierl, B., Petzold, A., Tesche, M., Leinert, S., Deutscher, C., Ebert, M., Weinbruch, S., and Wiedensohler, A. (2009). State of mixing, shape factor, number size distribution, and

hygroscopic growth of the Saharan anthropogenic and mineral dust aerosol at Tinfou, Morocco. *Tellus*, **61B**(1), 51–63. 29, 38, 53, 57

Kahnert, M., Nousiainen, T., and Räisänen, P. (2007). Mie simulations as an error source in mineral aerosol radiative forcing calculations. *Quart. J. Roy. Meteor. Soc.*, **133**(623 B), 299–307. 68

Kalashnikova, O. V. and Sokolik, I. N. (2002). Importance of shapes and compositions of wind-blown dust particles for remote sensing at solar wavelengths. *Geophys. Res. Lett.*, **29**(10), 38–1 – 38–4. 68, 69, 72

Kalashnikova, O. V., Kahn, R., Sokolik, I. N., and Li, W. H. (2005). Ability of multiangle remote sensing observations to identify and distinguish mineral dust types: Optical models and retrievals of optically thick plumes. *J. Geophys. Res.*, **110**, D18S14. 68, 69, 72, 90

Kandler, K. (2010). personal communication. 49

Kandler, K., Benker, N., Bundke, U., Cuevas, E., Ebert, M., Knippertz, P., Rodríguez, S., Schütz, L., and Weinbruch, S. (2007). Chemical composition and complex refractive index of Saharan Mineral Dust at Izaña, Tenerife (Spain) derived by electron microscopy. *Atmos. Environ.*, **41**(37), 8058–8074. 51

Kandler, K., Schütz, L., Deutscher, C., Ebert, M., Hofmann, H., Jäckel, S., Jaenicke, R., Knippertz, P., Lieke, K., Massling, A., Petzold, A., Schladitz, A., Weinzierl, B., Wiedensohler, A., Zorn, S., and Weinbruch, S. (2009). Size distribution, mass concentration, chemical and mineralogical composition and derived optical parameters of the boundary layer aerosol at Tinfou, Morocco, during SAMUM 2006. *Tellus*, **61B**(1), 32–50. 29, 49, 50

Kandler, K., Lieke, K., Benker, N., Emmel, C., Küpper, M., Müller-Ebert, D., Ebert, M., Scheuvens, D., Schladitz, A., Schütz, L., and Weinbruch, S. (2011). Electron microscopy of particles collected at Praia, Cape Verde, during the Saharan Mineral Dust Experiment: Microphysical properties and mineralogy. *submitted to Tellus*, **63B**. 56, 57, 68

Kasten, F. (1969). Visibility forecast in the phase of pre-condensation. *Tellus*, **21**(5), 631–635. 82

Kelly, W. P. and McMurry, P. H. (1992). Measurement of Particle Density by Inertial Classification of Differential Mobility Analyzer-Generated Monodisperse Aerosols. *Aerosol Sci. Technol.*, **17**(3), 199–212. 29

Kenny, L. C. and Gussman, R. A. (1997). Characterization and modelling of a family of cyclone aerosol preseparators. *J. Aerosol Sci.*, **28**(4), 677–688. 47

Kenny, L. C. and Gussman, R. A. (2000). A direct approach to the design of cyclones for aerosol-monitoring applications. *J. Aerosol Sci.*, **31**(12), 1407–1420. 48

Kinne, S., Lohmann, U., Feichter, J., Schulz, M., Timmreck, C., Ghan, S., Easter, R., Chin, M., Ginoux, P., Takemura, T., Tegen, I., Koch, D., Herzog, M., Penner, J., Pitari, G., Holben, B., Eck, T., Smirnov, A., Dubovik, O., Slutsker, I., Tanré, D., Torres, O., Mishchenko, M. I., Geogdzhayev, I., Chu, D., and Kaufman, Y. (2003). Monthly averages of aerosol properties: A global comparison among models, satellite data, and AERONET ground data. *J. Geophys. Res.*, **108**(D20), 4634. 3

Kirchstetter, T. W., Novakov, T., and Hobbs, P. V. (2004). Evidence that the spectral dependence of light absorption by aerosols is affected by organic carbon. *J. Geophys. Res.*, **109**, D21208. 10, 65

Knippertz, P., Ansmann, A., Althausen, D., Müller, D., Tesche, M., Bierwirth, E., Dinter, T., Müller, T., von Hoyningen-Huene, W., Schepanski, K., Wendisch, M., Heinold, B., Kandler, K., Petzold, A., Schütz, L., and Tegen, I. (2009). Dust mobilization and transport in the northern Sahara during SAMUM 2006 - a meteorological overview. *Tellus*, **61B**(1), 12–31. 68

Knippertz, P., Tesche, M., Heinold, B., Kandler, K., Toledano, C., and Esselborn, M. (2011). Dust Mobilization and Aerosol Transport from West Africa to Cape Verde: A Meteorological Overview of SAMUM-2. *submitted to Tellus*, **63B**. 68, 81

Knutson, E. O. and Whitby, K. T. (1975). Aerosol Classification by Electric Mobility: Apparatus, Theory, and Applications. *J. Aerosol Sci.*, **6**(6), 443–451. 25, 26

Koepke, P. and Hess, M. (1988). Scattering functions of tropospheric aerosols: the effects of nonspherical particles. *Appl. Opt.*, **27**(12), 2422–2430. 68, 69

Köhler, H. (1936). The nucleus in and the growth of hygroscopic droplets. *Trans. Faraday Soc.*, **32**, 1152–1161. 3, 11

Kotchenruther, R. A., Hobbs, P. V., and Hegg, D. A. (1999). Humidification factors for atmospheric aerosols off the mid-Atlantic coast of the United States. *J. Geophys. Res.*, **104**(D2), 2239–2251. 84

Lack, D. A., Quinn, P., Massoli, P., Bates, T., Coffman, D., Covert, D. S., Sierau, B., Tucker, S., Baynard, T., Lovejoy, E., Murphy, D. M., and Ravishankara, A. R. (2009). Relative humidity dependence of light absorption by mineral dust after long-range atmospheric transport from the Sahara. *Geophys. Res. Lett.*, **36**, L24805. 3

Lee, S. D., Schneider, T., Grant, L. D., and Verkerk, J. P. (1986). Aerosols: Research, risk assessment and control strategies. In *II. U.S.-Dutch International Symposium on Aerosols*, volume 19, Williamsburg, Va. Lewis Publishers, Inc. 74

Leinert, S. and Wiedensohler, A. (2008). A DMA and APS based technique for measuring aerodynamic hygroscopic growth factors of micrometer-size aerosol particles. *J. Aerosol Sci.*, **39**, 393–402. 40

Li-Jones, X., Maring, H. B., and Prospero, J. M. (1998). Effect of relative humidity on light scattering by mineral dust aerosol as measured in the marine boundary layer over the tropical Atlantic Ocean. *J. Geophys. Res.*, **103**(D23), 31113–31121. 3

Liao, H. and Seinfeld, J. H. (1998). Radiative forcing by mineral dust aerosols: sensitivity to key variables. *J. Geophys. Res.*, **103**(D24), 31637–31646. 1

Lieke, K., Kandler, K., Scheuvens, D., Emmel, C., von Glahn, C., Petzold, A., Weinzierl, B., Veira, A., Ebert, M., Weinbruch, S., and Schütz, L. (2011). Particle chemical properties in the vertical column based on aircraft observations in the vicinity of Cape Verde. *submitted to Tellus*, **63B**. 68

Liljequist, G. H. and Cehak, K. (2006). *Allgemeine Meteorologie*. Springer, Berlin Heidelberg, 3. edition. 11

Linke, C., Möhler, O., Veres, A., Mohácsi, A., Bozóki, Z., Szabó, G., and Schnaiter, M. (2006). Optical properties and mineralogical composition of different Saharan mineral dust samples: a laboratory study. *Atmos. Chem. Phys.*, **6**(11), 3315–3323. 10, 90

Liu, B. Y. H., Pui, D. Y. H., Whitby, K. T., Kittelson, D. B., Kousaka, Y., and McKenzie, R. L. (1978). The aerosol mobility chromatograph: a new detector for sulfuric acid aerosols. *Atmos. Environ.*, **12**(1-3), 99–104. 34

Liu, B. Y. H., Pui, D. Y. H., Wang, X. Q., and Lewis, C. W. (1983). Sampling of carbon fiber aerosols. *Aerosol Sci. Technol.*, **2**(4), 499–511. 74

Massling, A., Leinert, S., Wiedensohler, A., and Covert, D. S. (2007). Hygroscopic growth of sub-micrometer and one-micrometer aerosol particles measured during ACE-Asia. *Atmos. Chem. Phys.*, **7**, 3249–3259. 34, 38, 57

Massling, A., Stock, M., Wehner, B., Wu, Z. J., Hu, M., Brüggemann, E., Gnauk, T., Herrmann, H., and Wiedensohler, A. (2009). Size segregated water uptake of the urban submicrometer aerosol in Beijing. *Atmos. Environ.*, **43**(8), 1578–1589. 43

Massling, A., Niedermeier, N., Hennig, T., Fors, E., Swietlicki, E., Ehn, M., Hämeri, K., Villani, P., Laj, P., Good, N., McFiggans, G. B., and Wiedensohler, A. (2010). Results and recommendations from an intercomparison of six Hygroscopicity-TDMA systems. *Atmos. Meas. Tech. Discuss.*, **3**, 637–674. 34

Maxwell-Garnett, J. C. (1904). Colours in metal glasses and metal films. *Philos. Trans. Roy. Soc. London*, **203**, 385–420. 59

Meier, J., Wehner, B., Massling, A., Birmili, W., Nowak, A., Gnauk, T., Brüggemann, E., Herrmann, H., Min, H., and Wiedensohler, A. (2009). Hygroscopic growth of urban aerosol particles in Beijing (China) during wintertime: a comparison of three experimental methods. *Atmos. Chem. Phys.*, **9**, 6865–6880. 39, 41

Mertes, S., Schröder, F., and Wiedensohler, A. (1995). The Particle Detection Efficiency Curve of the TSI-3010 CPC as a Function of the Temperature Difference between Saturator and Condenser. *Aerosol Sci. Technol.*, **23**(2), 257–261. 26

Mertes, S., Dippel, B., and Schwarzenböck, A. (2004). Quantification of graphitic carbon in atmospheric aerosol particles by Raman spectroscopy and first application for the determination of mass absorption effciencies. *J. Aerosol Sci.*, **35**(3), 347–361. 50

Mészáros, A. and Vissy, K. (1974). Concentration, size distribution and chemical nature of atmospheric aerosol particles in remote oceanic areas. *J. Aerosol Sci.*, **5**(1), 101–109. 53

Meusinger, C. (2009). *Calibration of a spectral particle absorption photometer for determination of atmospheric mineral dust concentrations and measurements on Cape Verde Islands.* Master thesis, University of Leipzig, Germany. 49

Mie, G. (1908). Beiträge zur Optik trüber Medien, speziell kolloidaler Metallösungen. *Ann. d. Phys.*, **330**(3), 377–445. 8

Mikhailov, E., Vlasenko, S., Niessner, R., and Pöschl, U. (2004). Interaction of aerosol particles composed of protein and salts with water vapor: hygroscopic growth and microstructural rearrangement. *Atmos. Chem. Phys.*, **4**(2), 323–350. III, 16

Mishchenko, M. I., Lacis, A. A., Carlson, B. E., and Travis, L. D. (1995). Nonsphericity of dust-like tropospheric aerosols: Implications for aerosol remote sensing and climate modeling. *Geophys. Res. Lett.*, **22**(9), 1077–1080. 68, 72

Mishchenko, M. I., Travis, L. D., and Macke, A. (1996). Scattering of light by polydisperse, randomly oriented, finite circular cylinders. *Appl. Opt.*, **35**(24), 4927–4940. 72

Mishchenko, M. I., Travis, L. D., Kahn, R. A., and West, R. A. (1997). Modeling phase functions for dustlike tropospheric aerosols using a shape mixture of randomly oriented polydisperse spheroids. *J. Geophys. Res.*, **102**(D14), 16831–16847. 68

Mishchenko, M. I., Wiscombe, W. J., Hovenir, J. W., and Travis, L. D. (2000). Overview of Scattering by Nonspherical Particles. In M. I. Mishchenko, J. W. Hovenir, and L. D. Travis, editors, *Light Scattering by Nonspherical Particles*, pages 30–59. Academic Press, San Diego. 8

Müller, T., Nowak, A., Wiedensohler, A., Sheridan, P., Laborde, M., Covert, D. S., Marinoni, A., Imre, K., Henzing, B., Roger, J. C., Martins dos Santos, S., Wilhelm, R., Wang, Y., and de Leeuw, G. (2009a). Angular Illumination and Truncation of Three Different Integrating Nephelometers: Implications for Empirical, Size-Based Corrections. *Aerosol Sci. Technol.*, **43**(6), 581–586. 46, 59

Müller, T., Schladitz, A., Massling, A., Kaaden, N., Kandler, K., and Wiedensohler, A. (2009b). Spectral absorption coefficients and imaginary parts of refractive indices of Saharan dust during SAMUM-1. *Tellus*, **61B**(1), 79–95. 10, 48, 49, 66, 68, 72

Müller, T., Henzing, J. S., De Leeuw, G., Wiedensohler, A., Alastuey, A., Angelov, H., Bizjak, M., Collaud Coen, M., Engström, J. E., Gruening, C., Hillamo, R., Hoffer, A., Imre, K., Ivanow, P., Jennings, G., Sun, J. Y., Kalivitis, N., Karlsson, H., Komppula, M., Laj, P., Li, S.-M., Lunder, C., Marinoni, A., Martins dos Santos, S., Moerman, M., Nowak, A., Ogren, J. A., Petzold, A., Pichon, J. M., Rodríguez, S., Sharma, S., Sheridan, P., Teinilä, K., Tuch, T., Viana, M., Virkkula, A., Weingartner, E., Wilhelm, R., and Wang, Y. Q. (2010). Characterization and intercomparison of aerosol absorption photometers: result of two intercomparison workshops. *Atmos. Meas. Tech. Discuss.*, **3**, 1511–1582. 47, 48

Nakajima, T., Tanaka, M., Yamano, M., Shiobara, M., Arao, K., and Nakanishi, Y. (1989). Aerosol Optical Characteristics in the Yellow Sand Events Observed in May, 1982 at Nagasaki-Part 2 Models. *J. Meteor. Soc. Japan*, **67**(2), 279–291. 68

Nemesure, S., Wagener, R., and Schwartz, S. E. (1995). Direct shortwave forcing of climate by anthropogenic sulfate aerosol: Sensitivity to particle size, composition, and relative humidity. *J. Geophys. Res.*, **100**(26), 26105–26116. 3

Nessler, R., Weingartner, E., and Baltensperger, U. (2005). Adaptation of Dry Nephelometer Measurements to Ambient Conditions at the Jungfraujoch. *Environ. Sci. Technol.*, **39**(7), 2219–2228. 82

Niedermeier, D., Wex, H., Voigtländer, J., Stratmann, F., Brüggemann, E., Kiselev, A., Henk, H., and Heintzenberg, J. (2008). LACIS-measurements and parameterization of sea-salt particle hygroscopic growth and activation. *Atmos. Chem. Phys.*, **8**, 579–590. 56

Nowak, A. (2006). *Das feuchte Partikelgrößenspektrometer: Eine neue Messmethode zur Bestimmung von Partikelgrößenverteilungen (< 1 µm) und größenaufgelösten hygroskopischen Wachstumsfaktoren bei definierten Luftfeuchten*. PhD-thesis, University of Leipzig, Germany. 26, 30, 38

O'Dowd, C. D. and Smith, M. H. (1993). Physicochemical Properties of Aerosols Over the Northeast Atlantic: Evidence for Wind-Speed-Related Submicron Sea-Salt Aerosol Production. *J. Geophys. Res.*, **98**(D1), 1137–1149. 54

O'Dowd, C. D., Smith, M. H., Consterdine, I. E., and Lowe, J. A. (1997). Marine aerosol, sea-salt, and the marine sulphur cycle: A short review. *Atmos. Environ.*, **31**(1), 73–80. 54

Orr, Jr, C., Hurd, F. K., and Corbett, W. J. (1958). Aerosol size and relative humidity. *J. Colloid Sci.*, **13**, 472–482. 15

Otto, S., Bierwirth, E., Weinzierl, B., Kandler, K., Esselborn, M., Tesche, M., Schladitz, A., Wendisch, M., and Trautmann, T. (2009). Solar radiative effects of a Saharan dust plume observed during SAMUM assuming spheroidal model particles. *Tellus*, **61B**(1), 270–296. 72, 91

Petters, M. D. and Kreidenweis, S. M. (2007). A single parameter representation of hygroscopic growth and cloud condensation nucleus activity. *Atmos. Chem. Phys.*, **7**(8), 1961–1971. 11, 15, 56

Pollack, J. B. and Cuzzi, J. N. (1980). Scattering by Nonspherical Particles of Size Comparable to a Wavelength: A New Semi-Empirical Theory and Its Application to Tropospheric Aerosols. *J. Atmos. Sci.*, **37**, 868–881. 68

Prospero, J. M., Ginoux, P., Torres, O., Nicholson, S. E., and Gill, T. E. (2002). Environmental characterization of global sources of atmospheric soil dust identified with the Nimbus 7 Total Ozone Mapping Spectrometer (TOMS) absorbing aerosol product. *Rev. Geophys.*, **40**(1), 1002. 2

Pruppacher, H. R. and Klett, J. D. (1997). *Microphysics of clouds and precipitation*. D. Reidel Publishing Company, Dordrecht, Holland. 11, 12

Purcell, E. M. and Pennypacker, C. R. (1973). Scattering and absorption of light by nonspherical dielectric grains. *Astrophys. J.*, **186**(2), 705–714. 8

Quinn, P. K., Anderson, T. L., Bates, T. S., Dlugi, R., Heintzenberg, J., von Hoyningen-Huene, W., Kulmala, M., Russell, P. B., and Swietlicki, E. (1996). Closure in tropospheric aerosol-climate research: A review and future needs for addressing aerosol direct shortwave radiative forcing. *Beitr. Phys. Atmos.*, **69**(4), 547–577. 3

Quinn, P. K., Coffman, D. J., Kapustin, V. N., Bates, T. S., and Covert, D. S. (1998). Aerosol optical properties in the marine boundary layer during the First Aerosol Characterization Experiment (ACE 1) and the underlying chemical and physical aerosol properties. *J. Geophys. Res.*, **103**(D13), 16547–16563. 10

Quinn, P. K., Bates, T. S., Baynard, T., Clarke, A. D., Onasch, T. B., Wang, W., Rood, M. J., Andrews, E., Allan, J., Carrico, C. M., Coffman, D., and Worsnop, D. R. (2005). Impact of particulate organic matter on the relative humidity dependence of light scattering: A simplified parameterization. *Geophys. Res. Lett.*, **32**, L22809. 82, 83

Ramaswamy, V., Boucher, O., Haigh, J., Hauglustaine, D., Haywood, J., Myhre, G., Nakajima, T., Shi, G. Y., and Solomon, S. (2001). Radiative forcing of climate change. In J. Houghton, Y. Ding, D. Griggs, M. Noguer, P. van der Linden, and D. Xiasu, editors, *Climate Change 2001: The scientific Basis. Contribution of Working Group I to the Third Assessment Report of the Intergovernmental Panel on Climate Change*, pages 349–416. Cambridge University Press, Cambridge, United Kingdom and New York, USA. 2

Randall, D., Wood, R., Bony, S., Colman, R., Fichefet, T., Fyfe, J., Kattsov, V., Pitman, A., Shukla, J., Srinivasan, J., Stouffer, R., Sumi, A., and Taylor, K. (2007). Climate models and their evaluation. In S. Solomon, D. Qin, M. Manning, Z. Chen, M. Marquis, K. Averyt, M. Tignor, and H. Miller, editors, *Climate Change 2007: The Physical Basis. Contribution of Working group I to the Fourth Assessment Report of the Intergovernmental Panel on Climate Change*. Cambridge University Press, Cambridge, United Kingdom and New York, USA. 3

Rogers, R. R. and Yau, M. K. (1989). *A short course in cloud physics*, volume 113 of *Natural Philosophy*. Pergamon Press, Oxford, 3rd edition. 11, 12

Rood, M. J., Shaw, M. A., Larson, T. V., and Covert, D. S. (1989). Ubiquitous nature of ambient metastable aerosol. *Nature*, **337**, 537–539. 16

Rose, D., Gunthe, S. S., Mikhailov, E., Frank, G. P., Dusek, U., Andreae, M. O., and Pöschl, U. (2008). Calibration and measurement uncertainties of a continuous-flow cloud condensation nuclei counter (DMT-CCNC): CCN activation of ammonium sulfate and sodium chloride aerosol particles in theory and experiment. *Atmos. Chem. Phys.*, **8**(5), 1153–1179. 11

Rosen, H., Hansen, A. D. A., Gundel, L., and Novakov, T. (1978). Identification of the optically absorbing component in urban aerosols. *Appl. Opt.*, **17**(24), 3859–3861. 50

Schladitz, A., Müller, T., Kaaden, N., Massling, A., Kandler, K., Ebert, M., Weinbruch, S., Deutscher, C., and Wiedensohler, A. (2009). In situ measurements of optical properties at Tinfou (Morocco) during the Saharan Mineral Dust Experiment SAMUM 2006. *Tellus*, **61B**(1), 64–78. 29, 90

Schnaiter, M., Horvath, H., Möhler, O., Naumann, K. H., Saathoff, H., and Schöck, O. W. (2003). UV-VIS-NIR spectral optical properties of soot and soot-containing aerosols. *J. Aerosol Sci.*, **34**(10), 1421–1444. 10

Seinfeld, J. H. and Pandis, N. S. (2006). *Atmospheric Chemistry and Physics: From Air Pollution to Climate Change*. John Wiley & Sons, Inc., Hoboken, NJ, 2nd edition edition. 1

Shettle, E. P. and Fenn, R. W. (1979). Models for the aerosols of the lower atmosphere and the effects of humidity variations on their optical properties. *AFGL-TR-79-0214*, **Environmetal Research Papers No. 675**, 94 pp. VI, VII, 3, 84, 87, 88, 89, 91

Sokolik, I. N. and Toon, O. B. (1999). Incorporation of mineralogical composition into models of the radiative properties of mineral aerosol from UV to IR wavelengths. *J. Geophys. Res.*, **104**(D8), 9423–9444. 4, 91

Stock, M. (2006). *Hygroskopische Eigenschaften und Mischungszustand des sommerlichen ostmediterranen Aerosols in Abhängigkeit der Luftmasse auf Kreta.* Diploma thesis, University of Leipzig, Germany. 38

Stratmann, F. and Wiedensohler, A. (1996). A new data inversion algorithm for DMPS-measurements. In *European Aerosol Conference*, volume 27, Supplement 1, pages 339–340, Delft. J. Aerosol Sci. 29, 41

Swietlicki, E., Hansson, H. C., Hämeri, K., Svenningsson, B., Massling, A., McFiggans, G., McMurry, P. H., Petäjä, T., Tunved, P., Gysel, M., Topping, D., Weingartner, E., Baltensperger, U., Rissler, J., Wiedensohler, A., and Kulmala, M. (2008). Hygroscopic properties of submicrometer atmospheric aerosol particles measured with H-TDMA instruments in various environments-a review. *Tellus*, **60B**(3), 432–469. 35

Tang, I. N. (1996). Chemical and size effects of hygroscopic aerosols on light scattering coefficients. *J. Geophys. Res.*, **101**(D14), 19245–19250. III, IX, 13, 14, 15, 32

Tang, I. N. and Munkelwitz, H. R. (1994). Water activities, densities, and refractive indices of aqueous sulfates and sodium nitrate droplets of atmospheric importance. *J. Geophys. Res.*, **99**(D9), 18801–19808. III, 11, 13, 14, 32

Tegen, I. and Fung, I. (1995). Contribution to the atmospheric mineral aerosol load from land surface modification. *J. Geophys. Res.*, **100**(D9), 18707–18726. 2

Tegen, I., Lacis, A. A., and Fung, I. (1996). The influence on climate forcing of mineral aerosols from disturbed soils. *Nature*, **380**(6573), 419–422. 1, 2, 4

Tegen, I., Werner, M., Harrison, S. P., and Kohfeld, K. E. (2004). Relative importance of climate and land use in determining present and future global soil dust emission. *Geophys. Res. Lett.*, **31**(L05105). 2

Tesche, M., Ansmann, A., Müller, D., Althausen, D., Engelmann, R., Freudenthaler, V., and Groß, S. (2009). Vertically resolved separation of dust and smoke over Cape Verde using multiwavelength Raman and polarization lidars during Saharan Mineral Dust Experiment 2008. *J. Geophys. Res.*, **114**(D13), D13202. 79

Tuch, T. M., Haudek, A., Müller, T., Nowak, A., Wex, H., and Wiedensohler, A. (2009). Design and performance of an automatic regenerating adsorption aerosol dryer for continuous operation at monitoring sites. *Atmos. Meas. Tech.*, **2**, 417–422. 22, 74

Tuinstra, F. and Koenig, J. L. (1970). Raman Spectrum of Graphite. *J. Chem. Phys.*, **53**(3), 1126–1130. 50

Twomey, S. (1974). Pollution and the planetary albedo. *Atmos. Environ.*, **8**(12), 1251–1256. 1

Twomey, S. (1977). The influence of pollution on the shortwave albedo of clouds. *J. Atmos. Sci.*, **34**(7), 1149–1152. 1

van de Hulst, H. C. (1957). *Light scattering by small particles*. John Wiley & Sons, Inc., London. 7

Washington, R., Todd, M., Middleton, N. J., and Goudie, A. S. (2003). Dust-storm source areas determined by the total ozone monitoring spectrometer and surface observations. *Ann. Assoc. Am. Geogr.*, **93**(2), 297–313. 3

Waterman, P. C. (1971). Symmetry, unitarity, and geometry in electromagnetic scattering. *Phys. Rev. D*, **3**(4), 825. 8

West, R. A., Doose, L. R., Eibl, A. M., Tomasko, M. G., and Mishchenko, M. I. (1997). Laboratory measurements of mineral dust scattering phase function and linear polarization. *J. Geophys. Res.*, **102**(D14), 16871–16881. 68

Wex, H., Neusüß, C., Wendisch, M., Stratmann, F., Koziar, C., Keil, A., Wiedensohler, A., and Ebert, M. (2002). Particle scattering, backscattering, and absorption coefficients: An in situ closure and sensitivity study. *J. Geophys. Res.*, **107**(D21), 8122. V, 59

Wex, H., Stratmann, F., Hennig, T., Hartmann, S., Niedermeier, D., Nilsson, E., Ocskay, R., Rose, D., Salma, I., and Ziese, M. (2008). Connecting hygroscopic growth at high humidities to cloud activation for different particle types. *Environ. Res. Lett.*, **3**, 035004. 15

Wiedensohler, A. (1988). An approximation of the bipolar charge distribution for particles in the submicron size range. *J. Aerosol Sci.*, **19**(3), 387–389. 25

Wiedensohler, A., Orsini, D., Covert, D. S., Coffmann, D., Cantrell, W., Havlicek, M., Brechtel, F. J., Russell, L. M., Weber, R. J., Gras, J., Hudson, J. G., and Litchy, M. (1997). Intercomparison Study of the Size-Dependent Counting Efficiency of 26 Condensation Particle Counters. *Aerosol Sci. Technol.*, **27**(2), 224–242. 26

Wiedensohler, A., Birmili, W., Nowak, A., Sonntag, A., Weinhold, K., Merkel, M., Wehner, B., Tuch, T., Pfeifer, S., Fiebig, M., Fjäraa, A. M., Asmi, E., Sellegri, K., Depuy, R., Venzac, H., Villani, P., Laj, P., Aalto, P., Ogren, J. A., Swietlicki, E., Roldin, P., Williams, P., Quincey, P., Hüglin, C., Fierz-Schmidhauser, R., Gysel, M., Weingartner, E., Riccobono, F., Santos, S., Grüning, C., Faloon, K., Beddows, D., Harrison, R. M., Monahan, C., Jennings, S. G., O'Dowd, C. D., Marinoni, A., Horn, H. G., Keck, L., Jiang, J., Scheckman, J., McMurry, P. H., Deng, Z., Zhao, C. S., Moerman, M., Henzing, B., and de Leeuw, G. (2010). Particle mobility size spectrometers: harmonization of technical standards and data structure to facilitate high quality long-term observations of atmospheric particle number size distributions. *Atmos. Meas. Tech. Discuss.*, **3**(6), 5521–5587. 26

Wiegner, M., Quenzel, H., Rabus, D., Volker, W., Volger, P., Ackermann, J., Kahler, C., Fergg, F., and Wildgruber, G. (1995). Mobile three-wavelength backscatter lidar of the Meteorological Institute of the University of Munich. In J. Becherer, Richard, editor, *Lidar and Atmospheric Sensing*, volume 2505, pages 2–10, Munich, Germany. Proc. SPIE Int. Soc. Opt. Eng. 79

Wiegner, M., Gasteiger, J., Kandler, K., Weinzierl, B., Rasp, K., Esselborn, M., Freudenthaler, V., Heese, B., Toledano, C., Tesche, M., and Althausen, D. (2009). Numerical simulations of optical properties of saharan dust aerosols with emphasis on lidar applications. *Tellus*, **61B**(1), 180–194. 69, 72

Willeke, K. and Baron, P. A. (1993). *Aerosol Measurement - Principles, Techniques, and Applications*. Van Nostrand Reinhold, New York. 24

Winklmayr, W., Wang, H. C., and John, W. (1990). Adaptation of the Twomey Algorithm to the Inversion of Cascade Impactor Data. *Aerosol Sci. Technol.*, **13**(3), 322–331. 48

Yee, K. (1966). Numerical solution of inital boundary value problems involving maxwell's equations in isotropic media. *IEEE Trans. Antennas Propag.*, **14**(3), 302–307. 8

Yoon, S. C. and Kim, J. (2006). Influences of relative humidity on aerosol optical properties and aerosol radiative forcing during ACE-Asia. *Atmos. Environ.*, **40**(23), 4328–4338. 3

Acknowledgements

I want to thank all persons, who contribute to the success of the present work.

- Prof. Dr. Alfred Wiedensohler, my supervisor, for his support to write this PhD-thesis at IfT. I want to thank him for all his help in the past years and also for his continuous motivation to do better.
- Dr. Thomas Müller, my tutor, who had always time and patience for several questions. Furthermore, I want to thank him for his support in the correct formulation of scientific results.
- Prof. Dr. David S. Covert, for reading the PhD-thesis and his critical comments.
- The SAMUM-team, especially Dr. Andreas Massling, Dr. Andreas Nowak, and Dr. Konrad Kandler, for their great support at Cape Verde and the time thereafter.
- Dr. Martin Gysel, for answering me a couple of questions concerning the data evaluation of the HTDMA.
- The electronic and mechanical workshop, especially Hartmut Haudek, Andrea Haudek, Anja Schmidt, and Peter Glomb for all their quick help, especially for the field experiment at Cape Verde.
- Nicole Niedermeier, Dennis Niedermeier, and Dr. Heike Wex for stimulating discussions about hygroscopicity and Stephan Nordmann for our discussions during lunch.
- My colleagues in the office, for the great working atmosphere.
- My family, my girlfriend Anne-Kathrin, and my friends for the great time and continuous support.
- All other persons, I forgot to mention.